Transmission Line Modelling for Inverter-Fed Induction Machines

Transmission Line Modellierung für umrichtergespeiste Asynchronmaschinen
Zur Erlangung des akademischen Grades Doktor-Ingenieur (Dr.-Ing.)
genehmigte Dissertation von Hai Van Le Jorks aus Gera
Februar 2015 — Darmstadt — D 17

TECHNISCHE
UNIVERSITÄT
DARMSTADT

Fachbereich Elektrotechnik und Informationstechnik
Institut für Theorie Elektromagnetischer Felder (TEMF)

Transmission Line Modelling for Inverter-Fed Induction Machines
Transmission Line Modellierung für umrichtergespeiste Asynchronmaschinen

Genehmigte Dissertation von Hai Van Le Jorks aus Gera

1. Gutachten: Prof. Dr.-Ing. T. Weiland
2. Gutachten: Prof. Dr.-Ing. K. Hameyer

Tag der Einreichung: 22.04.2014
Tag der Prüfung: 09.09.2014

Darmstadt — D 17

Transmission Line Modelling for Inverter-Fed Induction Machines

Vom Fachbereich Elektrotechnik und Informationstechnik
der Technischen Universität Darmstadt
zur Erlangung des akademischen Grades eines
Doktor-Ingenieurs (Dr.-Ing.)
genehmigte Dissertation

von **Dipl.-Ing. Hai Van Le Jorks**
Geboren am 25.03.1981 in Gera

Referent:	Prof. Dr.-Ing. Thomas Weiland
Korreferent:	Prof. Dr.-Ing. Kay Hameyer
Tag der Einreichung:	22.04.2014
Tag der mündlichen Prüfung:	09.09.2014

D17
Darmstadt 2015

Dedicated to my family

Abstract

This thesis is focused on high-frequency (HF) modelling of inverter-fed induction machines. The common mode (CM) input impedance of an existing 240 kW induction machine is computed in the frequency range of 10 Hz - 1 MHz and the results are compared to measurements. Transmission line (TL) theory is used to provide a consistent relation between field and circuit approaches.

In the analysis of electromagnetic fields, special attention is attributed to the modelling of eddy currents inside the core lamination. In order to investigate this effect thoroughly, two modelling approaches are compared. First, a 2D simulation approach, where iron core lamination effects are included by means of an equivalent material approximation. The second approach consists in fully three-dimensional (3D) analysis taking into account explicitly the eddy currents induced in the laminations.

In order to provide the 3D reference solution, a specialized simulation tool has been developed. The tool is built upon an existing in-house finite element (FE) code, which employs vector basis functions of both, low and high, order. Another key feature of the code is the parallel processing on a cluster, which allows for large-scale simulations of the 3D motor models. The FE code has been adapted to the extraction of the impedance matrix, which is associated with the conductors in the motor cross-section. Even though, the number of conductors may be numerous, the code allows for very efficient extraction of the desired parameters while avoiding unnecessary computational overhead.

All simulations are carried out in frequency domain. Still, a procedure to include the magnetic nonlinearity of the motor core material is discussed and implemented. The proposed method computes iteratively the inhomogeneous permeability distribution for a given low-frequency (LF) excitation. The material data are then used in the linear computations in the HF range.

The FE code is also successfully used for the computation of the 3D fields in the end-region of an induction machine. Once again, efficient large-scale simulations are realised, whereas here, mesh elements of different types have been combined.

The modelling approaches are presented, using the example of an inverter-fed induction machine. Nevertheless, they may be employed to obtain important HF parameters of other radial flux machine types as well.

Zusammenfassung

In der vorliegenden Arbeit werden Modellierungsmethoden für hochfrequente elektromagnetische Felder in umrichtergespeisten Asynchronmaschinen untersucht. Ziel ist die Berechnung der Gleichtakt-Eingangsimpedanz (Common Mode Impedanz) eines realen 240 kW Motors im Frequenzbereich 10 Hz - 1 MHz und der Vergleich mit Messergebnissen. Die Leitungstheorie (Transmission Line bzw. TL Theorie) dient dabei als Bindeglied zwischen der elektromagnetischen Feldanalyse und dem Klemmenverhalten der Maschine.

Einen Schwerpunkt der Feldanalyse bildet die Modellierung von Wirbelströmen in den dünnen Blechen der Eisenkerne. Dabei werden zwei Modellierungsansätze verglichen. Zum einen ein zweidimensionaler (2D) Ansatz, der Wirbelstromeffekte über einen äquivalenten Materialparameter berücksichtigt. Zum anderen werden dreidimensionale (3D) Simulationen durchgeführt, in denen sich die Wirbelstromfelder explizit ausbilden können.

Um die 3D Referenzlösung bereitstellen zu können, wurde ein spezielles Simulationstool entwickelt. Es basiert auf einem institutseigenen, parallelisierten Finite Elemente Code, in dem Basisfunktionen sowohl niedriger als auch hoher Ordnung verwendet werden können. Der Code wurde so modifiziert, das die gewünschte Impedanzmatrix des TL Motormodells sehr effizient extrahiert werden kann.

Alle Simulationen werden im Frequenzbereich ausgeführt. Auf dieser Basis wird eine Methode vorgestellt, mit der die Nichtlinearität der Eisenbleche berücksichtigt werden kann. In der Methode wird zunächst die Permeabilitätsverteilung im Motorblech bei niedriger Frequenz iterativ bestimmt. Anschließend wird diese Permeabilitätsverteilung verwendet, um die Impedanzmatrix bei hohen Frequenzen zu berechnen.

Der entwickelte Finite Elemente Code wird außerdem verwendet, um die 3D Felder in den Wicklungsköpfen der Maschine zu berechnen. Um die komplexe Geometrie zu diskretisieren, werden Tetraeder und Dreiecksprismen kombiniert.

Die Modellierungsverfahren sind am Beispiel der umrichtergespeisten Asynchronmaschine dargestellt. Sie können aber auch zur Untersuchung hochfrequenter Effekte in anderen Radialflussmaschinen verwendet werden.

Contents

1 Introduction

1.1 Motivation

Induction machines fed by a pulse-width modulation (PWM) frequency inverter are used in an increasing number of industry and traction applications, such as fans and pumps, hoists and elevators, rail vehicles, electrical and hybrid cars and many more. For the purpose of adjusting mechanical speed and torque of the drive, a power electronic converter supplies the three-phase induction machine with phase voltages of the desired amplitude and frequency.

However, the applied phase voltages are not pure sine waves, but rectangular voltage pulses. The pulse lengths are defined by the PWM strategy, in a way that the average over each pulse period yields the desired sinusoidal voltage value. The switching is performed by semiconductor devices, usually Insulated Gate Bipolar Transistors (IGBTs) or Power Metal Oxide Semiconductor Field-Effect Transistors (MOSFETs), which are turned on and off via their gate electrodes.

When induction machines designed for fixed-speed operation were used with PWM inverters, an increased number of bearing failures in the machines has been observed. The failures are related to excessive levels of bearing current and often occur only a few months after start-up [5]. The rapid switching in PWM inverters is introducing a high-frequency excitation to the drive system, which has been identified to cause large current spikes in the motor bearings [25].

PWM inverters are producing a common mode voltage as a result of their switching action. This voltage is an unwanted side-effect which appears as a common signal on all motor phases with respect to the ground.

The resulting common mode (CM) current gives rise to circulating bearing currents. In the presence of an unbroken lubrication film between bearing surfaces, the bearing voltage is proportional to the CM voltage [75]. The ratio of the bearing voltage and the CM voltage is defined as the Bearing Voltage Ratio (BVR). When the bearing voltage exceeds a threshold value, the thin layer of lubrication breaks down and discharge current pulses occur. The process is usually characterized by statistical properties [38]. Persistent high bearing current densities may significantly decrease the lifetime of the bearings [75].

It is possible to describe the high frequency behaviour of the motor in terms of a common mode impedance, defined as

$$Z_{\mathrm{CM}} := \frac{U_{\mathrm{CM}}}{I_{CM}}. \tag{1.1}$$

The frequency-dependent common mode impedance of a motor is crucial in the analysis of inverter-induced bearing currents. Owing to very short rise times of the PWM voltage pulses a broad frequency range has to be investigated. The classical motor models were created to represent low frequency behaviour. They neglect capacitive effects in the insulation as well as eddy-current effects in the conductors and laminations. Hence, these models are not suited to accurately predict high frequency phenomena.

Consequently, researchers have been proposing new approaches. Some are extensions of the well-known ‘low frequency equivalent circuit’ of the induction motor (see Fig. 2.1), others are based on transmission line theory. This thesis will focus on transmission line models in order to evaluate the common mode impedance of the induction machine. Additionally, the model can be used to analyse other motor characteristics, such as high frequency losses and flux distributions.

The parameters of the transmission line model are determined using finite element simulations. The finite element method has become a standard tool in the analysis of electrical machines. The method is well suited for large, complex geometries and nonlinear as well as anisotropic materials [58]. However, the use of standard finite element software for high frequency motor analysis is still not a common practice. Therefore, the applicability of relevant low frequency methods to the high frequency case is critically reviewed in this thesis. In order to provide a reference solution, high-resolution 3D simulations are necessary, which are computationally very demanding. We have developed a specially tailored finite element simulation tool which can solve this specific task more efficiently than most commercially available software.

1.2 Literature Review

In this section, the literature which is most relevant to this thesis is discussed in chronological order. Further works, that have been used, will be cited directly in the corresponding sections.

Surge impedances of electrical machines have been studied already early in the 20th century. Travelling waves in the windings due to switching operation were thoroughly analysed by Ruedenberg in the 1940s [88]. Important work on the subject of harmonics in machines was also published by Jordan, e.g. [43], and Seinsch, e.g. [91].

In 1968 Heller and Veverka published a book named ’Surge Phenomena in Electrical Machines’ [46]. In this monograph, the idea of distributed parameter models of machine coils is used to analyse fast-fronted wave surges, caused by either lightning stroke or switching operation. With the aid of these models, the inhomogeneous voltage distribution along the coils is attributed to the impact of parasitic turn-to-turn and turn-to-ground capacitances.

The authors also advocate the assumption of an eddy-current shield, which can be found in many subsequent publications, e.g. [16]. According to this theory, the eddy currents induced in a thin surface of the iron prevent the electromagnetic field from entering the iron core. As a consequence, coupling between individual slots is assumed to be negligible. This widely accepted statement will be critically reviewed in Sec. 3.3.4 of this thesis. Nevertheless, the theoretical framework of Heller and Veverka is of great importance for the development of machine models suitable for fast time variation. See Table 1.1 for typical rise times of relevant HF phenomena.

phenomena	rise time	citation
standardized lightning waveform	1.2 µs	[46]
IGBT switching	50-200 ns	[81]
electrostatic discharge (ESD)	<10 ns	[37]

Table 1.1.: *Typical rise time of electromagnetic phenomena.*

In 1974 Stoll has published a monograph containing various analytical formula to calculate eddy-current distributions. One approach of great interest for motor analysis is the derivation of an equivalent permeability for a laminated body (see Section 2.2.2). The formulation can be combined with a stacking factor and is very convenient for implementation into finite element (FE) codes. The concept of equivalent permeability can also account for hysteresis, which is proposed in the book [94] as well. The open source FE software *FEMM* [69] offers the aforementioned functionality.

The concept of equivalent permeability is based on the analytical one-dimensional (1D) field solution in an infinitely large plate. By assigning equivalent material properties to a stack of iron sheets, the entire stack is viewed as a homogenized body. A three-dimensional (3D) problem can be reduced to two dimensions. Note, that the concept of frequency-dependent *complex valued reluctivity* $\underline{\nu} = 1/\underline{\mu}$ is a very similar approach. It is equally often used with homogenization techniques (e.g. [35]) and was published by Lammeraner and Stafl already in 1966 [60].

However, the eddy currents do not necessarily have to be assigned to magnetic properties. Another common concept is the use of anisotropic conductivity [48]. In reality, the lamination stack has a large, but finite number of sheets. On the top and the bottom of the stack, the magnetic field has considerable components normal to the stacking direction, which cause large eddy-current loops in parallel with the lamination sheets. As a consequence, additional iron losses are caused by the leakage fields, which are analysed, for instance, in [48, 99].

In the year 1996, Chen has proposed a hypothesis to explain the bearing current problem [25]. The increased use of variable-frequency drives in industrial applications has generated cumulated occurrence of bearing failure, which was then related to the pulse-width modulation (PWM) inverters. Chen reveals, that due to induced shaft voltages, circulating bearing currents may be excited and damage the bearings. The research was pursued, among others, by Muetze [75] and Magdun [66], who developed equivalent circuit models in order to predict the bearing voltage ratio (BVR).

At Helsinki University of Technology, the researcher Mäki-Ontto was occupied with a similar topic and developed a descriptive model of eddy-current flow through laminations [65]. He visualised the common mode (CM) current in a structure of five laminations, computed from an axisymmetric two-dimensional (2D) model excited at 30 kHz. The radial displacement current density in the insulation is assumed to be constant. Therefore, the same amount of current is entering each lamination. In the iron, the currents accumulate and flow back to the front end of the motor frame, where the grounding is assumed. In order to account for the eddy-current flow in the laminations, Mäki-Ontto approximated the effect by an additional impedance.

A comprehensive mathematical formulation of the transmission line (TL) model applied to the induction machine (IM) is provided by De Gersem in 2010 [28]. The paper provides valuable insights into the FE implementation, such as the construction of the system matrix or the coupling of the wire voltages via projection matrix. Furthermore, the author emphasises the importance of a lamination model in high-frequency (HF) motor analysis and refers to the lamination model of Mäki-Ontto. In a subsequent paper [29], the same author includes the end-winding analysis into his motor model.

Another recent work on eddy currents in laminations is the doctoral dissertation by Finnish researcher Pippuri from 2010 [83]. The author has extended the 2D FE code of her research group for frequency domain (FD) analysis of an induction motor supplied by a PWM-based inverter. To include the nonlinear magnetic properties into FD analysis, she uses a procedure similar to the two-step method described in Section 4.5.5.

Finally, the book of Boldea and Nasar from 2010 [16] should be mentioned as a reference to state-of-the-art IM analysis. In a subchapter dedicated to HF phenomena, again, the single slot analysis of the stator is advised, assuming the coupling between slots being negligible. As can be seen in Fig. 3.4, this is not always the case.

1.3 Aim of the Work

Although finite element (FE) simulations of electrical motors are a widely accepted design tool, the consideration of eddy currents inside the core laminations remains a challenging topic. Practically oriented modelling methods are especially needed for analysis of high-frequency (HF) excitation, such as PWM-related common mode (CM) signals. Unless computing power will increase in the future such that each lamination in the motor is easily discretised, homogenization methods are a reasonable compromise. However, their accuracy has to be verified for use in motor simulations. We aim to contribute in this subject by comparing a fast and effective two-dimensional (2D) method to an elaborate three-dimensional (3D) analysis of a real motor geometry.

The transmission line (TL) approach is often used implicitly when analysing a motor cross-section. However, TL theory is based on certain assumptions, which have to be reviewed carefully, especially when considering non-ideal, e.g. lossy or inhomogeneous, structures. Further, the TL model provides the, often, missing link between circuit and field models of a machine. Therefore, TL theory is discussed thoroughly with special regards to the induction machine (IM).

This thesis is focused on practical oriented methods, which aim to provide a comprehensive approach to HF motor modelling, including end-windings and nonlinear behaviour. The numerical methods are described concretely in order to illustrate their implementation. Computational examples and results finally give a good impression of the realisation of the proposed methods.

1.4 Scientific Contributions

The scientific contributions of this thesis may be summarized as follows:

1. Typical high-frequency (HF) finite element (FE) analysis of motor winding is restricted to the cross-sectional area of one stator slot. In this thesis, the magnetoquasistatic (MQS) analysis of the motor is extended from a single slot to the entire motor cross-section.
2. The lamination is analysed by means of elaborate three-dimensional (3D) simulations with explicit modelling of eddy-current fields. Results are taken as a reference solution for the investigation of two-dimensional (2D) homogenization approaches and their accuracy in a wide frequency range.
3. A 3D FE simulation code is adapted and optimized for efficient impedance matrix calculations of large motor geometries. The implementation of periodic boundary conditions will further reduce the problem size.
4. An extension of the simulation method is proposed in order to include saturation effects in the laminations.

5. The common mode impedance of a 240 kW induction motor is calculated from the results of electromagnetic (EM) field analysis. The computational scheme, based on TL theory, is implemented in MATLAB® and allows for quick analyses.
6. End-winding geometries are analysed by means of 3D simulations. The influence of modelling the end-region laminations and the rotor on the end-winding inductance is investigated.

Intermediate steps of the research have been presented in the following publications: [106–112].

1.5 Software

An overview of the software used for this thesis is shown in table 1.2. The finite element (FE) code, which was used for the three-dimensional (3D) motor analysis, will be referred to as *sfem* code. It was created by Dr. Erion Gjonaj as a multi-purpose simulation tool based on finite elements. Details on the formulation are explained in Sec. 4.5.

software	description
sfem code	3D FE simulation code (FD)
SALOME	mesh generation
ParaView	data visualization
FEMM	2D FE simulation software (FD)
CST EM Studio®	3D simulation software (TD and FD)
MATLAB®	numerical evaluation of TL model

Table 1.2.: *Overview of software tools employed in the research.*

In the course of this thesis, the *sfem* code has been adapted to the special purpose of efficient impedance calculation of a large 3D motor model (see Secs. 4.5.2 ff.). Commercially available FE software cannot be modified in its computational procedures. Therefore, it was found to be unsuitable for the elaborate, but repetitive analysis of the high-frequency (HF) induction motor model. The *sfem* tool, on the other hand, provides full access to the C++ code and allows for adjustments to a specific problem. Moreover, the *sfem* code supports distributed-memory parallel operations and, hence, allows to run our large simulations on the TEMF computing cluster[1].

The FE meshes were generated using *SALOME* v5-v6 for Linux 64 bit and *SALOME* v6 for Microsoft® Windows® 32 bit. *SALOME* is an open-source software that provides a generic platform for Pre- and Post-Processing for numerical simulation [1]. Meshes can be constructed via graphical user interface (GUI) or Python script.

ParaView was used for visualization of field plots. The open-source software was developed to analyse extremely large datasets using distributed memory computing resources [3].

2D FE analysis in the FD is performed with *FEMM* [69]. *FEMM* employs a homogenization formula, which provides a fast method to account for laminated materials. The accuracy of this

---

[1] 172 nodes, 2,064 cores, 21.89 TFlop/s, parallel computing with MPI.

approach is investigated for an induction motor for a wide frequency range (see Sec. 5.5.2). Additionally, *FEMM* offers the possibility to include nonlinear and hysteretic material behaviour into frequency domain (FD) analysis. The nonlinear feature is used in Sec. 5.5.3 to determine the permeability distribution in the motor. *FEMM* is a Windows® program written in C++ . The source code is available on the website and may be customized, e.g. for additional post-processing routines.

CST EM Studio® is a commercially available software package, which provides a variety of 2D and 3D solvers suited for static and low frequency problems [4]. The software was used by the author for fast and reliable calculations of relatively small test problems.

MATLAB® is appreciated as a convenient numerical computing environment and provides manipulation functions for matrices of moderate size. For this reason, it was used for implementation of the common mode (CM) impedance calculation procedure (see Sec. 3.3.6).

1.6 Outline of the Thesis

The first chapter introduces the reader to the topic of high-frequency (HF) motor modelling and defines the research area of this thesis. Section 1.1 describes the common mode (CM) circuit of an induction machine (IM) and its relation to bearing currents. Publications on HF motor modelling are reviewed in Section 1.2. For the realisation of the proposed methods, a variety of software tools is employed. An overview is given in Section 1.5.

In Chapter 2, common aspects of IM modelling are introduced and their relevance for HF analysis is discussed. In order to analyse the machine, it is divided into subregions, as explained in Section 2.1. Section 2.2 takes a closer look on the material properties of electrical steel sheets, which are assembled to form the motor core. See Section 2.2.1 for practical approaches to compute iron and copper losses. The derivation of the equivalent permeability formulation from the analytical solution of eddy-current distribution in a conductive sheet is explained in Section 2.2.2. The formation of the CM voltage is an undesired side effect of pulse-width modulation (PWM). See Section 2.3 for a sketch of the Insulated Gate Bipolar Transistor (IGBT) inverter and further details. In our modelling approach, the end-winding fields of the motor are considered separately by means of three-dimensional (3D) finite element (FE) analysis. The construction of the models is described in Section 2.4.

The transmission line (TL) approach of our motor model is explained in Chapter 3. Starting from the basic TL equations in time domain (see Sec. 3.1) and in frequency domain (FD) (see Sec. 3.2), the applicability to motor models is discussed in Section 3.3. The handling of the multiconductor formulation in Section 3.3.1 and the derivation of circuit parameters from the electromagnetic (EM) field (see Secs. 3.3.3 - 3.3.5) are some interesting highlights. Furthermore, it is worth discussing the computation of the CM impedance, which, due to the high number of conductors, is formalized in terms of matrix equations (see Sec. 3.3.6).

Chapter 4 is dedicated to another key topic of this thesis, the analysis of the HF EM fields inside the motor. MAXWELL's equations are introduced in Section 4.1. However it is not necessary in our approach to use them to their full extent. They can be simplified under certain assumptions as explained in Sections 4.2 - 4.4. The discussion of boundary conditions (see Sec. 4.4.1) is crucial in the procedure of EM field analysis, as they specify our particular EM problem. The method is used to determine the fields in our motor models. Formulations and the implementation into our code are described in Section 4.5. Special features of the code, namely the direct impedance matrix extraction (see Sec. 4.5.3) and the implementation of periodic boundary conditions (see Sec. 4.5.4), followed by a method to consider nonlinear material properties in FD simulations, conclude this chapter.

The numerical results of this work, for small test models, as well as for an existing 240 kW induction machine, are presented in Chapter 5. High-order basis functions are used in Section 5.4. Most section titles are self-explanatory. Regarding the motor analysis (Sec. 5.5), the results refer to the theoretical methods described in the previous chapter. A highlight of Chapter 5 might be the field plots of the induction motor (see Figures 5.11 and 5.21).

Finally, in Chapter 6, the results of this work are summarized and ideas for future research topics are presented.

2 Motor Modelling

2.1 Approaches to Motor Modelling

The well-known T-equivalent circuit model of an induction machine (Fig. 2.1) is a single-phase representation of the three-phase system in a steady-state balanced-load condition, where excitation, motor geometry and load are assumed to be symmetric with respect to the three phases. The model describes the electrical behaviour of the machine under ideal operating conditions.

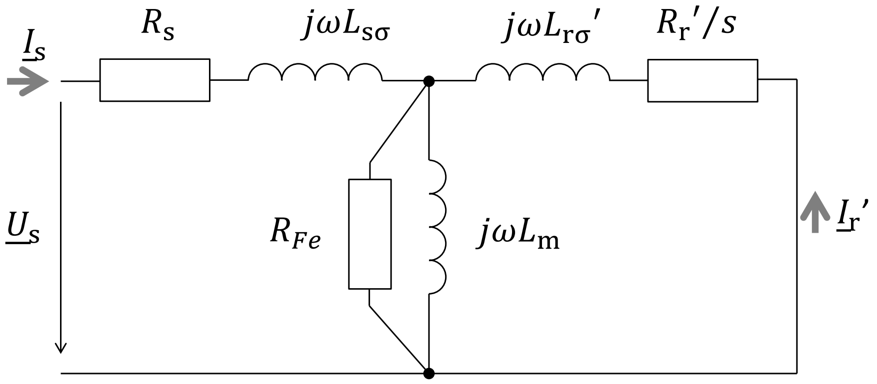

$\underline{U}_\mathrm{s}$ stator voltage
$\underline{I}_\mathrm{s}$ stator current
R_s stator resistance
ω st. angular frequency
$L_{\mathrm{s}\sigma}$ st. leakage inductance
s slip
L_m magnetizing inductance

referred to stator side:
$\underline{I}_\mathrm{r}'$ rotor current
R_r' rotor resistance
$L_{\mathrm{r}\sigma}'$ r. leakage inductance

Figure 2.1.: *Single-phase T-equivalent circuit of squirrel-cage induction machine (LF model).*

The slip is defined as $s = f_1/f_2$, where f_1 is the frequency of stator current and voltage and f_2 is the frequency of induced rotor current and voltage. The rotor frequency is related to the mechanical speed of the rotor as $f_2 = f_1 - p \cdot n_\mathrm{mech}$, where p is the number of pole pairs and n_mech is the mechanical speed of the rotor in revolutions per second.

When the motor is controlled by a frequency converter, an additional common mode (CM) voltage occurs between the terminals and ground. The CM voltage is not sinusoidal but contains a wide range of frequency components up to the Megahertz range. The upper end of this range is defined by the short rise and fall times of the IGBT collector to emitter voltages and the associated high $\mathrm{d}u/\mathrm{d}t$ applying at the motor terminals.

The T-equivalent circuit model is mainly used for description of machine behaviour at power frequencies. A modified version of the single phase model is also used for the analysis of higher harmonics [96]. However, the propagation of common mode signals through the motor is substantially different from the propagation of symmetric three phase signals. As a consequence, the equivalent circuit model shown in Fig. 2.1 cannot be used for the analysis of common mode excitation.

In the analysis of high-frequency common mode effects, parasitic capacitances, created by the winding insulation, have to be considered. They provide a low-impedance path from the conductors to the iron lamination, which is grounded via the stator. The high frequency equivalent circuit of the motor is sometimes represented by a set of parasitic capacitances added to the three phases of a motor [44] (see Fig. 2.2) or even by purely capacitive models [82]. However, these kind of models are not sufficiently detailed for our purposes. We aim to investigate the common mode current distribution inside the motor, which is necessary in order to predict circulating bearing currents.

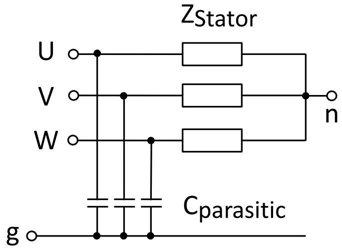

Figure 2.2.: *Simplified representation of the common mode circuit of a three-phase motor.*

In our approach, we will determine the frequency-dependent common mode impedance $Z_{\mathrm{CM}}(f)$ using transmission line theory and electromagnetic field simulations. $Z_{\mathrm{CM}}(f)$ fully characterizes the common mode behaviour of the system in frequency domain. The model includes the impedances of the windings, coupling impedances between individual conductors and capacitances between conductors as well as between conductors and ground (see Fig. 3.2).

The complexity can be significantly reduced, if the motor is divided into three parts, namely the core section and the two end-winding sections. The core section, also called the active part of the motor, can be approached by transmission line (TL) theory exploiting axial periodicity of the electromagnetic fields (see Chapter 3). The parameters of the TL model are determined by electromagnetic field analysis (see Chapter 4). The end-windings are analysed in a separate model (see Sec. 2.4). They are characterized by a set of inductances, which can be combined with the TL parameters into a comprehensive motor model.

The induction motor is a rotating machine. The circuit model (Fig. 2.1) accounts for motion effects by incorporating a slip dependent resistance R'_r/s. However, the circuit parameters are often identified from either analytical calculations or mechanically static, i.e. $n_{\mathrm{mech}} = 0$, finite element simulations. On the one hand, this is possible because the stator parameters R_{s} and $L_{\mathrm{s}\sigma}$ are nearly independent of rotor speed. On the other hand, rotor parameters R'_{r} and $L'_{\mathrm{r}\sigma}$ are mainly dependent on the relative frequency f_2 instead of the absolute value of n_{mech}. The trick is done by supplying the stator with a frequency $f_1 = f_2$ and keeping the rotor at rest ($n_{\mathrm{mech}} = 0$).

In 2D transient analysis of an induction motor, it is also possible to consider motion explicitly. However, simple usage of the term $\vec{v} \times \vec{B}$ is neglecting the effect of the slots [10]. More general methods are using two referential systems, one for the stator, one for the rotor. The relative movement of the referential systems is evaluated in the airgap, e.g. by a moving band technique [10].

In our analysis, the effects of the moving rotor on high-frequency (HF) fields are neglected. In other words, HF simulations are performed assuming a rotor at rest. The possibility to include motional effects is discussed in the Appendix A.1. Further, in frequency domain, we can only analyse periodic fields at a chosen frequency. In this way, it is not possible to consider a time-dependent rotor position. A fixed rotor position was chosen. The transmission line parameters in our model are slightly varying depending on the chosen rotor position, but the effect was found to be negligible.

2.2 Electrical Steel Sheets

Electric machines are equipped with magnetic cores in order to guide magnetic flux, which is important to obtain compactness and effectiveness of the device. The magnetic material, most commonly used in machines, is electrical steel sheet. It is manufactured in the form of cold-rolled strips, usually less than one millimetre thick. The sheets are stamped out in shapes and stacked to form the core. The stacking factor F accounts for the insulating coating and for air inclusions between the sheets. It is calculated as the ratio of theoretical sheet volume to measured volume of the stack. Modern processing techniques allow filling factors in the range of $F = 0.98$. The individual laminations are electrically insulated from each other. Therefore, eddy currents with a skin depth δ larger than half the sheet thickness (see Section 2.2.2) are suppressed.

The steel sheet is made of an alloy of iron and around 3.5 % silicon customized to produce the desired electromagnetic properties, such as small hysteresis area and high permeability. Silicon increases resistivity of the steel, which is desirable to lower eddy-current loss. In the processing of the sheets the crystal orientation can be controlled. Non-oriented steels are nearly isotropic. They are suitable for use in rotating machines, i.e. motors and generators. On the other hand, grain oriented sheets have a higher permeability in the rolling direction and are used in transformers.

Iron, and most of its alloys, respond strongly to magnetic fields, thus, they are classified as ferromagnetic. Soft and hard ferromagnets are distinguished. ‘Hard’ refers to a wide hysteresis loop. Once magnetized by a large external field, the specimen can be used as a permanent magnet. Soft ferromagnetic materials, such as electrical steel, are easily magnetized but most of this property disappears when the external field is removed.

Ferromagnets are composed of elementary magnets, called Weiss domains. The domains are separated by transition regions, called Bloch walls. At thermodynamic equilibrium, which is the lowest energy condition, domains arrange in a way to minimize the static magnetic field outside the specimen. Therefore, the material is magnetised inside individual domains, but seems neutral from the outside. The development of magnetic domain theory is mainly attributed to [61] and [101] .

When demagnetized iron is exposed to an external magnetic field, three stages in the magnetization curve $M = M(H)$ are distinguished. At low field, reversible Bloch wall displacement is initiated. As the applied field strength increases, domain walls are irreversibly displaced. When further domain wall movement becomes impossible, the remaining domain magnetisation is rotated to align with the external field. The latter process requires large energy and the slope of the M-H curve flattens. When all magnetic moments are aligned, saturation is reached.

The curves of magnetic polarization $M(H)$ and magnetic induction $B(H)$ are equivalent expressions since

$$\vec{B} = \mu_0(\vec{H} + \vec{M}), \tag{2.1}$$

with μ_0 being the vacuum permeability. Exposed to alternating field, the B-H relationship follows a hysteresis loop. However, for technical applications, manufacturers usually provide a single valued curve $B = B(H)$. An example is shown in Fig. 2.3.

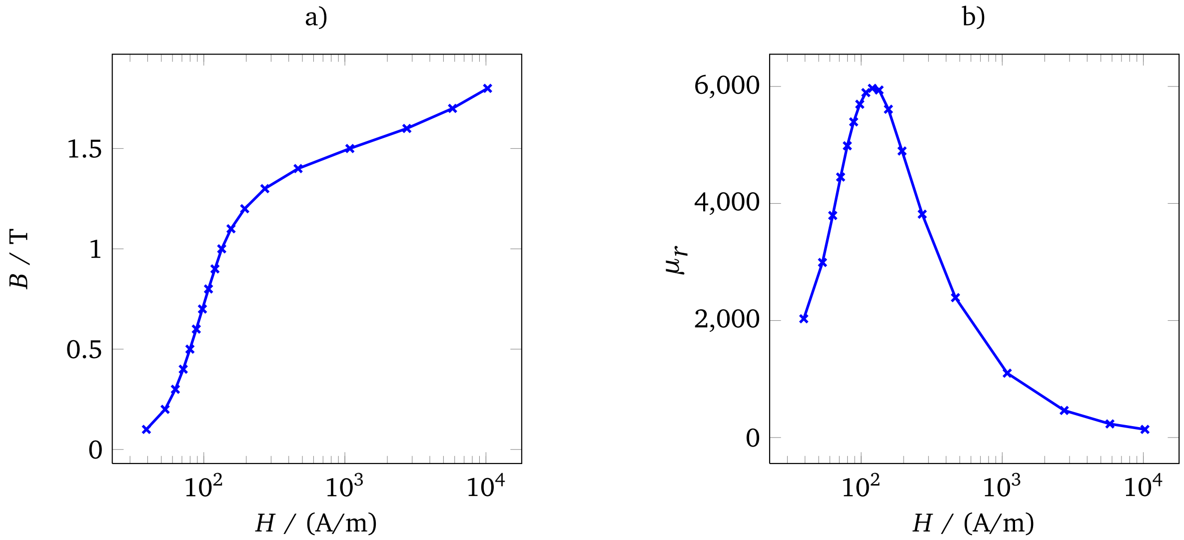

Figure 2.3.: *a) Magnetization curve of Sura® M530-65A, b) relative permeability.*

In general, the magnetic properties of steel sheets do not only depend on the magnitude of applied field, but also on the rate of change (e.g. [12]), the magnetization direction (e.g. [33]), applied stress (e.g. [11]) and temperature. Electrical machines heat up significantly when operated, e.g. from 25°C to 85°C. The electric resistivity of the material increases with temperature and the total core loss decreases by a few percent.

2.2.1 Iron Loss Models

The B-H relationship of a ferromagnetic material is often described by a nonlinear multivalued function, called the static hysteresis curve. This curve is measured at a very low frequency, typically <1 Hz. The H-field is increased until saturation of the B-field is reached. Therefore, the curve is also called the major hysteresis loop. The area enclosed by the loop equals the energy which is necessary to perform one full magnetization cycle. Hence, the static ('DC') hysteresis loss yields

$$p_{\mathrm{DC}} = \oint \vec{H} \cdot \mathrm{d}\vec{B}. \tag{2.2}$$

Unfortunately, the static curve does not fully characterize the magnetic response of the material. The actual B-H relationship depends on the sequence of former field extrema [13]. If the material is not taken to saturation before the field direction is reversed, minor loops are formed. The behaviour can be described mathematically by so called static hysteresis models, e.g. by Preisach [85] or Jiles-Atherton [54].

Owing to the complexity of nature, the hysteresis curve is also frequency dependent. It widens as frequency increases. This behaviour is attributed to eddy-current loss. In order to describe the problem mathematically, the loss is separated into rate-independent hysteresis loss P_{hy} and frequency-dependent eddy-current loss P_{ed}. The classical eddy-current computation, based on MAXWELL's equations, has been shown to underestimate the dynamic loss [12]. Therefore, an additional loss component, so-called excess loss P_{ex}, is included into the mathematical description of iron loss. The physical explanation of this component are additional eddy-current components due to the microstructure of the magnetic material. The total iron loss is the sum of the three components,

$$P_{\mathrm{iron}} = P_{\mathrm{hy}} + P_{\mathrm{ed}} + P_{\mathrm{ex}}. \tag{2.3}$$

Soft ferromagnetic materials have a narrow hysteresis loop, which is not represented in the technical magnetisation curve, Fig. 2.3. However, hysteresis loss is one of the main loss components in electrical steels. It is usually computed from the measured static loop loss per volume (Eq. 2.2) multiplied by the frequency of excitation f. Each measurement point is related to a specific induction level $\hat{B}$. With reference to the empirical STEINMETZ equation from 1890 [93], hysteresis loss per volume can be approximated as

$$\frac{p_{\mathrm{hy}}}{\mathrm{W/m^3}} = C_{\mathrm{hy}} \cdot \frac{f}{\mathrm{Hz}} \cdot \left(\frac{\hat{B}}{\mathrm{T}}\right)^{\alpha} \tag{2.4}$$

where C_{hy} is a fitting parameter and α is a coefficient between 1.6 and 2.

The second component in the loss separation theory, the eddy-current loss, is proportional to the square of induction, frequency and sheet thickness $2d$. The classical formula [12] is

$$p_{\mathrm{ed}} = \pi^2 \kappa (2d)^2 \left(f\hat{B}\right)^2 / 6, \tag{2.5}$$

where κ is the electric conductivity of the material. In this formula, the frequency is assumed to be low enough to neglect the skin effect, i.e. $\delta > d$. For engineering purposes, the total loss is usually measured at 50 or 60 Hz. Hysteresis loss is subtracted and the remaining loss is attributed to eddy currents.

In science, the excess loss is considered separately. It may be even larger than the classical eddy-current loss and was empirically determined [12] as

$$\frac{p_{\mathrm{ex}}}{\mathrm{W/m^3}} = C_{\mathrm{ex}} \cdot \left(\frac{f}{\mathrm{Hz}} \cdot \frac{\hat{B}}{\mathrm{T}}\right)^{1.5}, \tag{2.6}$$

where C_{ex} is a fitting parameter.

In finite element (FE) simulations, the nonlinear behaviour is either approximated by a single valued curve, corresponding to Fig. 2.3, or even linearized, by determining a constant permeability value. A constant permeability enables the use of linear system theory and a convenient description in the frequency domain (FD), provided that the excitation is sinusoidal. In order to simplify the calculations, eddy currents and nonlinear behaviour are often omitted in the simulation. Iron loss is approximated in the post-processing using Eqs. 2.4-2.6.

Nonlinear systems generate nonsinusoidal output, even if the input is a sinus. Hence, they constitute a time-dependent problem. The output of a nonlinear system can be calculated by time-stepping methods, which update the field dependent parameter $\mu(H)$ in each time step.

The inclusion of hysteretic behaviour into the calculation can also be achieved in time-domain calculations. However, it requires the implementation of a hysteresis model into the simulation procedure, which, simply speaking, accounts for the branching in the hysteresis loop.

Many publications can be found on magnetic hysteresis modelling, from a mathematical point of view [68] as well as from the point of practical application [12]. The main problem in hysteresis modelling can be identified as constructing an accurate representation of the B-H curve from a limited amount of measured data. Recently, the employment of neural networks (e.g. [59, 67]) has shown to complement classical Preisach-type hysteresis models.

It was observed from measurements that hysteresis loss due to rotational flux is different to loss from alternating flux [19], the latter being implicitly assumed by scalar models. Electrical machine cores are exposed to both flux types. Therefore, vector hysteresis models have been applied [31, 33].

Even though hysteresis loss is mainly attributed to the fundamental field components, higher harmonics in the flux lead to so-called minor loops which complicate accurate loss prediction. The subject has been recently analysed in a number of publications, e.g. [52, 87].

Naturally, as dealing with a nonlinear phenomenon, most iron loss models in the literature, tackle the problem in time domain. Implementation of these methods is beyond the scope of our research, which is focused on high-performance FD methods. Therefore, in Sec. 4.5.5, a FD domain method will be presented, which includes magnetic saturation effects while preserving the advantage of efficient FD simulations.

2.2.2 Eddy Currents in Laminations

Eddy currents are closed loops of induced current, circulating in all conductive media exposed to a time-varying magnetic flux $\mathrm{d}B/\mathrm{d}t$. As explained in the previous section, machine cores are laminated in order to suppress eddy currents. The associated loss can be minimized by making the sheets as thin as possible, but remains an important component in the overall machine loss. As a consequence, it is necessary to account for the laminated structure of the iron core, when the electromagnetic field of a machine is analysed by means of finite element (FE) simulations.

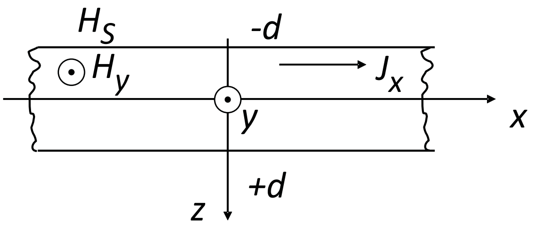

Figure 2.4.: *1D eddy-current problem.*

In low-frequency (LF) motor analysis, 2D models of the motor cross-section are state of the art. However, in 2D FE simulations, eddy currents in the laminations cannot be modelled explicitly. By definition, currents flowing in the simulation plane are excluded. A common approach is to discard the electric conductivity κ of the laminated material in the simulation and account for losses in the post-processing using Eqs. 2.4, 2.5 and possibly 2.6. In this procedure the skin effect in the individual sheets is assumed to be negligible. The assumption is valid if the skin depth

$$\delta = \sqrt{\frac{1}{\pi f \kappa \mu}} \tag{2.7}$$

is larger than half the sheet thickness d. The variable f denotes the frequency, κ and μ denote the electric conductivity and the magnetic permeability of iron, respectively. The example of skin depths presented in Table 2.1 shows, that the skin effect may be important, even at relatively low frequencies. The variable μ_r denotes the relative permeability of iron.

	f /Hz	δ/mm
$d = 0.325$ mm	50	0.57
$\mu_\mathrm{r} = 6000$	200	0.28
$\kappa = 2.63$ MS/m	1000	0.13

Table 2.1.: *Skin depths in electrical steel sheet.*

The one-dimensional (1D) eddy-current problem is represented in Fig. 2.4, where H_S denotes the magnetic field strength on the surface. The corresponding 1D diffusion equation reads

$$\frac{\mathrm{d}^2 \underline{H}_y}{\mathrm{d}z^2} = \kappa\mu \frac{\mathrm{d}\underline{H}_y}{\mathrm{d}t}, \tag{2.8}$$

where $\underline{H}_y$ denotes the y-component of the magnetic field strength $\underline{\vec{H}}$, z denotes the z-coordinate and t denotes time. The assumption of sinusoidal time variation allows to substitute $\mathrm{j}\omega$ for $\mathrm{d}/\mathrm{d}t$. The symbol j denotes the imaginary number and ω denotes the angular frequency. The analytical solution leads to the distribution of eddy currents, well known from university lectures:

$$\underline{J}_x(z) = -\frac{\mathrm{d}\underline{H}_y}{\mathrm{d}z} = \underline{\alpha} H_\mathrm{S} \frac{\sinh(\underline{\alpha} z)}{\cosh(\underline{\alpha} d)} \quad \text{with} \quad \underline{\alpha} = (1+\mathrm{j})/\delta, \tag{2.9}$$

where $\underline{J}_x$ is the x-component of the complex current density $\underline{\vec{J}}$. By averaging the associated magnetic flux density over the thickness $2d$ of the lamination, an expression for equivalent permeability is derived [94]:

$$\underline{\mu}_\mathrm{eq} = \frac{\mu_0 \mu_\mathrm{r}}{\underline{\alpha} d} \frac{\sinh(\underline{\alpha} d)}{\cosh(\underline{\alpha} d)}, \tag{2.10}$$

where μ_0 denotes the permeability of vacuum. Using this formula, the lamination stack can be homogenized in the stacking direction and the essentially 3D problem is reduced to 2D. However, the shortcomings of using an analytical 1D formula to solve a 3D problem have to be considered. First, the actual motor lamination is large but not infinite, therefore, edge effects will occur. In fact, the analytical formula (2.10) only considers eddy currents transversal to the plate. On edges, the eddy current vector has to turn toward transversal direction. Although, the iron sheets of a motor are indeed much larger than thick, edge effects might play an important role in the teeth of the stator core, where magnetic flux is typically highest. The second effect of a 3D field distribution, that is not considered by the 1D approach, is the gradient of magnetic field along the surface of a plate. The numerical results of small scale tests are presented in Section 5.3.

2.3 Pulse-Width Modulation Inverters

Variable-frequency drives (VFDs), also known as adjustable-speed drives, allow for operation of induction machines under optimal conditions with regards to load requirements and energy savings. The drive converts alternating current (AC) power from the supply into direct current (DC) and back to AC of desired amplitude and frequency, see Fig. 2.5. One of the prevalent methods to vary the inverter output voltage is pulse-width modulation (PWM) control. Amplitude and frequency are entirely controlled by the modulation strategy: The DC link voltage U_{DC} is applied to the motor in short pulses by turning the semiconductor switching devices, e.g. Insulated Gate Bipolar Transistors (IGBTs), on and off. A time-dependent average value, corresponding to the desired waveform, is obtained.

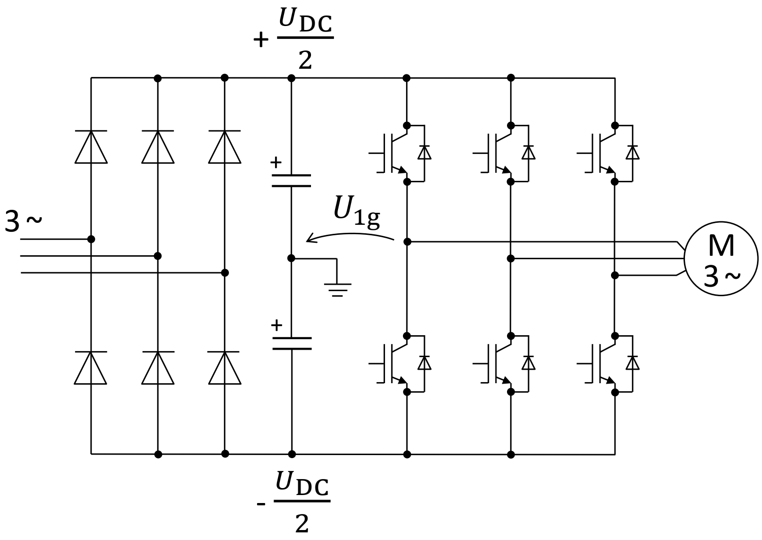

Figure 2.5.: *IGBT motor drive.*

The underlying principle of pulse-width modulation (PWM) is to vary the pulse width while the switching frequency may be constant or variable. Precisely, there are many PWM schemes, e.g. sinusoidal PWM, regular PWM and optimal PWM. For details the reader is referred to [27]. The appropriate scheme is selected with regards to minimum harmonic distortion of the output voltage, hardware and software requirements, real-time capability, tolerance toward the energy source and other factors [24].

It is also a common practice to change the switching scheme according to the particular operating point of the induction machine. For example, fundamental frequency switching (also known as six-step mode or block mode) is often used in electric and hybrid vehicle applications at high motor speed [51,72]. Fundamental frequency switching can be seen as a PWM with a switching frequency reduced to the fundamental frequency or a modulation index approaching infinity.

Conventional voltage source inverters produce a significant common mode (CM) voltage due to discrete switching. The instantaneous value of U_{CM} equals the motor stator neutral-to-ground voltage and can be expressed as

$$U_{\mathrm{CM}}(t) = \frac{1}{3}(U_{1g}(t) + U_{2g}(t) + U_{3g}(t)), \tag{2.11}$$

where U_{1g}, U_{2g}, U_{3g} are the phase-to-ground voltages.

In case of pure sinusoidal voltage excitation, U_{CM} would be zero, but since the inverter output voltages are discrete values, U_{CM} takes the values $\pm U_{\mathrm{DC}}/6$ and $\pm U_{\mathrm{DC}}/2$ depending on the switching state. Steep slopes of voltage waveforms, due to short rising and falling times of the semiconductor switches, especially when using IGBTs, are adding a high-frequency (HF) spectrum to the CM voltage. This fact is associated with the occurrence of bearing currents and electromagnetic interference issues [75]. In order to capture the phenomena correctly, appropriate HF models of the motor are needed. Subsequently, the causes may be approached by suppressing CM voltages or cancelling CM currents. Several methods to alleviate the problem have been proposed in the literature, e.g. four-leg inverters, filters and modified switching patterns [77].

2.4 End-Windings

The purpose of the end-winding is to provide a safe electrical connection between bars and coils in the stator or rotor of a machine [95]. End-winding inductance is contributing to the leakage inductance of the machine. Leakage flux is linking either the stator or the rotor windings and, therefore, not contributing to the main reactance. End-windings have been of particular interest in the analysis of large turbo generators [89, 90]. By contrast, in a typical induction machine, only a very small portion of the total flux is associated with the end-winding region. Hence, end-winding inductances are often neglected in steady state analysis. However, during transient operation, e.g. startup, of a machine, the core may become deeply saturated, which increases the influence of end-winding inductances on the overall inductance of the machine. Leakage reactance is important to limit the starting current of the motor and also short circuit currents. On the other hand, a low leakage inductance increases the pull-out torque of the induction machine [16]. Knowledge of pull-out torque and slip is also important for motor control.

High frequency end-region fields have been found to affect eddy-current loss in the windings, core ends and other surrounding metal parts [63]. Moreover, a larger leakage reactance reduces current harmonics [96].

The magnetic field of end-windings follows a complicated 3D pattern. Prior to the use of numerical field simulation, many sophisticated analytical and semi-analytical methods have been proposed, e.g. [22, 49]. Practically, so-called geometric permeance factors are used by designers to account for the different coil end shapes and layer types [16]. Nowadays, due to increased computational resources, 3D simulations of the end-winding regions are possible [26]. Yet, the consideration of eddy currents remains a challenging task.

In this thesis, a 3D modelling approach for the end-region field of an induction machine is presented. The influence of core end, rotor end parts and frame is investigated. Eddy currents are

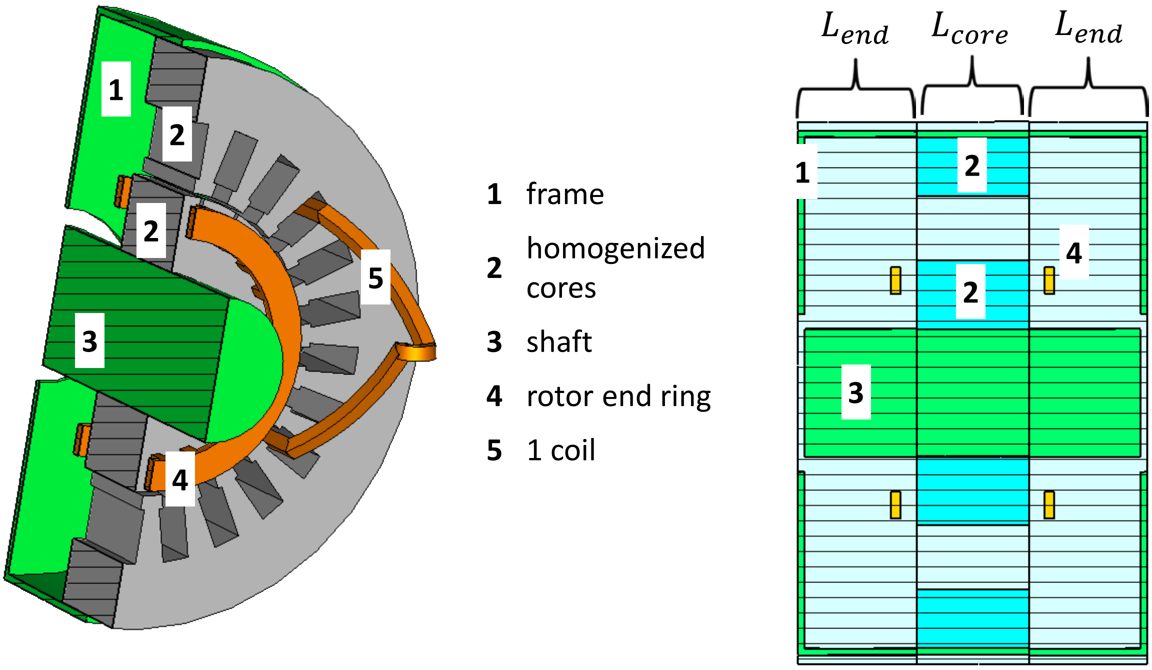

Figure 2.6.: *End-winding geometry of test motor. Images created with CST EM Studio®*

explicitly considered by means of fine discretization of the surface layers of metal conductors. However, simplifications are made: Out of the entire stator winding, only one coil is modelled.

The end-winding inductance is computed from the magnetic field energy in the end region. Flux lines linked with the end-winding currents are mostly closing inside air and other nonmagnetic parts. Therefore, linear analysis in the frequency domain (FD) is suitable.

Figure 2.6 shows one of our end-region models of a fictitious test motor. The motor core is assumed to be merely deep enough to let end effects decay. The outer boundary of the model is the defined by simplified end shields and the motor frame, where the magnetic field is assumed to vanish. In this model a homogeneous anisotropic core was assumed. In other models, presented in Sec. 5.5.5, a few laminations were discretised, in order to obtain realistic eddy-current fields. The end-winding analysis in this thesis is considered a proof of concept and, therefore, has not been carried out for the 240 kW induction motor.

3 Transmission Line Approach

3.1 General Transmission Line Theory

A transmission line (TL) is a system of metal conductors and insulating media that is guiding energy transfer in one dimension. In this work, the direction of the z-axis is chosen. The cross-sectional dimensions of the system are assumed to be small compared to the wavelength of the propagating waves. The basic equations are derived for two-conductor lines. One of them is often viewed as the return path or reference conductor. Therefore, line parameters are only assigned to the remaining conductor. A system of more than two conductors is called a multi-conductor TL. The principles of the two-conductor line can be generalized into matrix equations.

The TL approach is valid for a transverse electromagnetic (TEM) field structure. That means, E- and H-field are perpendicular to each other and transverse to the propagation direction. The TEM mode requires a uniform line with perfect electric conductors (PECs). The surrounding medium has to be homogeneous. Notably, a lossy insulator does not invalidate TEM assumptions.

It can be shown (see Appendix A.2), that a unique voltage between the conductors and a unique current in the given conductor can be defined at any point of the transmission line as

$$\int_{C2} \vec{E} \cdot \mathrm{d}\vec{l} = U, \tag{3.1a}$$

$$\oint_{C1} \vec{H} \cdot \mathrm{d}\vec{l} = I, \tag{3.1b}$$

where $C1$ is a closed contour around the given conductor and $C2$ is an arbitrary contour between the conductors in a transverse plane of the line. Consequently, circuit theory can be used to analyse the structure.

In the ideal TEM mode, field components in direction of wave propagation vanish ($E_z = H_z = 0$). In reality, the finite conductivity of metals introduces certain longitudinal field components. As long as these components are small compared to the transversal fields, the structure can be considered as quasi-TEM. The dynamic state of the TL is determined by the *Telegrapher's* equations

$$-\frac{\partial}{\partial z} u(z,t) = R'\, i(z,t) + L' \frac{\partial}{\partial t} i(z,t), \tag{3.2a}$$

$$-\frac{\partial}{\partial z} i(z,t) = G'\, u(z,t) + C' \frac{\partial}{\partial t} u(z,t), \tag{3.2b}$$

where $u(z,t)$ is the line voltage and $i(z,t)$ the line current at position z and time t. R', L', G' and C' are parameters per unit length for resistance, inductance, conductance of the dielectric material and capacitance, respectively. They can be obtained either from MAXWELL's equations or from circuit theory, as is shown in [62]. Ohmic loss in the metal conductors is considered in Eq. (3.2a) through the per-unit-length resistance R'.

As an important consequence of the (quasi-)TEM assumption, the per-unit-length parameters in Eq. (3.2a) and Eq. (3.2b) are determined by the (quasi-)static field distributions in the cross-sectional area of the line. C' and G' can be obtained from the solution of two-dimensional (2D) electrostatic (ES) and stationary current flow problems, respectively. Resistance and inductance, however, are frequency dependent, due to the fact that alternating currents are not distributed uniformly in the cross section of the conductors (skin effect, proximity effect). Hence, R' and L' are determined through a 2D magnetoquasistatic (MQS) approach.

3.2 Transmission Line Theory in Frequency Domain

Linear time-invariant systems can be analysed conveniently in frequency domain. Every absolutely integrable function of time $f(t)$ is representable as a sum of sinusoidal functions. The Fourier transform

$$\mathscr{F}\left\{\frac{\mathrm{d}f}{\mathrm{d}t}\right\} = j\omega\,\mathscr{F}\{f(t)\} = j\omega\,\mathscr{F}(\omega) \tag{3.3}$$

shows the correspondence between the derivative operator in time domain and the multiplication by $j\omega$ in frequency domain. The TL equations in frequency domain then read

$$-\frac{\partial}{\partial z}\underline{U}(z) = (R' + j\omega L')\,\underline{I}(z) \tag{3.4a}$$

$$-\frac{\partial}{\partial z}\underline{I}(z) = (G' + j\omega C')\,\underline{U}(z) \tag{3.4b}$$

with $\underline{\mathrm{U}}$ and $\underline{\mathrm{I}}$ being complex functions of coordinate z. The general solution, using an exponential expression, yields

$$\underline{U}(z) = \underline{C}_1 e^{\underline{\gamma} z} + \underline{C}_2 e^{-\underline{\gamma} z} \tag{3.5a}$$

$$\underline{I}(z) = \frac{\underline{\gamma}}{R' + j\omega L'}\left(\underline{C}_1 e^{\underline{\gamma} z} - \underline{C}_2 e^{-\underline{\gamma} z}\right) \tag{3.5b}$$

with the complex propagation constant

$$\underline{\gamma} = \sqrt{(R' + j\omega L')(G' + j\omega C')} \tag{3.6}$$

and $\underline{C}_1$ and $\underline{C}_2$ being arbitrary complex constants. The equivalent circuit of a line with distributed parameters is shown in Fig. 3.1.

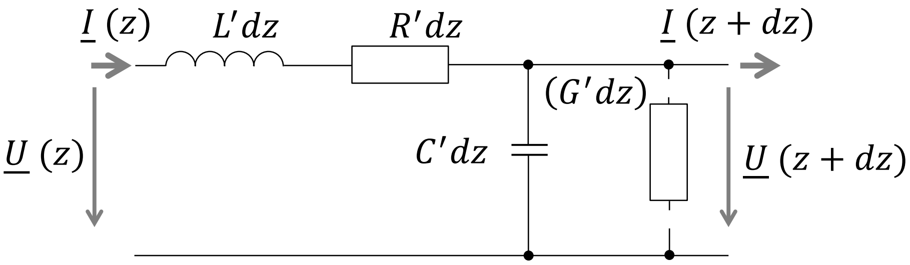

Figure 3.1.: *Circuit model of TL with distributed parameters (G' can be omitted in motor analysis).*

3.3 Application to the Induction Motor

In HF motor analysis, analytical methods are often combined with numerical simulations. A full-wave simulation of the entire motor would be desirable, but is, at present, not an available option. One of the main obstacles are eddy currents, which flow in thin layers on the surface of winding conductors and iron lamination. Their influence on the HF behaviour of the motor cannot be neglected. An appropriate discretisation of the geometry will easily lead to billions of mesh cells. Therefore, the motor is divided into subregions. Analytical methods are sometimes used to compute parasitic capacitances, e.g. [75], or end-winding inductances, e.g. [63]. Numerical methods can be employed universally. However, it remains a difficult task to find an appropriate representation of the entire motor.

A common approach is to find some circuit representation more or less intuitively and assign the parameters through a curve fitting process based on measurements. Obviously, this method has some major disadvantages. First, a prototype of the motor is imperative for the measurements and, second, the physical fields inside the motor remain unknown.

As an alternative, transmission line (TL) theory is a versatile tool which can be applied to transverse electromagnetic (TEM) or quasi-TEM structures. The copper conductors in the slots of the stator core of an induction machine can be viewed as such a structure. A (quasi-) TEM wave is propagating in the insulation space surrounding the conductors.

3.3.1 Multiconductor Formulation

The state of a multiconductor line can be described by the transmission line (TL) equations in matrix notation as

$$\frac{\mathrm{d}}{\mathrm{d}z}\begin{pmatrix}\mathbf{u}(z)\\ \mathbf{i}(z)\end{pmatrix}=\begin{pmatrix}0 & -\mathbf{Z}'(\omega)\\ -\mathbf{Y}'(\omega) & 0\end{pmatrix}\begin{pmatrix}\mathbf{u}(z)\\ \mathbf{i}(z)\end{pmatrix}, \tag{3.7}$$

where $\mathbf{Z}'=\mathbf{R}'+j\omega\mathbf{L}'$ and $\mathbf{Y}'=j\omega\mathbf{C}'$ represent the complex frequency-dependent impedance and admittance matrices per unit length, respectively. The vectors $\mathbf{u}(z)$ and $\mathbf{i}(z)$ are the voltage and current vectors, respectively, which depend on the z-coordinate.

The differential equation system (3.7) can be solved using a modal transformation of the system matrix

$$\begin{pmatrix} 0 & -\mathbf{Z}'(\omega) \\ -\mathbf{Y}'(\omega) & 0 \end{pmatrix} = \mathbf{T}\,\mathbf{\Lambda}\,\mathbf{T}^{-1}, \tag{3.8}$$

where **T** is a matrix of the eigenvectors of the system matrix and **Λ** is a diagonal matrix containing the eigenvalues. The solution of the system (3.7) then reads

$$\begin{pmatrix} \mathbf{u}(z) \\ \mathbf{i}(z) \end{pmatrix} = \mathbf{T}\exp\left(\mathbf{\Lambda}\, z\right)\, \mathbf{T}^{-1}, \tag{3.9}$$

where $\exp(\mathbf{\Lambda}\, z)$ is the matrix exponential of a diagonal matrix, which equals the element-wise exponential of the diagonal elements. A comprehensive demonstration of the distributed parameter solution of a multiconductor system is shown in [28].

3.3.2 Lumped Parameter Approach

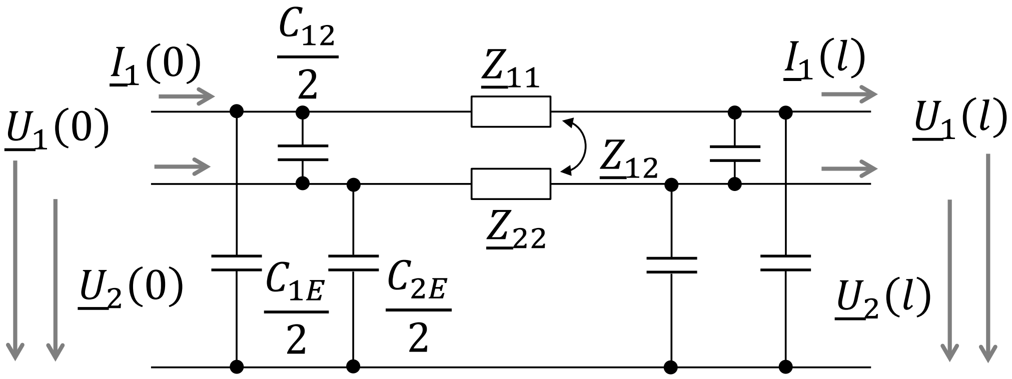

Figure 3.2.: *Pi-equivalent circuit of two-conductor TL with lumped parameters.*

Owing to the relatively short motor core length of about 35 cm, which is much smaller than the delimiting wavelength[1] of $\lambda_{\text{lim}} \approx 300$ m, the transmission line (TL) parameters can be lumped per conductor. It simplifies the multiconductor TL equation system (3.7) from a differential equation system to an algebraic one. At first, it may seem contradictory to use TL theory on a lumped parameter circuit. However, even though travelling wave phenomena are neglected in our approach, the multiconductor TL model allows for a formal description of coupling between the conductors. The pi-equivalent circuit of a two-conductor line with lumped parameter impedances and admittances is shown in Fig. 3.2.

---

[1] A discussion concerning the wave propagation velocity is given in Appendix A.3.

With the use of KIRCHHOFF's circuit laws, we obtain one voltage and two current equations,

$$\mathbf{u}(0) - \mathbf{u}(l) = \mathbf{Z}\,\mathbf{i}_z, \tag{3.10a}$$

$$\frac{1}{2}\mathbf{Y}\,\mathbf{u}(0) - \mathbf{i}(0) + \mathbf{i}_z = 0, \tag{3.10b}$$

$$-\frac{1}{2}\mathbf{Y}\,\mathbf{u}(l) - \mathbf{i}(l) + \mathbf{i}_z = 0, \tag{3.10c}$$

where $\mathbf{u}(0)$, $\mathbf{u}(l)$, $\mathbf{i}(0)$and $\mathbf{i}(l)$ are the voltage and current vectors at the beginning ($z = 0$) and the end ($z = l$) of the multiconductor TL, which correspond to the front and rear end of the motor, respectively. Each matrix is of dimension ($N \times N$), where N is the number of winding conductors. The vector $\mathbf{i}_Z$ holds the currents through the impedances $\mathbf{Z}$ and can be eliminated by inserting one equation into the others.

3.3.3 Transverse Electric Field

According to the properties of a transmission line (TL) modelling approach, transverse electric and transverse magnetic field can be analysed independently (see Sec. 3.1). The capacitors of the TL network model are determined from electrostatic field distributions in the cross-section of the motor or, more precisely, in the insulating region in between copper winding and iron core.

The conductors of the machine are electrically insulated against each other and the iron slot walls. The insulation material, the so called dielectric, has a very low electric conductivity ($\kappa < 10^{-8}$ S/m). An important property is the relative permittivity, which is $\varepsilon_r = 2...8$ for commonly used insulation materials. The parasitic capacitances of in the machine are increased by a factor $\varepsilon_r > 1$ compared to the same geometry of electrodes in vacuum, due to a process called polarisation.

The electric displacement field can be expressed in two ways

$$\vec{D} = \varepsilon_0 \vec{E} + \vec{P} = \varepsilon_0 \varepsilon_r \vec{E}, \tag{3.11}$$

where $\vec{P}$ is the vector of electric polarisation.

Polarisation in dielectric materials is known to be depending on frequency, electric field strength, temperature and mechanical stress [56]. These influences have been neglected in the modelling process, because most of them are expected to be very small. However, frequency dependency of orientation polarization may be relevant in the frequency range around 1 MHz, as can be seen in Figure 4.2-3 in [56] and should be further investigated in the future.

Additionally, the insulating region in the machine slots is not homogeneously filled with the dielectric. Because of the manufacturing process, the winding is randomly surrounded by air ($\varepsilon_r = 1$). Therefore, in the modelling process, a homogenized material with $\varepsilon_r = 3$ is assumed.

Electrostatic capacitance is defined as the ratio of opposite and equal charge $\pm Q$ on two electrodes and the resulting voltage U between them:

$$C = \frac{Q}{U}. \tag{3.12}$$

The total electrostatic energy stored in one capacitor is

$$W_e = \frac{1}{2} C\, U^2, \tag{3.13}$$

and in the case of a multiconductor system

$$W_e = \frac{1}{2} \sum_{i=1}^{N} \sum_{j=1}^{N} C_{ij} U_i U_j, \tag{3.14}$$

where N is the number of conductors, C_{ij} are the mutual capacitances and U_i,U_j are the voltages between a conductor and the reference potential.

Although it is possible, to obtain the mutual capacitances from Eq. (3.14), the common way to determine a capacitance from the numerical field solution is to use the relation

$$C = \frac{\oint \varepsilon \vec{E} \cdot \mathrm{d}\vec{A}}{\int_1^2 \vec{E} \cdot \mathrm{d}\vec{l}}, \tag{3.15}$$

where the numerator is an integral over the closed surface around electrode 1 and represents the charge Q on this electrode. The integration limits 1,2 denote points on each of the two electrodes forming the capacitor and the integral in the denominator represents the potential difference $U_1 - U_2$.

Transferred to a multiconductor system, a voltage U_i is applied to only one of the conductors, while the other conductors are set to $U_n = 0$. The mutual capacitances are calculated as

$$C_{ij} = \left. \frac{Q_i}{U_i} \right|_{U_n = 0, n \neq i}, \tag{3.16}$$

where Q_i is the charge on the i-th conductor.

In the distributed parameter TL model, the transverse electric field is represented by a matrix of per unit length capacitances

$$C'_{ij} = \frac{C_{ij}}{l} \tag{3.17}$$

with $i, j = 1, .., N$.

3.3.4 Transverse Magnetic Field

A purely transversal magnetic field implies straight wires of infinite length. On the other hand, the inductance definition is usually associated with closed loops or coils. The self-inductance of a closed loop is defined as the ratio of flux through a loop and current through the same loop:

$$L_{ii} = \frac{\underline{\Phi}_i}{\underline{I}_i}, \tag{3.18}$$

where $\underline{\Phi}$ is the complex magnetic flux, which has the same direction in the complex area as the exciting current $\underline{I}$. Therefore, the inductance L is a real-valued quantity. The mutual inductance of two loops relates the flux through the first loop with the current through the second loop and vice versa:

$$L_{ij} = \frac{\underline{\Phi}_i}{\underline{I}_j}. \tag{3.19}$$

The total magnetic energy of a current carrying loop can be expressed in terms of its inductance as

$$W = \frac{1}{2} L \, |\underline{I}|^2. \tag{3.20}$$

In a multiconductor system, the closed current loops can not be separated. Therefore, partial inductances are defined for each segment. The total magnetic energy yields

$$W = \frac{1}{2} \sum_{i=1}^{N} \sum_{j=1}^{N} L_{ij} \underline{I}_i \underline{I}_j^*, \tag{3.21}$$

where N is the number of segments. The variables L_{ij} denote the partial self-inductances if $i = j$ and the partial mutual inductances if $i \neq j$. The currents through the segments are denoted by $\underline{I}_i$ and $\underline{I}_j$, where $\underline{I}_j^*$ denotes the complex conjugate of $\underline{I}_j$. Partial inductances are not physical, as they depend on the gauge choice of the magnetic vector potential. The ‘physical’ loop inductance is calculated from the partial inductances of all segments forming the loop, including the partial mutual inductances.

The ohmic resistance R of a conductor represents the proportionality of power dissipation and the square of the current

$$P = R \, |\underline{I}|^2. \tag{3.22}$$

The DC resistance of a conductor is simply computed as

$$R_{\text{DC}} = \frac{l}{\kappa \, A}, \tag{3.23}$$

where l is the length and A the cross-section of the conductor.

In the case of alternating currents, induced magnetic fields change the current distribution and therefore the resistance. The phenomenon is known as *skin effect*. The current flowing in one conductor further induces a field in neighbouring conductors, evoking the *proximity effect*. The coupling between the resistances is expressed in terms of mutual resistances. The total loss can be expressed as

$$P = \sum_{i=1}^{N} \sum_{j=1}^{N} R_{ij} \underline{I}_i \underline{I}_j^*, \tag{3.24}$$

where N is the number of segments, R_{ij} are the partial self- and mutual resistance analogous to the inductances in Eq. (3.21).

The goal of magnetoquasistatic (MQS) analysis is to determine the per unit length resistances R' and inductances L' of the conductors. In frequency domain (FD), they can be represented by a complex valued impedance $\underline{Z}'$

$$\underline{Z}' = \frac{\underline{Z}}{l} = \frac{R + j\omega L}{l}, \tag{3.25}$$

Because all conductors are coupled via HF magnetic fields, an impedance matrix is set up to describe the system.

In the MQS analysis of the motor, usually 2D cross-sectional models of a single slot are employed to compute self- and coupling impedances of the stator conductors [16, 81]. When focusing on high frequencies, the skin depth of magnetic field in iron is very small. Therefore, the flux is assumed to be confined inside the slot (see Fig. 3.3). As a consequence, the coupling between conductors of different slots is neglected. In a massive iron core, see Fig. 3.4b, the assumption of independent slots would be correct. However, in the case of lamination, the magnetic field is actually penetrating deep into the motor core. The effect is caused by the core lamination, which promotes the eddy-current flow on the surface of each lamination sheet.

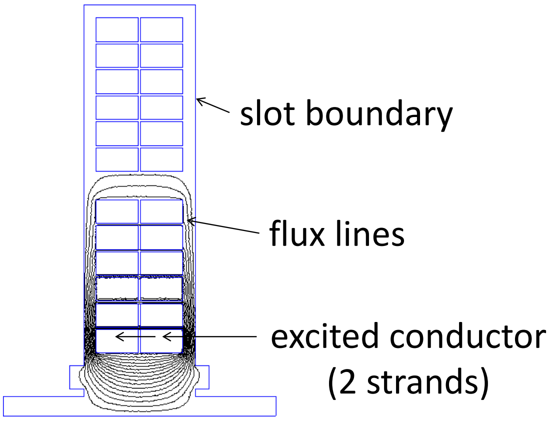

Figure 3.3.: *Magnetic flux lines of one slot simulation.*

The extension of MQS analysis from a single slot to the entire motor cross-section is an important statement of this thesis. As demonstrated by Fig. 3.4a, even at high frequencies, the flux is spreading throughout the lamination. Therefore, strong inductive coupling may occur even between distant slots. In the TL model of a motor, the lamination is considered a conductor, e.g. the reference conductor [28]. Obviously, the laminated core is not homogeneous in the axial direction. The common mode (CM) current meanders through the individual iron sheets as described in [73]. At first sight, it may seem inappropriate, to include the lamination into

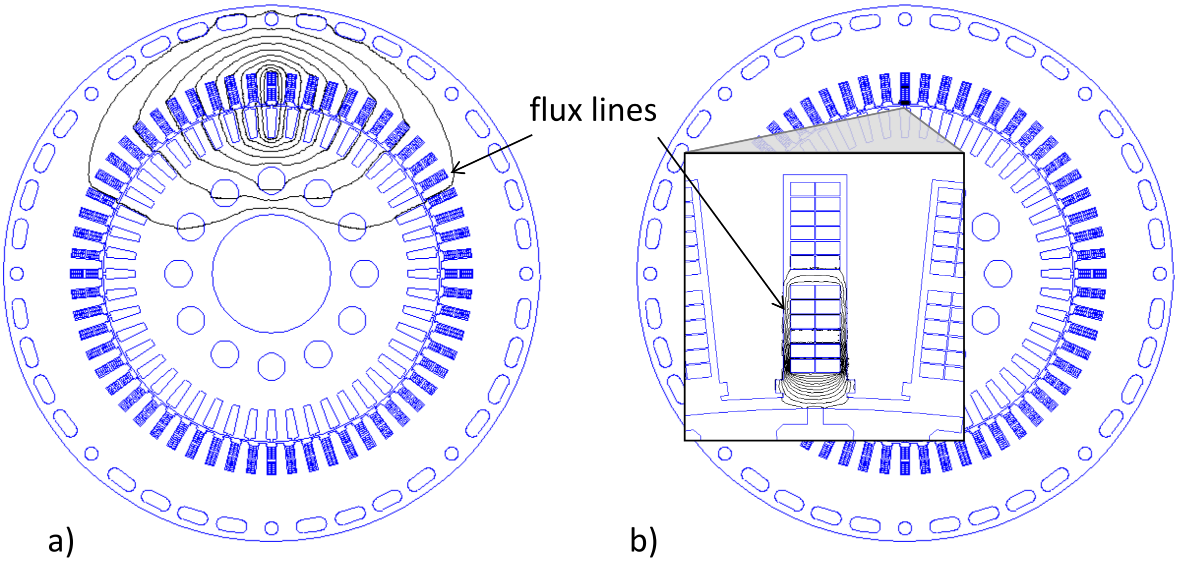

Figure 3.4.: *Magnetic flux lines in motor cross-section at 1 MHz, with a) iron laminates and b) iron as massive body.*

the transmission line (TL) model. The lamination sheets form a periodic inhomogeneity in the direction of wave propagation. However, the disturbance of the transverse electromagnetic (TEM) fields is small enough to consider the structure as quasi-TEM. A numerical investigation regarding this feature can be found in Section 5.2.

In LF motor simulations, the lamination is often treated as a homogenized material with anisotropic properties. The easiest method is to assume zero electric conductivity in the stacking direction, see for example [92]. However, this method is unsuitable to approximate eddy-current distributions (see Section 5.3). More accurate methods are those, assigning an equivalent permeability, e.g. [41], or conductivity , e.g. [99], or employing two-step methods to account for eddy currents in the second step, e.g. [15,35].

The formulation of equivalent material parameters is used in 2D simulations, while the two-step methods are designed for 3D approaches. In this thesis, a 3D analysis of a thin slice of the motor is carried out. In principle, all of these methods can be employed to determine the TL parameters.

3.3.5 Longitudinal Electric Field

In the TL model of a motor, ohmic losses in the conductors are non-negligible. Due to finite conductivity of the metals, the applied and induced currents introduce a small longitudinal electric field component

$$J_z = \kappa E_z. \tag{3.26}$$

Because of the continuity of the tangential electric field component

$$E_{\tan 1} = E_{\tan 2} \tag{3.27}$$

the longitudinal field component transfers inside the dielectric.

As a result, fields are not purely transversal and the structure is referred to as *quasi-TEM*. As long as the longitudinal field components are small, their effect on the transversal fields is negligible and E-field and H-field can be analysed separately.

A rough estimation, using motor rated values, will clarify the ratio of electric field in a good conductor versus the electric field in a good insulator. In our TL problem they are corresponding to the longitudinal field component and the transversal field component, respectively. First, we compute the electric field in a copper conductor carrying a DC current of 120 A in a cross section of 1 mm^2

$$E_{\mathrm{z}} = \frac{1}{\kappa_{\mathrm{Cu}}} \cdot \frac{120\ \mathrm{A}}{1\ \mathrm{mm}^2} \approx 2\ \mathrm{V/m}. \tag{3.28}$$

Second, we estimate the electric field in a parallel-plate capacitor, which is a good representation of the insulation gap between copper winding and stator iron. The distance of the parallel plate is assumed to be 1 mm and the potential difference is 1400 V. We obtain for our 'transversal' field component

$$E_{\mathrm{t}} = U/d = 1,400,000\ \mathrm{V/m}. \tag{3.29}$$

Since $E_{\mathrm{z}} \ll E_{\mathrm{t}}$, the longitudinal field component may be neglected, when solving the transversal field problem.

However, losses due to finite conductivity κ of the conductors are non-negligible in motor analysis. Resistance parameters are computed from the MQS field distribution as explained in the previous section. In this section, the longitudinal E-field and the resistance of a line are related by means of the Poynting vector

$$\vec{S} := \vec{E} \times \vec{H}. \tag{3.30}$$

Strictly speaking, the definition of the Poynting vector is based on the fully coupled Maxwell equations. A physical interpretation of $\vec{S}$ for decoupled fields $\vec{E}$ and $\vec{H}$ is not straightforward. However, it can be shown [47], that the loss, which is related to the longitudinal component of electric field E_z, leads to a component of the Poynting vector normal to the conductor surface

$$S_{\mathrm{n}} = E_z H_{\varphi}. \tag{3.31}$$

The Poynting vector integrated over the surface of the conductor is then associated with the power dissipation inside the lossy conductor [47]

$$\int_A S_n \mathrm{d}A = R\, I^2. \tag{3.32}$$

3.3.6 Common Mode Impedance Calculation Scheme

The common mode impedance Z_{CM} of the induction motor characterizes the system response to high-frequency (HF) common mode (CM) excitation signals. HF CM components are naturally contained in the pulse-width modulation (PWM) controlled power supply. It should be noted, however, that for measuring Z_{CM} of a machine, an impedance analyser is used [66].

The measurement device records the complex impedance between the shorted input terminals and the ground connection. Notably, the applied test signal is in the order of a few millivolts (mV). Hence, the CM current being analysed is in the order of microamperes (µA). As the machine was not excited by a three phase operating current during the measurement, potential saturation of the iron core is not considered by the Z_{CM} measurements.

In this thesis, Z_{CM} is determined without measurements. The transmission line (TL) parameters of the motor are extracted from field simulation. With the help of the winding scheme the conductors of the TL model are recombined into motor coils. End-winding parameters can be included as well (see Section 2.4).

The winding scheme is taken into account, which reduces the number of degrees of freedom (DOFs) in the system equations (3.10a - 3.10c). This is achieved by substituting each original state vector by a reduction matrix **P** multiplied with the reduced state vector, e.g.

$$\mathbf{u}(l) = \mathbf{P}_{\mathrm{ul}}\, \mathbf{u}_{\mathrm{red}}(l) \tag{3.33}$$

The subscript ‘ul’ denotes the relation to the vector $\mathbf{u}(l)$. The subscript ‘red’ means ’reduced’. The other reduction matrices would be denoted $\mathbf{P}_{il}$, $\mathbf{P}_{u0}$ and $\mathbf{P}_{i0}$. The reduction matrices contain only entries from the domain $\{-1, 0, 1\}$ and are constructed from the winding scheme. Thus, for instance, if conductors i and j are connected at the rear end of the motor ($Z = l$), this implies $u_i(l) = u_j(l)$ and $i_i(l) = -i_j(l)$. The reduction matrix in this case imposes these conditions explicitly such as the $u_j(l)$ and $i_j(l)$ are eliminated from the resulting reduced vectors. The resulting system of equations is brought into the form

$$\begin{pmatrix} \mathbf{E} + 0.5\,\mathbf{Z}\,\mathbf{Y} & -\mathbf{E} & -\mathbf{Z} & 0 \\ \mathbf{E} & -\left[\mathbf{E} + 0.5\,\mathbf{Z}\,\mathbf{Y}\right] & 0 & -\mathbf{Z} \end{pmatrix} = \begin{pmatrix} \mathbf{u}\,(0) \\ \mathbf{u}\,(l) \\ \mathbf{i}\,(0) \\ \mathbf{i}\,(l) \end{pmatrix}, \tag{3.34}$$

where **E** denotes the identity matrix of the same size as **Z** and **Y**. In the last step, the conditions at the motor terminals $u_1(0) = U_{\mathrm{CM}}$ and at the star point have to be included in the equation system. Since the star point is not grounded, this equals $i_N = 0$, where N indicates the last stator conductor, which is directly connected to the star point. When solving the final equation system, a given voltage at the motor terminals will yield a certain input current. The ratio of the two quantities yields the common mode input impedance Z_{CM}.

4 Electromagnetic Field Analysis

In this chapter, formulations of electromagnetic (EM) problems are derived as actually used in the motor analysis. Materials are assumed to be non-dispersive, linear and isotropic, unless specified otherwise. For a comprehensive review of MAXWELL*'s equations and the constitutive relation, the interested reader is referred to [50]. For further reading on finite element (FE) methods in electromagnetics, the monographs [10, 70, 74] are suggested. High-order methods are discussed in [6, 32, 100, 104], among others.*

4.1 Maxwell's Equations

Modern theory of electromagnetism traces back to James Clark Maxwell, who published his *Treatise on Electricity and Magnetism* in 1873 [74]. MAXWELL's equations are a system of first order, coupled partial differential equations which describe the classical macroscopic electromagnetic field [74]. In their differential form they read

$$\nabla \times \vec{E} = -\frac{\partial \vec{B}}{\partial t}, \tag{4.1a}$$

$$\nabla \times \vec{H} = \frac{\partial \vec{D}}{\partial t} + \vec{J}, \tag{4.1b}$$

$$\nabla \cdot \vec{D} = \varrho, \tag{4.1c}$$

$$\nabla \cdot \vec{B} = 0. \tag{4.1d}$$

The field vectors of electric field strength $\vec{E}$, magnetic flux density $\vec{B}$, magnetic field strength $\vec{H}$, electric displacement field strength $\vec{D}$, electric current density $\vec{J}$ and the charge density ϱ are functions of space $\vec{r}$ and time t.

So-called constitutive relations are complementing the MAXWELL equations in order to describe the interaction of fields with matter. Often, materials can be considered as non-dispersive, linear and isotropic. In this case, the associated constitutive relations yield

$$\vec{D}(\vec{r}, t) = \varepsilon(\vec{r})\, \vec{E}(\vec{r}, t), \tag{4.2a}$$

$$\vec{B}(\vec{r}, t) = \mu(\vec{r})\, \vec{H}(\vec{r}, t), \tag{4.2b}$$

$$\vec{J}(\vec{r}, t) = \kappa(\vec{r})\, \vec{E}(\vec{r}, t). \tag{4.2c}$$

In the case of nonlinear materials, the coefficients are dependent on field strength. For example, magnetic nonlinearity is described as $\mu = \mu\,(H)$ (see Sec. 4.5.5). In order to model anisotropy, coefficients can be formulated as tensors, e.g. the electric conductivity would read as $\underline{\underline{\kappa}}$ (see Sec. 5.3). Dispersion, i.e. frequency dependence of the constitutive parameters [103], is not considered in this thesis. The frequency dependency the relative permittivity ε_r of the winding insulation has been discussed in Sec. 3.3.3.

4.2 Electrostatic Formulation

The capacitances of the TL model are determined from the 2D electrostatic analysis in the motor cross-section. Electrostatic fields are produced by electric charges at rest, i.e. without time variation. Hence, currents and magnetic fields are excluded and only two out of the four MAXWELL equations have to be solved. Assuming electrostatic fields, they read

$$\nabla \times \vec{E} = 0, \tag{4.3a}$$

$$\nabla \cdot \vec{D} = \varrho. \tag{4.3b}$$

From Eq. (4.3a), the electric field can be written as the gradient of a scalar field, the electric scalar potential Φ:

$$\vec{E} = -\nabla\Phi. \tag{4.4}$$

With the constitutive relation

$$\vec{D} = \varepsilon\vec{E}, \tag{4.5}$$

we obtain the POISSON equation

$$\Delta\Phi = -\frac{\varrho}{\varepsilon} \tag{4.6}$$

in regions of homogeneous permittivity ε. For charge-free regions, Eq. (4.6) reduces to the LAPLACE equation

$$\Delta\Phi = 0. \tag{4.7}$$

In electrostatics, ohmic conductors form equipotentials. Fields are considered in the non-conducting region only. In our applications, DIRICHLET boundary conditions

$$\nabla\Phi \times \vec{n} = 0 \quad \text{on} \;\; \Gamma_{\mathrm{D}} \tag{4.8}$$

are assigned to each conductor $i = 1,..,N$ by applying a specific potential, e.g. $\Phi_i = 0$. Homogeneous NEUMANN boundary conditions

$$\vec{n} \cdot \nabla\Phi = 0 \quad \text{on} \;\; \Gamma_{\mathrm{N}}, \tag{4.9}$$

are assigned to the non-conducting boundaries, if existent. The normal vector is denoted as $\vec{n}$ and the NEUMANN boundary as Γ_{N}.

4.3 Stationary Current Formulation

In the magnetic field analysis of either the motor cross-section or the end-winding section, voltages are applied to the boundaries of the windings. Before computing the MQS fields, a stationary current (SC) distribution $\vec{J}_{\mathrm{SC}}(\vec{r})$ in the copper conductors is determined from the applied voltages and is used in the subsequent MQS formulation as excitation term.

In the SC field of an ohmic conductor, moving charges amount to electric current. Time variation of this current is assumed negligible and, hence, displacement currents and induced magnetic fields are not considered. Electric and magnetic fields are assumed static. The current requires electric field strength according to

$$\vec{J} = \kappa \vec{E}. \tag{4.10}$$

Similar to the ES case, the rotational electric field vanishes as in Eq. (4.3a) and the scalar potential equation

$$\nabla \cdot \kappa \nabla \Phi = 0 \tag{4.11}$$

is obtained, which reduces to the LAPLACE equation (4.7) in regions of homogeneous κ. The law of charge conservation yields the continuity equation for the SC field

$$\nabla \cdot \vec{J} = 0. \tag{4.12}$$

Practically, fixed potentials are applied to the DIRICHLET boundaries, i.e. Eq. (4.8) on Γ_D. Zero current is leaving the domain through boundaries with insulating media

$$\vec{n} \cdot \vec{J} = 0 \quad \text{on} \quad \Gamma_\mathrm{N}, \tag{4.13}$$

which yields the same homogeneous NEUMANN boundary condition as in Eq. (4.9) on Γ_N. A typical boundary condition configuration is shown in Fig. 4.1.

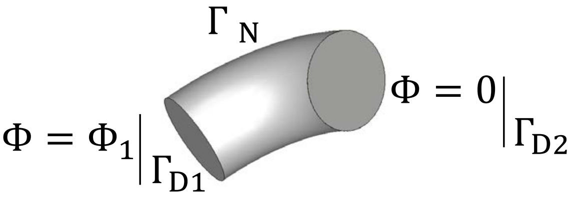

Figure 4.1.: *Ohmic conductor with boundary conditions.*

4.4 Magnetoquasistatic Formulation

In this section, the underlying equations of magnetoquasistatic (MQS) field simulations in terms of the magnetic vector potential (MVP) are derived. Starting from MAXWELL's equations in their differential form (Eqs. 4.1) and the constitutive relations (Eqs. 4.2), further adaptations to the investigated problem are made. Electromagnetic field quantities are considered in frequency domain. Under the assumption of sinusoidal time-variation and linear systems, a physical field can be represented by a complex phasor (see Eq. 3.3).

In a typical MQS field problem, displacement currents are negligible relative to conductive currents, which can be expressed in frequency domain as

$$\max_{r \in \mathbb{R}^3} \left| j\omega\varepsilon \underline{\vec{E}} \right| \ll \max_{r \in \mathbb{R}^3} \left| \kappa \underline{\vec{E}} \right|. \tag{4.14}$$

Considering copper and iron, which are good electric conductors, at a frequency of 1 MHz, we derive the following estimations

$$\frac{\omega\varepsilon_{\mathrm{Cu}}}{\kappa_{\mathrm{Cu}}} \approx \frac{2\pi\cdot 1\ \mathrm{MHz}\cdot\varepsilon_0}{58\ \mathrm{MS/m}} \approx 1\cdot 10^{-12} \ll 1, \tag{4.15a}$$

$$\frac{\omega\varepsilon_{\mathrm{Fe}}}{\kappa_{\mathrm{Fe}}} \approx \frac{2\pi\cdot 1\ \mathrm{MHz}\cdot\varepsilon_0}{2.63\ \mathrm{MS/m}} \approx 2\cdot 10^{-11} \ll 1, \tag{4.15b}$$

with $\varepsilon_0 \approx 8.854\cdot 10^{-12}$ F/m being the vacuum permittivity. We conclude, that in the considered frequency range we may apply the magnetoquasistatic assumption.

Strictly speaking, there are also longitudinal displacement currents in the surrounding insulation ($\varepsilon_r = 3$) of the conductors, which are neglected in the MQS approach. For a rough estimation of the error, we may relate the displacement current just above the the surface of a copper conductor to the conductive current on the copper surface. We obtain with continuity of tangential electric field

$$\underline{E}_{\mathrm{tan1}} = \underline{E}_{\mathrm{tan2}} \tag{4.16}$$

the following estimation

$$\frac{\omega\varepsilon_{\mathrm{iso}}}{\kappa_{\mathrm{Cu}}} \approx \frac{2\pi\cdot 1\ \mathrm{MHz}\cdot 3\cdot\varepsilon_0}{58\ \mathrm{MS/m}} \approx 3\cdot 10^{-12} \ll 1. \tag{4.17}$$

We may conclude, that the longitudinal displacement currents in the insulation will not have a noticeable effect on the global magnetic energy distribution of our problem and are, therefore, negligible in the MQS approach.

However, radial displacement currents in the non-conducting regions are certainly non-negligible, however, they are already considered by the electrostatic analysis in Sec. 4.2. According to the transmission line (TL) approach, the transverse magnetic field can be computed independently from the transverse electric field (see Sec. 3.3.4).

The transverse magnetic field is obtained from solving the MQS field problem, formulated in the plane transverse to the direction of wave propagation. Therefore, it is associated with current flow in the longitudinal direction. On the other hand, the transverse electric field is associated with (displacement) current in the radial direction.

In order to be clear with the formulation of our MQS problem, we have to adjust the assumptions. We might state, that the contribution of displacement currents to the transverse magnetic field is negligible compared to that of conductive currents.

Now, Eqs. (4.1a), (4.1b), transformed into frequency domain, read

$$\nabla\times\underline{\vec{E}} = -j\omega\underline{\vec{B}}, \tag{4.18a}$$

$$\nabla\times\underline{\vec{H}} = \underline{\vec{J}}. \tag{4.18b}$$

From Eq. (4.1d), we know that $\underline{\vec{B}}$ can be expressed in terms of the magnetic vector potential $\underline{\vec{A}}$

$$\underline{\vec{B}} = \nabla\times\underline{\vec{A}}. \tag{4.19}$$

With Eq. (4.18a) we obtain

$$\underline{\vec{E}} = -j\omega\underline{\vec{A}} - \nabla\underline{\Phi}, \tag{4.20}$$

and with Eq. (4.10) the current density

$$\underline{\vec{J}} = -j\omega\kappa\underline{\vec{A}} - \kappa\nabla\underline{\Phi}. \tag{4.21}$$

We derive the equation for the MVP within the MQS regime as

$$\nabla \times \frac{1}{\mu}\nabla \times \underline{\vec{A}} + j\omega\kappa\underline{\vec{A}} = -\kappa\nabla\underline{\Phi}, \tag{4.22}$$

The right-hand side of Eq. (4.22) is obtained from the stationary current (SC) problem by solving Eq. (4.11) in the copper conductors and computing the source current density as

$$\vec{J}_s = \vec{J}_{SC} = -\kappa\nabla\Phi_{SC}. \tag{4.23}$$

Practically, we solve the curl-curl equation as

$$\nabla \times \frac{1}{\mu}\nabla \times \underline{\vec{A}} + j\omega\kappa\underline{\vec{A}} = \vec{J}_s. \tag{4.24}$$

In this process, J_s is guaranteed to be divergence free. To ensure uniqueness of the MVP, the COULOMB gauge

$$\nabla \cdot \underline{\vec{A}} = 0. \tag{4.25}$$

is commonly used with formulations based on *nodal* elements [58].

However, we employ *edge based* elements[1]. As stated in [97], gauging is not necessary in a vector potential formulation with edge elements, in order to obtain the correct solution. Yet, solving the singular system requires consistency of the right-hand side [39,86], i.e.

$$\nabla \cdot \vec{J}_s = 0 \tag{4.26}$$

must be fulfilled exactly.

4.4.1 Boundary Conditions

The unique solution of Eq. (4.24) requires appropriate boundary conditions to be satisfied. A DIRICHLET boundary condition denotes the case, where the tangential component of the magnetic vector potential (MVP) is prescribed, while in a NEUMANN boundary condition, the tangential component of the curl of the MVP is given [98]. Employing an edge-based formulation, DIRICHLET conditions remain unchanged in the analysis and must be properly set as in the nodal case. NEUMANN conditions are naturally fulfilled in the formulation and do not need to be imposed explicitly [80].

---

[1] For details see Sec. 4.5

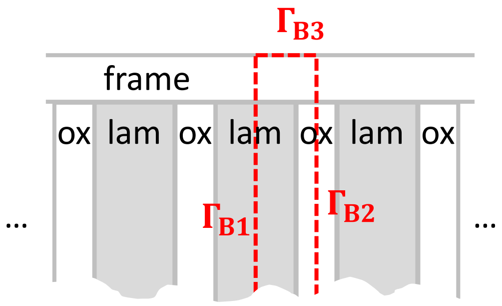

Figure 4.2.: *Side view of lamination stack with indicated periodicity.*

Taking advantage of symmetries in the finite element (FE) analysis is helpful to minimize the model size and, hence, leads to substantial alleviations of computing and storage requirements. The 3D model of an induction motor is reduced in several ways. In the longitudinal direction, the periodicity of the lamination determines the model thickness, as indicated in Fig. 4.2. Purely tangential magnetic field is assumed on the cutplanes Γ_{B1},Γ_{B2} and the outer surface of the motor frame Γ_{B3}. The subscript 'B' refers to the constraints imposed on the normal component of the magnetic flux density on the boundary

$$B_{\mathrm{n}} = 0 \quad \text{on} \quad \Gamma_{\mathrm{B}}, \tag{4.27}$$

which leads to a Dirichlet boundary condition for the magnetic vector potential:

$$\underline{\vec{A}} \times \vec{n} = 0 \quad \text{on} \quad \Gamma_{\mathrm{B}}. \tag{4.28}$$

In the circumferential direction, symmetries depend not only on the geometry of the motor cross-section but also on the excitation of the conductors. Assuming a common mode (CM) excitation, i.e. the same phase angle applies to all three stator terminals, a certain spatial periodicity can be exploited. When reducing the 360° motor cross-section to such a circular sector, the direction of the MVP on the periodic boundaries is, in general, neither parallel nor perpendicular. As a consequence, the degrees of freedom (DOFs) of corresponding boundaries have to be coupled not only in amplitude, but also in direction. The constraints on the MVP could be described in cylindrical coordinates (ϱ, φ, z) as

$$\underline{\vec{A}}(\varrho, \varphi_0, z) = \underline{\vec{A}}(\varrho, \varphi_0 + \alpha, z) \qquad on \;\; \Gamma_{\mathrm{P}}, \tag{4.29}$$

where α is the angular period and the subscript 'P' refers to 'periodic'. The implementation of periodic boundaries into the *sfem* code is discussed in Sec. 4.5.4.

4.5 The Finite Element Method

The exact solution to a differential equation is, in general, unknown for complicated geometries or boundary conditions. The finite element method seeks an approximate solution, which does not satisfy the differential equation exactly, but in an average sense over the entire domain [21].

The domain is spatially discretised by a mesh and the problem is solved locally on elements. The finite element (FE) solution is expected to converge to the exact solution of the differential equation as the mesh is refined (*h-refinement*) or the approximation order is increased (*p-refinement*). The mathematical proof of convergence of a FE solution is of fundamental importance. Details on this subject can be found, e.g., in [74]. The convergence of solutions, which are obtained with the *sfem* code, is demonstrated in Secs. 5.4 and 5.5.5.

Starting from the differential equation, the GALERKIN method of weighted residuals is used to transform the problem into its weak form. The corresponding variational formulation of the MQS problem defined by Eq. (4.24) reads

$$\int_{\Omega} \left(\frac{1}{\mu}\nabla \times \underline{\vec{A}}\right) \cdot \nabla \times \underline{\vec{A}}^{*} + \underline{\vec{A}}^{*} \cdot j\omega\kappa\, \underline{\vec{A}}\, \mathrm{d}\Omega = \int_{\Omega} \underline{\vec{A}}^{*} \cdot \vec{J}_{s}\, \mathrm{d}\Omega + \oint_{\Gamma} \underline{\vec{A}}^{*} \times \left(\frac{1}{\mu}\nabla \times \underline{\vec{A}}\right) \mathrm{d}\vec{\Gamma}, \tag{4.30}$$

where $\underline{\vec{A}}^{*}$ is a weight function [58], Ω is the domain and Γ is the domain boundary. The second term on the right hand side can be used to specify an excitation in terms of a surface current. This is equal to specifying the tangential component of the magnetic field $\underline{\vec{H}} \times \vec{n}$. However, on the boundaries of our problem, we have specified the normal component of $\underline{\vec{B}}$, which is expressed by Eq. (4.28). In consequence, the boundary integral vanishes.

In the *sfem* code, the solution of the magnetoquasistatic (MQS) problem is approximated using vector basis functions. It is well known, that the approximation of the magnetic vector potential (MVP) using *nodal elements* may lead to difficulties in the presence of material parameter jumps [17], e.g. the abrupt change of permeability at the interface iron/air. This is due to the inherent property of the procedure, imposing continuity of both the normal and the tangential components of the vector potential [9].

On the contrary, *edge-based* elements naturally fulfil the correct continuity conditions on material interfaces [14, 23, 55]. The edge-based interpolation does not force the normal component to be continuous across the interface between two different materials [80], which is in accordance with the physics of the problem.

4.5.1 Numerical Implementation

In the finite element (FE) procedure, the element matrices are, at first, constructed locally. Then, the global shape functions are obtained by systematically recombining all sets of element equations. As in most FE methods, basis functions with compact support are employed, which means, they are nonzero only on small subdomains. This leads to a sparse system matrix, which allows for fast solvers and less memory requirements.

The global equation system can be expressed in matrix notation as

$$\boldsymbol{H}\ \boldsymbol{a} = \boldsymbol{i}, \tag{4.31}$$

where the complex system matrix $\boldsymbol{H}$ combines the discrete operators corresponding to the left hand side of (4.24). The vector $\boldsymbol{a}$ holds the degrees of freedom (DOFs) of the vector potentials. The source term $\boldsymbol{i}$ is determined by a preceding simulation of the stationary current flow, when a voltage is applied to both ends of the excited conductor.

The solution of the equation system can be carried out using either a direct or an iterative solver. In our implementation the direct solver *SuperLU_DIST* from the *PETSc* library [2] was used. *PETSc* data structures and routines are designed for distributed-memory parallel machines.

In direct methods, the linear system

$$\mathbf{H}\,\mathbf{a} = \mathbf{i} \tag{4.32}$$

is usually solved by finding first the *LU* decomposition

$$\mathbf{H} = \mathbf{L}\,\mathbf{U} \tag{4.33}$$

with **L**,**U** being the lower/upper triangular matrix, respectively. Secondly, the vector **a** is found from solving

$$\mathbf{L}\,\mathbf{y} = \mathbf{i}, \tag{4.34}$$

$$\mathbf{U}\,\mathbf{a} = \mathbf{y}. \tag{4.35}$$

Direct methods are known to possess high memory requirements, since the matrices **L**,**U** are not as sparse as **H**. However, the method is beneficial in the computation scheme described in Sec. 4.5.3, since the same *LU* decomposition can be reused with several right hand side vectors.

In the *sfem* code, a consistent FE approximation for (4.24) is obtained by using high-order hierarchical shape functions for, e.g., the tetrahedral and the prismatic element (Fig. 4.3) as defined in [104]. This approach fulfils automatically the correct continuity conditions at element boundaries for the magnetic flux density, the electric field strength as well as for the induced currents in the conducting regions. Furthermore, the COULOMB gauge is satisfied implicitly, as long as the right hand side of the curl-curl equation (4.24) is divergence-free.

It is important to note, that finite elements are mapped onto reference elements (see Fig. 4.3) which allows to precompute numerical operations. For the spatial discretization, we use triangular prisms for the motor core model and a combination of prismatic and tetrahedral elements for the end-winding model. Geometrical flexibility in the motor cross-section is obtained with an unstructured triangular mesh, as known from 2D models. In the direction normal to the cross-section, the mesh is structured, which simplifies the computation.

A key feature of the *sfem* code is the parallel processing on a cluster. It allows for frequency domain (FD) magnetoquasistatic (MQS) motor computations with considerably more than 10 million DOFs. However, the mesh size was limited due to mesh generation with the *SALOME* software, which performs on a single PC.

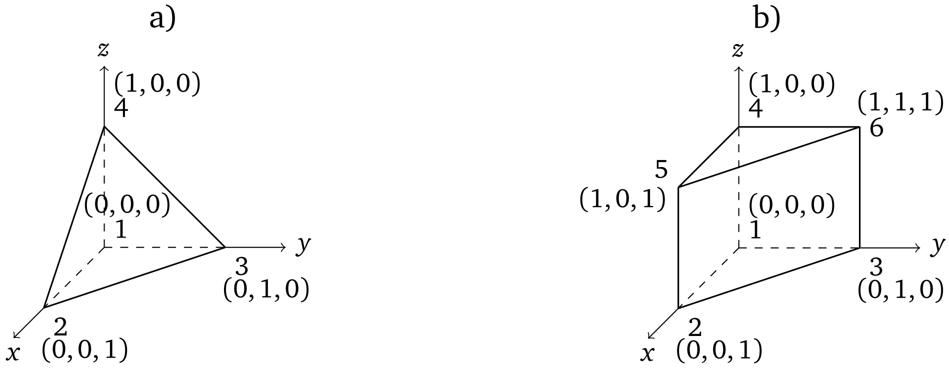

Figure 4.3.: *a) Tetrahedral and b) prismatic reference elements.*

4.5.2 Parameter Extraction

In the standard version of the *sfem* code, the equation system (4.31) is solved in order to approximate the solution of the electromagnetic (EM) field problem in terms of the magnetic vector potential (MVP). The relation between wire voltages and the source currents associated with the finite element (FE) model can be expressed as

$$\boldsymbol{i} = \boldsymbol{M}\ \boldsymbol{D}\ \boldsymbol{u}_{\mathrm{w}} \tag{4.36}$$

where

$$\boldsymbol{M} = \frac{1}{\omega}\ \mathrm{Im}\left\{\boldsymbol{H}\right\}, \tag{4.37}$$

and $\boldsymbol{D}$ is a projection matrix to couple the vector of the wire voltages $\boldsymbol{u}_{\mathrm{w}}$ to the FE system.

One conductor is excited after the other, therefore in the vector of wire voltages

$$\boldsymbol{u}_{\mathrm{w}} = \left(u_1, u_2, .., u_N\right)^T \tag{4.38}$$

only the n-th element is $u_n = 1$ V while $u_i = 0$ for all the remaining conductors. The superscript T indicates the transpose of a vector.

As was shown in [28], the impedance matrix can be computed directly from the system matrix $\boldsymbol{H}$ as:

$$\mathsf{Z} = \left(\boldsymbol{D}^T \left(\boldsymbol{M} - \mathrm{j}\omega\ \boldsymbol{M}\ \boldsymbol{H}^{-1}\boldsymbol{M}\right)\ \boldsymbol{D}\right)^{-1}. \tag{4.39}$$

Practically, this procedure is restricted to relatively small matrices. When dealing with large equation systems the explicit inversion of $\boldsymbol{H}$ in Eq. (4.39) leads to memory issues. This is related to the fact, that the inverse of a sparse matrix is generally dense [34].

A possible way to circumvent the inversion of $\boldsymbol{H}$ in Eq. (4.39) is to combine $\boldsymbol{H}^{-1}$ with the matrices $\boldsymbol{M}$ and $\boldsymbol{D}$ as

$$\boldsymbol{M}_{\mathrm{D}} = \boldsymbol{M}\ \boldsymbol{D}, \tag{4.40}$$

$$\boldsymbol{H}_{\mathrm{MD}} = \boldsymbol{H}^{-1}\ \boldsymbol{M}_{\mathrm{D}}, \tag{4.41}$$

where $\boldsymbol{H}^{-1}$ is of size $m \times m$, $\boldsymbol{M}$D and $\boldsymbol{H}_{\mathrm{MD}}$ are of size $m \times N$ each, m is the number of degrees of freedom (DOFs) in the FE system and N is the number of wires in the motor model. Next, the equation system

$$\boldsymbol{H}\ \boldsymbol{H}_{\mathrm{MD}} = \boldsymbol{M}_{\mathrm{D}} \tag{4.42}$$

is solved N times in order to determine all column vectors of $\boldsymbol{H}_{\mathrm{MD}}$. However it turns out, that, numerically, it is preferable to compute

$$\boldsymbol{i}_{\mathrm{w}} = \boldsymbol{D}^{T}\ \boldsymbol{M}\ \boldsymbol{D}\ \boldsymbol{u}_{\mathrm{w}} - \boldsymbol{D}^{T}\ \mathrm{j}\omega\ \boldsymbol{M}\ \boldsymbol{H}^{-1}\boldsymbol{M}\ \boldsymbol{D}\ \boldsymbol{u}_{\mathrm{w}}, \tag{4.43}$$

where $\boldsymbol{i}_{\mathrm{w}}$ is a vector of wire currents corresponding to the vector of wire voltages $\boldsymbol{u}_{\mathrm{w}}$ with only one element being different from zero (see Eq. 4.38).

Basically, we have returned to the standard procedure to extract the impedances of cross-sectional conductors from FE analysis, which is to impose on the n-th conductor a total current of 1 A and set all the other conductors to 0 A. The induced voltages

$$\boldsymbol{u}_{\mathrm{w}} = \mathbf{Z}\ \boldsymbol{i}_{\mathrm{w}} \tag{4.44}$$

in all conductors will be equal to the corresponding self- and mutual impedances. Alternatively, it is also possible to use voltage excitation and by employing the relation:

$$\boldsymbol{i}_{\mathrm{w}} = \mathbf{Z}^{-1}\ \boldsymbol{u}_{\mathrm{w}} \tag{4.45}$$

as was done in our 3D simulations. In both cases, this procedure has to be repeated for all $n = 1, .., N$ conductors.

A 60° section of the analysed 240 kW induction motor holds 120 stator and 8 rotor conductors. If general purpose FE software was used, this would lead to a huge computational overhead, which makes the method inconvenient. Therefore, the *sfem* code was modified for the purpose of optimized impedance extraction (see next Section).

4.5.3 Optimized Implementation

The magnetic characteristics of the multiconductor transmission line (TL) model are described in terms of a $N \times N$ impedance matrix, where N is the number of conductors. In order to determine the elements of this matrix, a similar extraction procedure has to be repeated N times. Each time, one of the conductors is excited by a voltage, while the other conductors are maintained at 0 V. Taking the symmetry of stator and rotor geometry into account, the total number of simulations can be reduced significantly, but it is still high enough to consider further optimization measures, namely in the simulation code.

The goal of the code optimization is to combine the entire extraction procedure into a single simulation cycle. Thus, common steps like loading the mesh, setup of the system matrix $\boldsymbol{H}$ and its LU decomposition have to be performed only once. A flowchart of the modified computational algorithm is shown in Fig. 4.4.

At first, the mesh and the problem definition are loaded from files. Parallel computing is used to decrease the runtime for the solution and also to increase the problem size which can be solved. When loading a larger mesh, the limited memory bandwidth[2] of the distributed computing system shows evidence of a severe bottleneck to parallel scalability. In other words, not only the actual problem size, but also the cost of data transmission adds to the overall computing time. Therefore, a huge improvement in performance is seen, when reducing unnecessary data transfer.

The next task in the flowchart in Fig. 4.4 is precomputing the periodic boundaries, which involves relatively few operations, since only certain boundary elements are affected. Nevertheless, the boundary conditions remain the same throughout the impedance matrix extraction procedure and, therefore, are saved and reused.

After another "cheap" task, namely the preparation of the coupling matrix $\boldsymbol{D}$, the system matrix $\boldsymbol{H}$ is assembled. The latter can be considered a major task, just as the LU decomposition of $\boldsymbol{H}$, which follows immediately.

Up to this point, all results are reusable. Consequently, the loop, going through the excitation of each conductor, is implemented behind. As pointed out before, it cannot be avoided to solve the linear equation system for multiple times. However, the solution is carried out very efficiently. As the matrix $\boldsymbol{H}$ is already decomposed into $\mathbf{L}$ and $\mathbf{U}$, only forward- and backward-substitution is applied to solve Eqs. (4.34 - 4.35), respectively.

In the course of looping over N, the admittance matrix $\mathbf{Y}$ is assembled column by column. The desired impedance matrix $\mathbf{Z}$ is finally derived by direct inversion of $\mathbf{Y}$. In this case, the inversion is feasible, since $\mathbf{Y}$ is only of size $N \times N$, where N is the number of conductors.

Compared to the unmodified code a speed-up factor of about 100 could be obtained. The desired impedance matrix extraction at 7 frequency points for a motor model containing 9.6 million degrees of freedom (DOFs) could be achieved in less than 4 hours on a cluster using 60 nodes.

---

[2] Rate at which data can be read from or stored into memory by a processor.

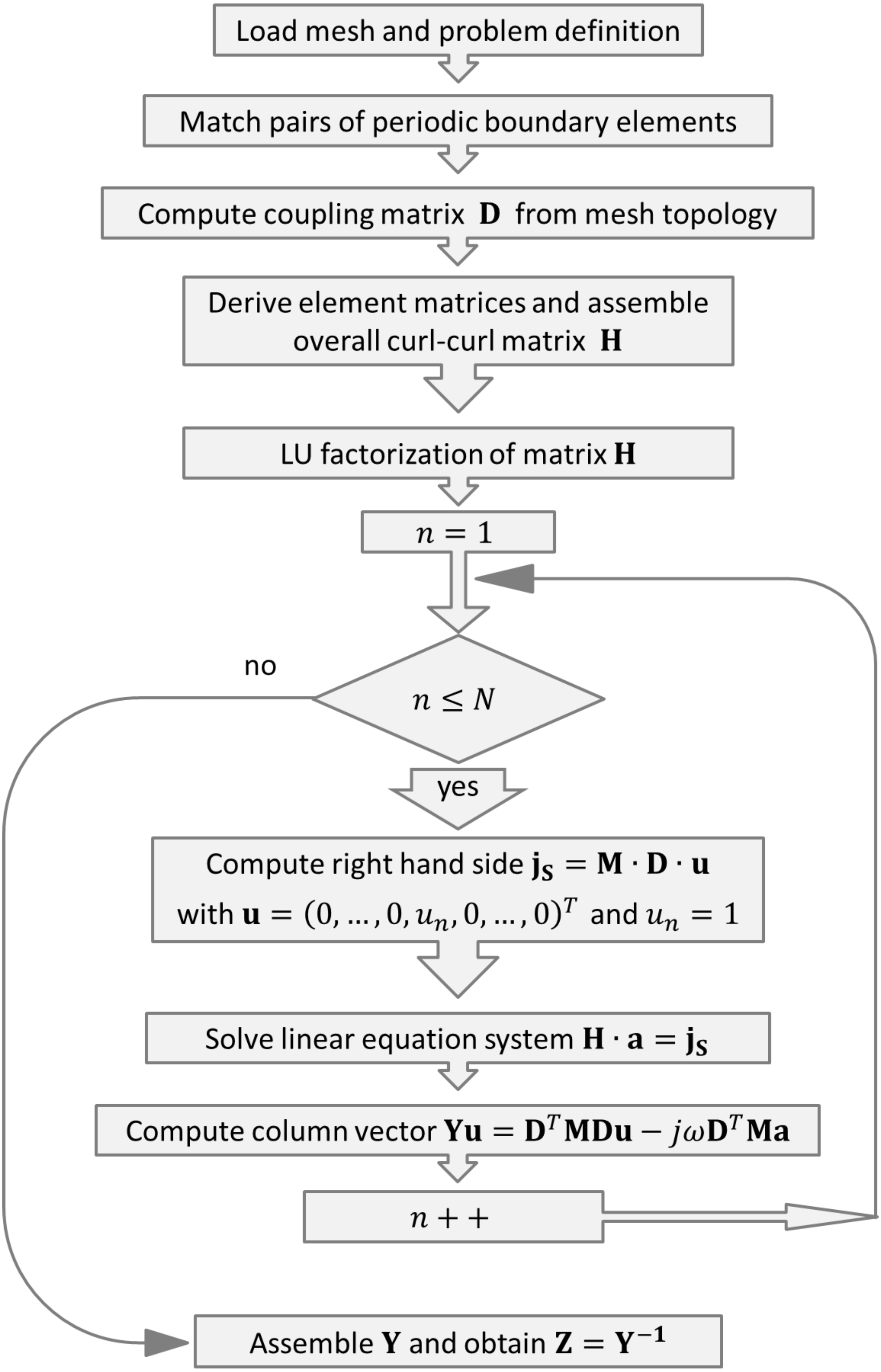

Figure 4.4.: *Flowchart of the parameter extraction procedure.*

4.5.4 Periodic Boundaries

An induction motor is usually equipped with several identical poles. The three-phase current generates an anti-symmetric pattern from pole to pole. However, when looking at common mode (CM) excitation, the symmetries are different. The CM voltage is applied simultaneously to all three phase terminals. When the rotor conductors are modelled as well, a common symmetry of stator and rotor has to be found. In the case of the 240 kW induction motor, a periodicity of 60° can be used (see Sec. 5.5).

As opposed to the quite restrictive conditions of purely normal or tangential fields, periodic boundary conditions (PBCs) are more versatile. Fields may be of arbitrary amplitude and direction as long as the corresponding boundaries show the same distribution. In the problem definition, the PBCs are assigned to pairs of outer surfaces of identical shape. Consequently, the degrees of freedom (DOFs) at each pair of the periodic surfaces are coupled in the simulation process.

PBCs are offered in many commercially available finite element (FE) software packages. However, to take advantage of the other unique features of the *sfem* code, PBCs were incorporated into the C++ code by the author of the thesis. In order to verify the algorithm, a 60° model with PBCs was compared to the corresponding 360° model without PBCs (see Section 5.1).

The magnetoquasistatic (MQS) module of the *sfem* code employs a magnetic vector potential (MVP) formulation based on vector elements. The PBCs have been implemented for edge-based functions. In contrast to nodal definitions, the DOFs of tangentially-continuous edge-based methods are vectors and, therefore, the definition of PBCs is different [80].

The exploitation of geometrical symmetry in 3D eddy-current formulations employing edge-variables was thoroughly investigated in [18]. On the other hand, Nakata et al. have pointed out some difficulties with nodal formulations, which arise from the fact that the periodic phenomena are defined by the flux and current distributions, while the PBCs for the MVP cannot be directly obtained from $\vec{B}$ and $\vec{J}$ at one point [76]. However, this is no issue when employing edge-elements and, once more, confirms their usefulness in our implementation.

In order to facilitate the implementation of PBCs, as well as the actual solution of the curl-curl problem, a *periodic mesh* should be used. A periodic mesh is a mesh structured in a way, that each surface element on one periodic boundary has a corresponding element on the associated periodic boundary. In this case, the corresponding DOFs on both periodic surfaces can be set equal, circumventing any interpolation or additional constraints. Due to the vectorial nature of edge elements, directions, moduli and signs, assigned to each symmetrical pair of degrees of freedom, must be considered. According to [80], the conditions can be written as

1) directions of DOFs on the periodic planes are rotationally symmetric,
2) moduli of DOFs along symmetrical edges are the same as $|\vec{A}_i| = |\vec{A}'_i|$, where $|\vec{A}_i|, |\vec{A}'_i|$ are circulations of the MVP along symmetrical pairs of edges, and
3) signs are assigned to each symmetrical pair of DOFs such as identical directions are obtained.

The implemented method is described in the following. For the reasons given above, *periodic meshes* are required for the use of PBCs in the *sfem* code. The periodic mesh with a period angle of 60° is easily obtained by first creating a 30° mesh and, following this, mirroring the mesh at a lateral face. Obviously, this technique can be employed only, because the considered geometry provides the necessary symmetry within the 60° piece. However, symmetries of this type are found in most motor geometries. Mirroring the mesh also provides the advantage, that the geometrical direction of one edge, rotated by the period angle α, automatically coincides with the direction of the corresponding edge. Yet, in order to avoid confusion, directions of all periodic edges are reviewed in the simulation code.

When the simulation is first started, the mesh topology and configuration data are loaded from files. Subsequently, the introduction of the PBCs is prepared: Based on the mesh topology, all edges, associated with PBCs are filtered and their locations are recorded together with their global indices. Then, pairs of edges are matched by evaluating their coordinates and the matching edge indices are stored in a table. During global assembly of the curl-curl system matrix, this table is recalled. The curl-curl system matrix $\boldsymbol{H}$ (see Eq. 4.31) is set up by looping over all combinations of edges i, j.

Different cases may occur:

1) Both edges i, j have PBCs, but they are not a pair,
2) they are a pair,
3) either one of the edges has a periodic condition,
4) none of the edges has a periodic condition.

According to each case, the value of the local curl-curl operator is

1) split 0.25/0.25/0.25/0.25 to the entries H_{ij}, H_{il}, H_{kj} and H_{kl}, where k and l are the periodic partner edges of i and j,
2) split 0.5/0.5 to the entries H_{ij} and H_{kl},
3) split 0.5/0.5 to the entries H_{ij} and H_{kj}, if i has the PBC or split 0.5/0.5 to the entries H_{ij} and H_{il}, if j has the PBC,
4) assigned fully to H_{ij}.

4.5.5 Nonlinear Formulation

The nonlinear properties of iron, as well as modelling methods in time domain, are reviewed in Sections 2.2 and 2.2.1. In the present section, a method to account for nonlinear behaviour in frequency domain (FD) simulations is explored. The method is designed to incorporate the linear methods described previously, however, with a slight modification in the simulation code.

So far in this chapter, the eddy currents inside the lamination are analysed under the assumption of a constant and uniformly distributed permeability. However, when taking the nonlinear B-H curve of iron into account, permeability distribution and magnetic field solution become interdependent. A nonlinear problem is created, which is generally contradictory to the principles of superposition in the TL approach. Therefore, nonlinear analysis must be performed outside of the TL formulation, i.e. through consideration of the actual 3-phase excitation of the IM.

The numerical solution of the nonlinear problem has to be approached iteratively, where the permeability is updated in each step. Thus, for instance, sinusoidal excitation applied to a nonlinear system leads to the formation of harmonics in the output. Hence, the fields are not sinusoidal anymore, but still periodic. Analysis of the problem in FD requires consideration of the involved frequency components [58]. However, single-harmonic approaches were explored by several authors. The concept of equivalent permeability was employed to account for hysteresis and eddy currents [79]. The approach was extended to consider the effect of saturation while neglecting higher harmonics [36, 53].

In order to account for harmonics, several frequencies should be considered simultaneously. The approach is referred to as *harmonic balance (HB)* method and can be employed to find the steady-state solution of nonlinear problems. HB is commonly used in circuit analysis [64], but is also applied to field problems [102].

In the method, the time periodic variables are approximated by truncated Fourier series

$$y(\vec{r},t) \approx y_N(\vec{r},t) = \sum_{k=0}^{N} \left[y_k^c(\vec{r})\, cos(k\omega t) + y_k^s(\vec{r})\, sin(k\omega t) \right], \tag{4.46}$$

where N is the number of chosen harmonics and $y_k^c(\vec{r})$, $y_k^s(\vec{r})$ are Fourier coefficients to be discretised in space. The field problem is formulated in terms of a finite number of FD equations, one for each of the chosen harmonics. The equations are coupled through the field-dependent magnetic permeability.

After discretization of the domain into finite elements and application of GALERKIN's method, the size of the equation system becomes a multiple of the standard FE system, wherein only a single frequency is considered. Despite the proposition of efficient algorithms, e.g. [7, 30, 42], HB methods would exceed the computational capability of the 3D motor model.

In the method presented in this thesis, feedback from the HF components to the LF calculation is omitted. It is assumed, that the permeability distribution in the iron lamination is entirely determined by the fundamental component of the excitation. The approximation is justified by the fact, that in the spectra of all PWM schemes, the fundamental has the greatest amplitude. A similar method, yet limited to 2D analysis, was proposed in [84] and was found to show reasonable agreement with measurements.

5 Numerical Results

In this chapter, the numerical results of this thesis are presented. Starting with small verification and validation examples, we then apply the methods, described in the previous chapters, to an existing 240 kW induction machine. The distinction between verification and validation often refers to the distinction between numerical and conceptual modelling. On that account, code verification aims at a convincing demonstration, that the equations are solved correctly [57]. On the other hand, proper modelling of the physical problem is subject to the validation process. A comprehensive treatise on the definitions of verification and validation in scientific computing is found in [78].

5.1 Verification of the 3D Finite Element Code

The *sfem* code, used in this thesis, is continuously improved and extended, by Dr. Gjonaj himself as well as by the author of this thesis. Hence, in order to assure correct functionality of the code, each analysis was preceded by verification tests using analytical calculations as well as standard 2D and 3D FE software as a reference. Some examples are presented in this section.

Example 1 - Comparison to the analytical solution

The first verification example is a circular copper conductor in vacuum. In order to form a closed loop, the current is assumed to return via the boundary which encloses the domain at radius $r_5 = 7.1$ mm. Given a conductivity of copper $\kappa_{Cu} = 58$ MS/m, permeability of vacuum $\mu_0 = 4\pi \cdot 10^{-7}$ H/m , conductor length $l = 3.75$ mm and radius of conductor $r_1 = 2$ mm, the DC resistance yields

$$R = \frac{l}{\kappa_{\mathrm{Cu}} \pi r_1^2} = 5.14\ \mu\Omega \tag{5.1}$$

and DC inductance

$$L = \frac{\mu_0 l}{8\pi} + \frac{\mu_0 l}{2\pi} \ln\left(\frac{r_5}{r_1}\right) = 1.14\ \mathrm{nH} \tag{5.2}$$

Derivation of the analytical formulae is given in the Appendix A.4. Numerical calculations with the *sfem* code yield essentially the same results within specified numerical tolerances. The relative error between analytical and numerical solution is found to be $< 0.1\%$ using a fine spatial discretization.

Example 2 - Lamination

The next verification example uses the same copper conductor as above, but now placed inside of a laminated iron stack. Inner radius of the iron core is $r_2 = 2.1$ mm, outer radius $r_3 = 5.1$ mm.

The stack is tightly enclosed by a nonmagnetic iron frame with outer radius $r_4 = 6.1$ mm. Some free space is added terminating at the domain boundary at $r_5 = 7.1$ mm. The iron stack consists of 5 laminations, each of thickness $d_{\text{lam}} = 0.65$ mm, the insulation layer between the sheets is $d_{\text{ox}} = 0.1$ mm thick (see Fig. 5.1).

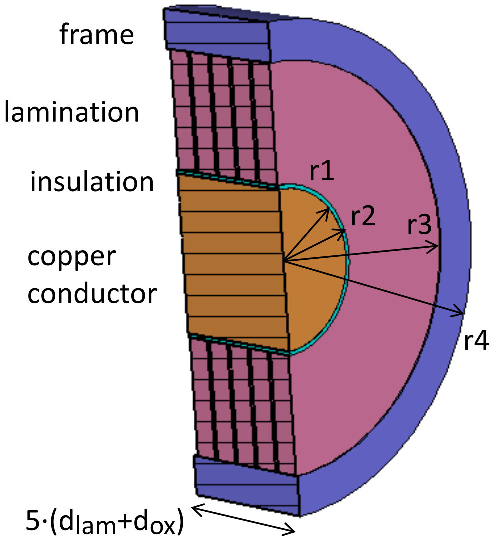

Figure 5.1.: *One conductor model with lamination, view: cut-plane. Image created with CST EM Studio®*

This example was computed with the *sfem* code and using CST EM Studio® as a reference. A voltage of 1 V was applied to the copper conductor and current $\underline{I}$ was computed. Frequency ranges from 1 Hz to 1 MHz. Resistance R and inductance L of the system are computed from the total electric loss P_{el} and the total magnetic energy W_{mag}, respectively:

$$R = \frac{P_{\text{el}}}{|\underline{I}|^2} \tag{5.3}$$

$$L = \frac{2\,W_{\text{mag}}}{|\underline{I}|^2} \tag{5.4}$$

Results are compared in Fig. 5.2. The agreement seems to confirm once again correctness of the *sfem* code.

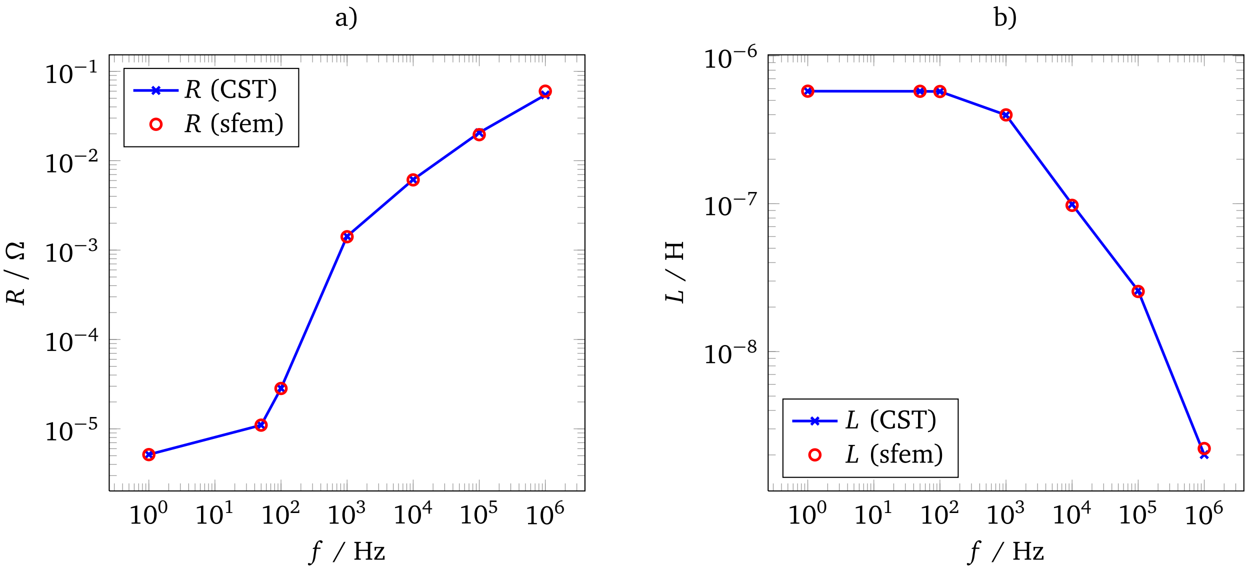

Figure 5.2.: *a) Resistance and b) inductance of one-conductor model with lamination.*

Example 3 - Periodic boundaries

In the analysis of the 240 kW motor model, a 60° rotational symmetry of the fields was exploited. Therefore, periodic boundary conditions have been implemented in the *sfem* code by the author of the thesis. Correctness of the code implementation is demonstrated in the following example.

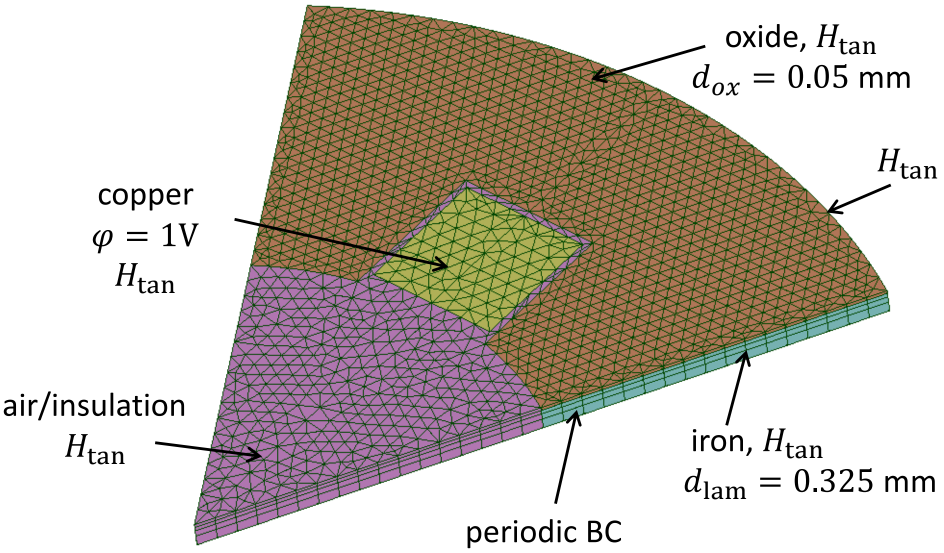

Figure 5.3.: *Mesh of* 60° *model, periodic boundary conditions are applied. Mesh created with SALOME software.*

The tested structure is composed of a copper conductor, insulation and lamination with an oxide layer. In the magnetic computation, two kinds of boundary conditions apply, namely tangential magnetic fields H_{tan} and periodic fields (see Fig. 5.3). The copper conductor is excited by 1 V sinus signal at frequency $f = 10$ kHz. A total electric loss of $P = 312.0$ W and total magnetic energy of $W = 2.409$ mJ are computed with the *sfem* code. This corresponds exactly to $1/6$ of the quantities computed for the corresponding 360° model without periodic boundaries.

5.2 Validation of the Transmission Line Approach

The transmission line (TL) approach is based on the separation of electric and magnetic field solutions. On the other hand, full-wave simulations consider both fields simultaneously and will be used to validate the TL approach. As an example one copper conductor placed in an iron lamination stack (the same model as in Example 2 in Section 5.1) is examined. The reference solution is computed with the full-wave solver of CST EM Studio® . The TL parameters are computed from the analytical electrostatic (ES) solution and from 3D magnetoquasistatic (MQS) simulations using *CST* software.

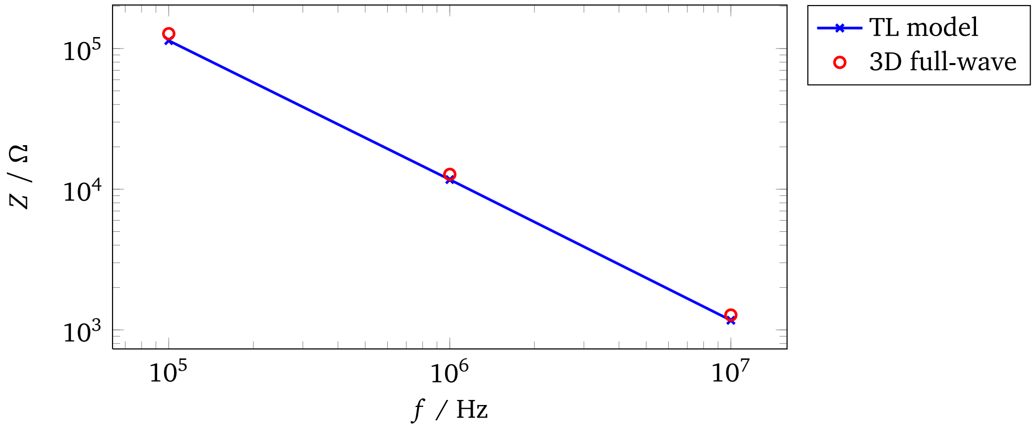

Figure 5.4.: *CM impedance of one-conductor model with lamination, TL approach and full-wave simulation.*

In the model, the end of the copper conductor is not connected to the domain boundary. This corresponds to an open-ended TL. At sufficiently low frequencies the electric field energy dominates, and the system reacts like a capacitor. In other words, the amplitude of Z_{CM} decreases with increasing frequencies, as can be observed in Fig. 5.4. The two curves agree quite well.

However a deviation of about 10% is observed. In fact, the full-wave simulations with CST EM Studio® are influenced by an undesired edge effect due to the excitation via current path. This leads to an additional 10% of electric field energy outside the actual model and, therefore, lowers the overall capacitive impact just like an additional series capacitance. Subtracting out the edge effect, it can be concluded, that the comparison of input impedance seems to confirm the TL approach.

Remark: In typical motor analysis, there will be the first resonance point around 100 kHz. At this frequency, the dominating capacitive and inductive effects cancel out and the CM input impedance of the motor is reaching a minimum. However, this cannot be observed in the one-conductor model, because the ratio of inductance to stray capacitance is much smaller than in the actual motor. This is due to the fact, that in a motor, the coils have multiple turns which increase the inductance.

5.3 Accuracy of Homogenization Techniques

In a 3D FE simulation of an entire induction motor, the individual laminations cannot be resolved by the mesh. The discretization of the small skin depth at higher frequencies and the thin oxide layer separating the iron sheets would lead to an enormous number of mesh cells, which by far exceeds today's computing capacities. Therefore, several homogenization techniques have been proposed in the literature. To investigate two of them, the simple geometry shown in Fig. 5.5 is considered.

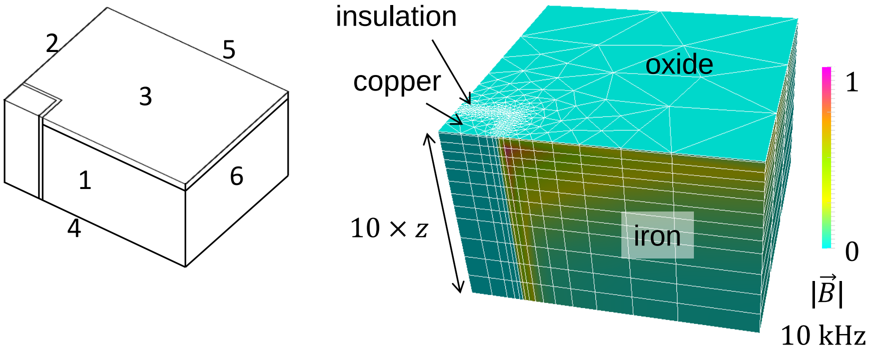

Figure 5.5.: *B-field of one-conductor model at 10 kHz, $H_{tan} = 0$ is set to planes 1-2, $E_{tan} = 0$ is set to planes 3-6*

It comprises a rectangular piece of copper conductor, which is electrically insulated from the surrounding iron sheet. The lamination sheet is covered by a thin oxide layer. The outer dimensions of the test geometry are $5 \times 5 \times 0.35\ \text{mm}^3$. Owing to the symmetry of the model only 1/8 of the geometry needs to be considered in the simulations. The 3D reference solution is computed with the *sfem* code.

Technique 1 - Zero conductivity normal to the laminations

A popular homogenization technique which is often used in 3D motor simulations [92] consists in assuming an anisotropic conductivity tensor in a bulk iron material with zero conductivity in the direction perpendicular to the lamination as

$$\begin{bmatrix} \kappa_x & 0 & 0 \\ 0 & \kappa_y & 0 \\ 0 & 0 & \kappa_z \end{bmatrix} = \begin{bmatrix} F\,\kappa_{\text{Fe}} & 0 & 0 \\ 0 & F\,\kappa_{\text{Fe}} & 0 \\ 0 & 0 & 0 \end{bmatrix} \tag{5.5}$$

where F is the stacking factor and κ_{Fe} is the conductivity of the iron sheet. The approach seems to be reasonable in the LF range, when eddy-current effects on the field distribution are negligible. The numerical tests (see green line in Fig. 5.6) reveal an error of less than 4% when the technique is applied at 50 Hz. This certainly justifies the application of this model in a number of commercial simulation packages. Nevertheless, at high frequencies when the skin effect becomes significant in the laminations, this simple homogenization technique is not valid any more.

It should be mentioned, that, based on anisotropic material models, a number of more sophisticated homogenization methods have been shown to give accurate results for test problems even at higher frequencies [35, 40]. These methods often allow for arbitrary flux orientation[1], which is important in the end-winding region. When interested in the middle part of the motor,

---

[1] Fluxes may be both parallel and perpendicular to the lamination.

however, it is possible to take advantage of the longitudinal periodicity in the lamination stack, which is exploited in the following approach.

Technique 2 - Equivalent permeability approach

The analytical solution of eddy-current distribution in an infinitely large plate (Eq. 2.9) can be employed to account for the laminated iron core. In our test, a 2D model is set up at exactly the same dimensions in the x-y plane, whereas the lamination in the z-direction is considered using the equivalent permeability approach (Eq. 2.10).

Simulations are carried out in the frequency range 10 Hz-1 MHz. From the field results, the overall electric losses P_{el} and the stored magnetic energy W_{mag} are calculated (see blue line in Fig. 5.6). In contrast to *technique 1*, 2D simulations using the effective iron permeability agree very well with the reference in the low-and medium frequency range. At 1 kHz the simulations showed a difference of less than 7% for the electric losses and 1% for the magnetic energy. However, as the frequency increases the deviations become larger. The discrepancy between 2D and 3D results at 1 MHz amounts to 9% for P_{el} and 18% for W_{mag}, respectively.

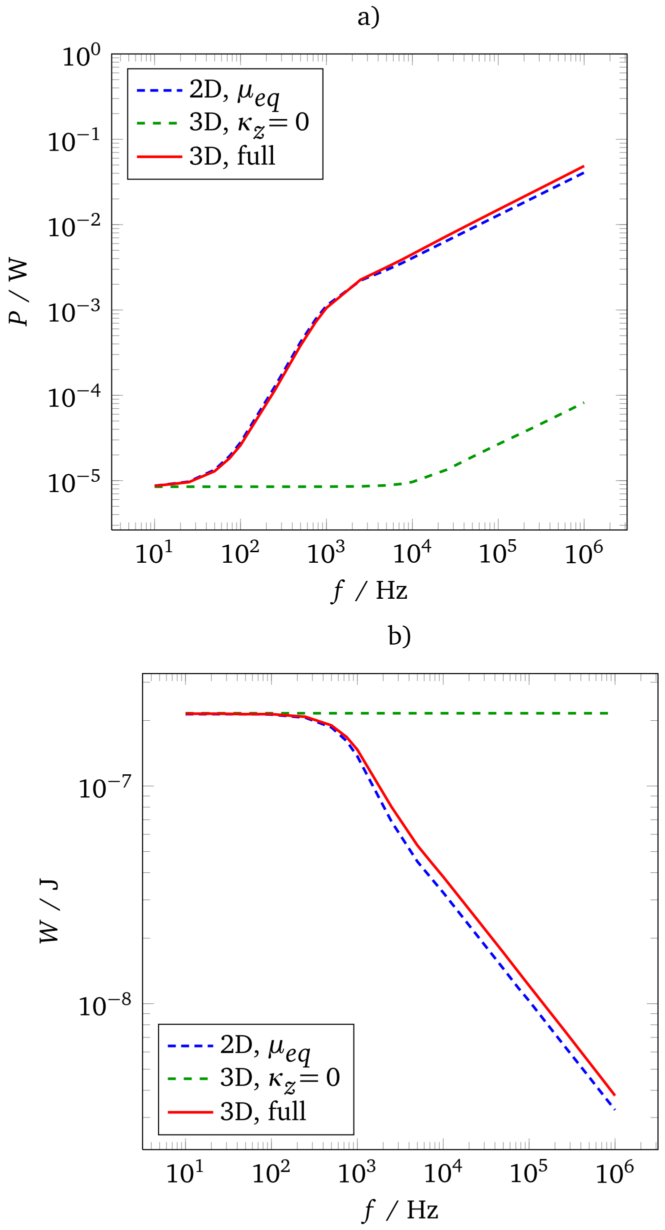

Figure 5.6.: *Comparison of a) electric loss and b) magnetic energy in one-conductor model using different approaches (2D, 3D homogenized and 3D full model).*

5.4 Efficiency of High-Order Methods

In the following, the numerical approach used to obtain reference solutions by full-scale 3D eddy-current simulations is described. Numerical convergence was established by applying a set of meshes with different resolutions as well as different approximation orders.

Figure 5.7 shows, in particular, that employing high-order basis functions improves accuracy significantly even for coarse meshes. This allows for reliable results, especially at higher frequencies, when the skin depth is difficult to resolve by the mesh. Full numerical convergence is obtained in the single conductor test case by using a coarse mesh (with only 7,000 elements) and either quadratic or cubic finite element (FE) basis functions. Also in the figure, the devi-

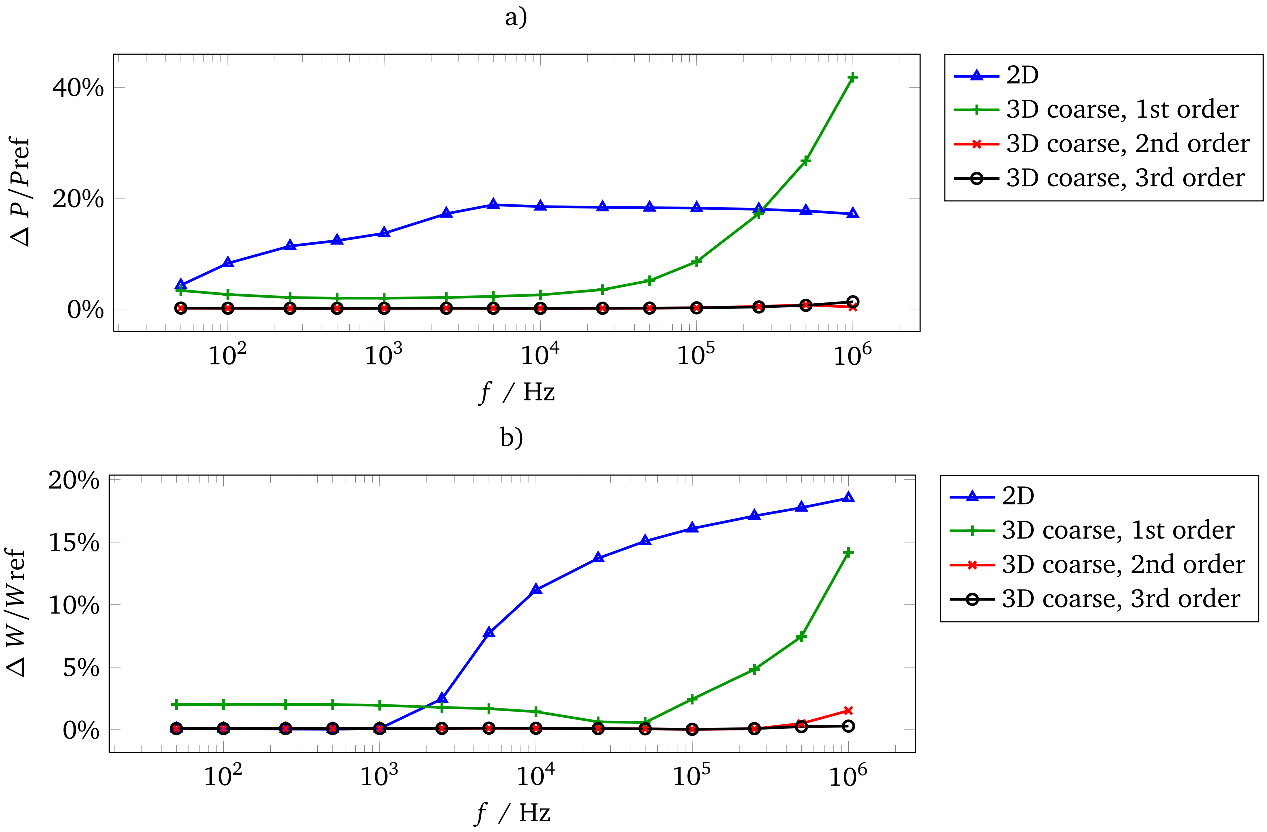

Figure 5.7.: *Percentage error of a) electric losses, b) magnetic energy of one-conductor model. Reference is a 3D model with fine mesh (700,000 elements).*

ation between 2D and 3D simulations is shown. They occur because of the application of the equivalent permeability model (Eq. 2.10) in the 2D simulations.

Table 5.1 summarises the simulation parameters used. As seen in the table, apart from providing more accurate results, the use of high-order FE approximations may also reduce simulation time. A second-order computation on a coarse mesh is four times faster than a fine mesh first-order simulation for the same accuracy.

The tuning of simulation parameters for optimal efficiency, however, depends also on the number of parallel computing nodes involved in the simulation. A third-order computation on a coarse mesh using 60 nodes appears again less efficient than the low-order simulations. This is a result of the deterioration of the parallel speed-up in the numerical solution of discrete FE equations for a large number of parallel computing processors.

Mesh	No. of mesh elements	Order of basis functions	CPU time (min)	No. of parallel computing nodes
2D	5,000	1	2	1
3D fine	700,000	1	128	30
3D coarse	7,000	1	3	10
3D coarse	7,000	2	28	24
3D coarse	7,000	3	306	60

Table 5.1.: *Discretisation parameters used in the simulations and corresponding CPU times for a full frequency sweep in the range 10 Hz - 1 MHz.*

5.5 Numerical Analysis of a 240 kW Induction Motor

The modelling methods developed in this thesis are demonstrated on the example of a real 240 kW induction machine (Fig. 5.8), which is available at the *Institute of Electrical Energy Conversion* of the *Technische Universität Darmstadt*. Measurements of the common mode input impedance are by courtesy of colleagues from the aforementioned institute. The motor is well documented in data sheets, however, not all desired information is available. The permittivity of the stator coil insulation remains unknown as well as the actual stacking factor of the iron core. The latter is necessary to define the thickness of the oxide layer in the magnetoquasistatic model of half a lamination sheet. In the model, these values were defined according to suitable literature sources.

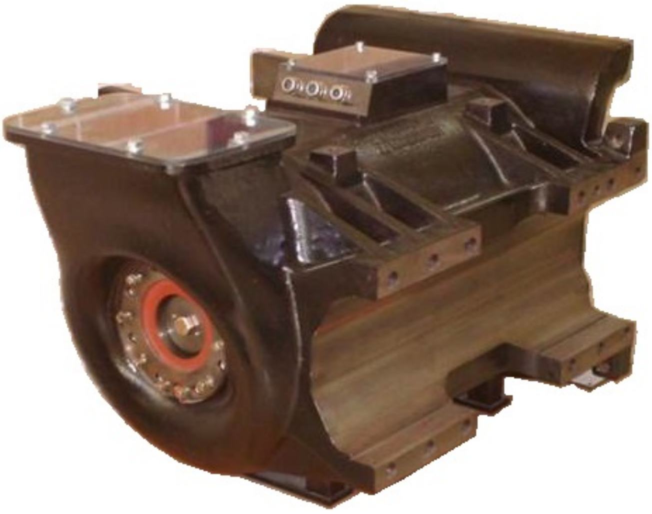

Figure 5.8.: *Siemens 240 kW induction motor*

The motor cross-section (Fig. 5.9) was reconstructed from the geometrical data. The motor has 4 poles, 60 stator slots and 48 rotor slots. The stator winding divides into three phases and two parallel branches per phase. There are two layers in each slot with 6 conductor per layer and two strands per conductor. Additional data are given in Appendix A.6.1.

The winding of an induction machine (IM) can be constructed in different ways. Machines with voltages below 1000 V usualy have random wound coils, while machines for higher voltages employ form-wound coils. Stator coils are usually made from copper, rotor bars are made from either copper or aluminium. Our 240 kW IM possesses form wound coils and copper rotor bars.

In order to increase the effective cross-section, the stator conductors are often stranded. The parallel strands form one half-turn and several of them are connected in series by the end-winding to form coils. Coils may be connected in series or in parallel. The stator winding must be well insulated against the grounded stator core and other machine parts. The rotor winding of a squirrel-cage IM usually has no explicit electrical insulation on the rotor conductors, since the induced voltages are very low [95].

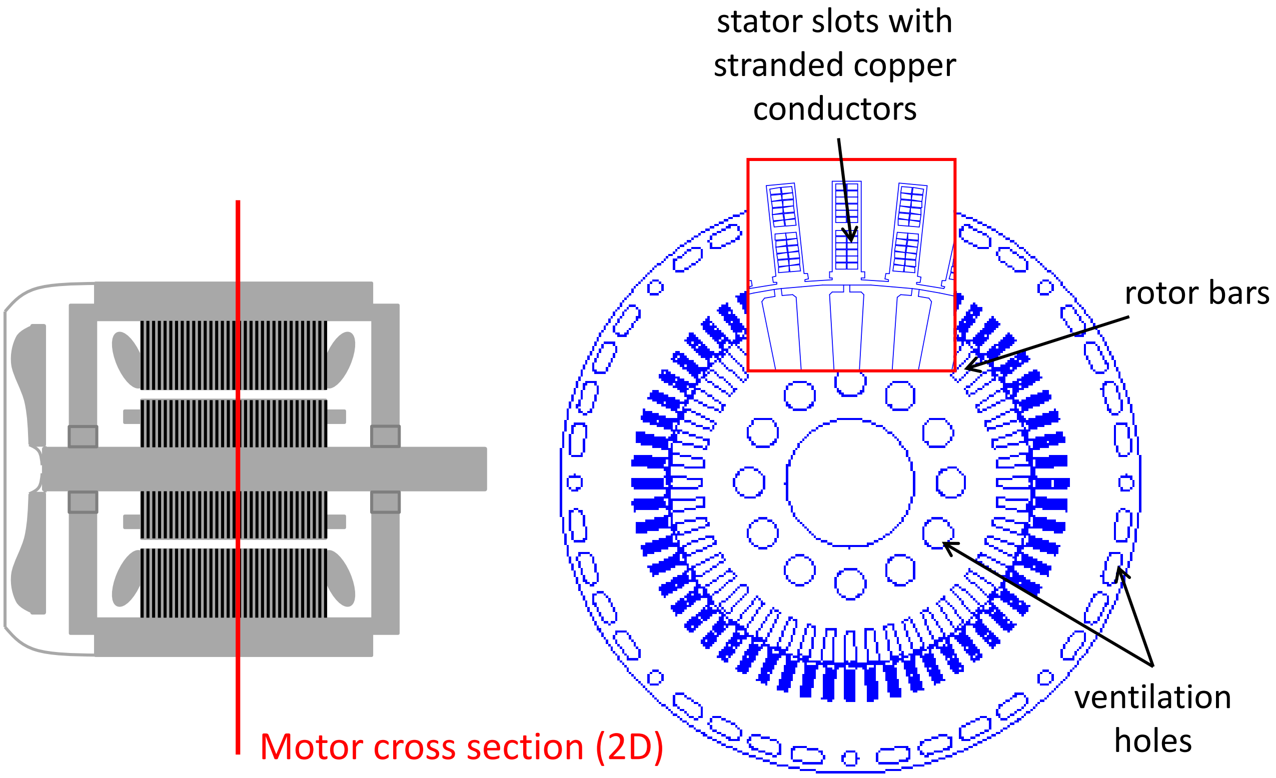

Figure 5.9.: *Cross-section of 240 kW induction motor. Right hand side image created with FEMM software.*

5.5.1 Electrostatic Analysis

The electrostatic (ES) field solution is used to extract the capacitance matrix of the conductors in the transmission line (TL) model. Accurate determination of stray capacitances is crucial to the prediction of the common mode (CM) response of the motor. As a matter of fact, the numerical solution of the corresponding 2D electrostatic (ES) field problem is straightforward. The true challenge of proper capacitance estimation lies in the correct representation of geometry and insulating material properties.

Stray capacitances are formed by electrically insulated conductors, which are in close proximity to each other. Small tolerances in the geometry may significantly affect the calculation. Therefore, the manufacturing process has to be taken into account. This is especially true for low voltage machines with random wound coils, where the position of conductors inside the slots is unknown and changes within the winding. Fortunately, our 240 kW machine is equipped with form wound coils.

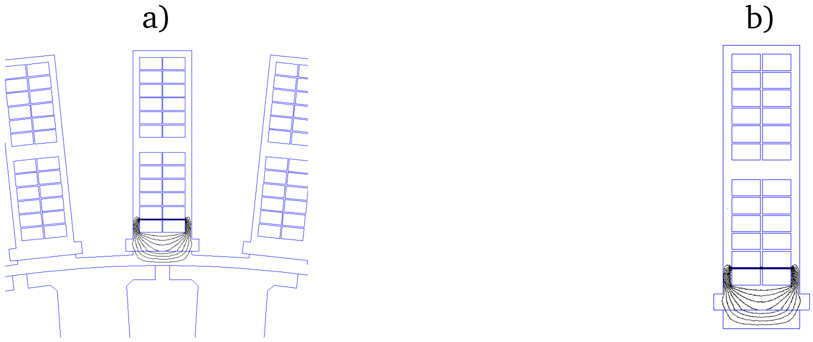

Figure 5.10.: *Electrostatic potential field plot for partial capacitance computation considering a) the entire motor cross section and b) only one slot.*

Stray capacitances are often distinguished into turn-to-turn, turn-to-stator frame and several air gap capacitances. In the 2D ES field simulation of the entire motor cross-section, such classification in not necessary. However, it can be easily seen from the distribution of the electric potential (Fig. 5.10a), that electrostatic coupling between adjacent slots and across the airgap is negligible compared to the situation found within one slot. This leads to the conclusion, that a single slot simulation is sufficient for accurate capacitance extraction (Fig. 5.10b).

In our ES computations it is assumed that the entire slot is homogeneously filled with an insulating material with a relative permittivity of $\varepsilon_{\mathrm{r}} = 3$. In reality, insulation materials may be layered and the winding does not completely fill the slot cross-section, which leaves some regions filled simply with air at $\varepsilon_{\mathrm{r}} = 1$. For most stator winding insulation materials, the dielectric constant is about 4 [95]. Practically, a reduction factor < 1 is often employed in order to account for inhomogeneous permittivity distribution.

The ES problem is modelled and solved with *FEMM*. The elements of the capacitance matrix of the winding are extracted subsequently by applying 1 V to one of the conductors and 0 V to all the rest. In the FE simulation the electric scalar potential Φ is computed inside the non-conducting domain. We obtain the electric field according to Eq. 4.4 and the unknown charges by integrating along the contour of each conductor as

$$Q_{ij} = \int_A \varepsilon \vec{E}_j \cdot \mathrm{d}\vec{A}, \tag{5.6}$$

where Q_{ij} is the electric charge on conductor i, when a voltage is applied only to conductor j. A is a closed surface around conductor i, which reduces to a contour in the 2D problem. When the voltages U_{ij} and the charges Q_{ij} are known, the capacitance matrix is easily computed from Eq. 5.6.

The boundary of the problem region is defined by the inner contour of the stator iron core. As the stator core is electrically connected to the grounded stator frame, the potential is set to zero. The rotor of the machine is not grounded, which implies that the rotor should be modelled as an additional conductor. Clearly, in the single slot simulation (Fig. 5.10b), the rotor is not considered. However, as the stator-to-rotor capacitances are relatively small, their influence on the TL model is negligible. Some of the capacitance coefficients yield, for instance,

$$C'_{11} = 1.2\ \mathrm{nF/m},$$
$$C'_{12} = -1.0\ \mathrm{nF/m}\ \text{and}$$
$$C'_{1\mathrm{r}} = -0.01\ \mathrm{nF/m},$$

where the indices 1,2,r are associated with the stator conductors 1,2 and the rotor, respectively.

Remark: Stator winding-to-rotor capacitances are important for the determination of the bearing voltage ratio [75]. However, the bearings are not included into our TL model. A comprehensive model is also found in [75]. As a prerequisite for this thesis, common mode currents are expected to evoke bearing currents, but the phenomena are not modelled as mutually coupled.

5.5.2 Linear Magnetic Analysis

The results, obtained from the small test model in Sec. 5.3 lead to the conclusion, that it is worth investigating the actual geometry of the 240 kW induction machine (IM) by means of 3D simulations. Only 3D simulations are capable to fully consider the eddy currents in the lamination. The goal is to quantify the amounts of electric loss and magnetic energy considering the eddy currents in a motor lamination sheet for a wide frequency range. The results are compared to the corresponding 2D motor model, which employs the equivalent permeability approach in order to account for eddy currents in the laminations (see Sec. 2.2.2).

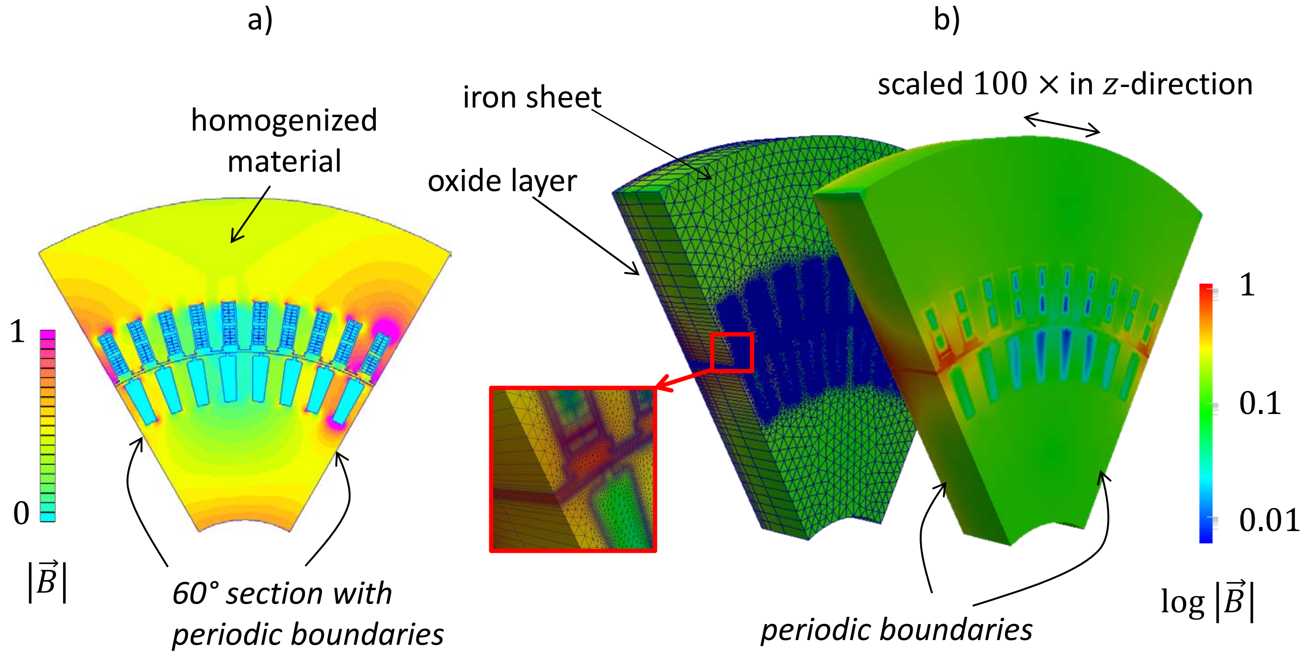

Figure 5.11.: *B-field of motor at 1 MHz, for the a) 2D and b) 3D model.*

The thickness of the lamination sheet is 0.65 mm, the insulating layer in between the sheet is assumed to be 0.05 mm thick, which yields a stacking factor of $F \approx 0.93$. The electric conductivities of copper and iron are $\kappa_{Cu} = 58$ MS/m and $\kappa_{Fe} = 2.63$ MS/m, respectively. The relative permeability of iron is assumed to be $\mu_{\mathrm{r,Fe}} = 1000$ in the linear analysis.

The electric conductivity of iron enables eddy-current flow, when the sheet is exposed to an alternating magnetic field. The eddy currents, in turn, produce an opposing magnetic field which leads to exponential decay of the total EM fields from the surface towards the inside of the sheet. The high permeability of iron strongly amplifies the field decline and leads to very small skin depths as the frequency of the exciting field increases. HF fields practically vanish inside the sheets. Therefore, HF eddy currents cannot be computed without an appropriate discretization of a small boundary layer on the surface of the lamination. Proportions of theoretical field decay and mesh discretization are visualized in Appendix A.5.

The preparation of the *sfem* code (see Sec. 4.4) allows for efficient 3D simulations of an actual motor. By discretising half the thickness of a lamination sheet and exploiting rotational periodicity, a 3D model containing 9.6 million degrees of freedom (DOFs) is created (Fig. 5.11b). Figure 5.11a shows the corresponding 2D model containing 200,000 DOFs.

The magnitudes of self-resistances and self-reactances of one stator conductor, extracted from 2D and 3D simulations, are plotted in Fig. 5.12. Resistance and reactance are associated with the losses and the magnetic field, respectively. The 2D solution which employs the equivalent permeability (Eq. 2.10) shows major discrepancies from the 3D reference case. For the purpose of validation, the same geometry is tested without laminated materials, i.e. the iron core is considered to be one massive conductive body. In this case, we obtain a pure 2D problem and, therefore, 2D and 3D analyses should yield the same results. The corresponding impedances are shown in Fig. 5.13. They are indeed in very good agreement.

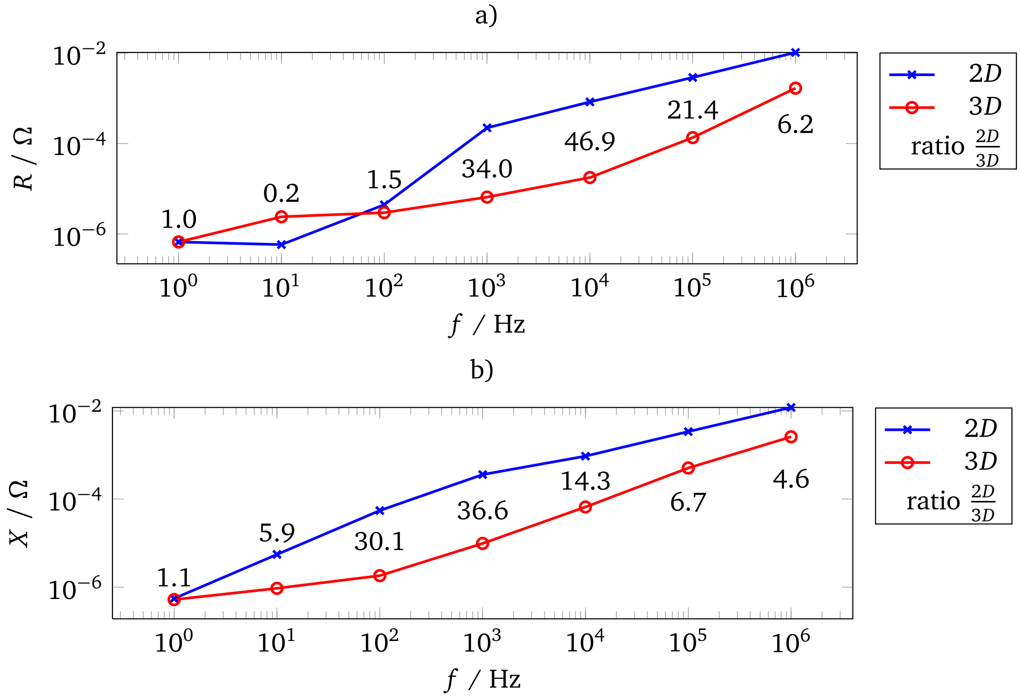

Figure 5.12.: *Self impedance Z11 of conductor one in 240 kW motor, 2D compared to 3D results.*

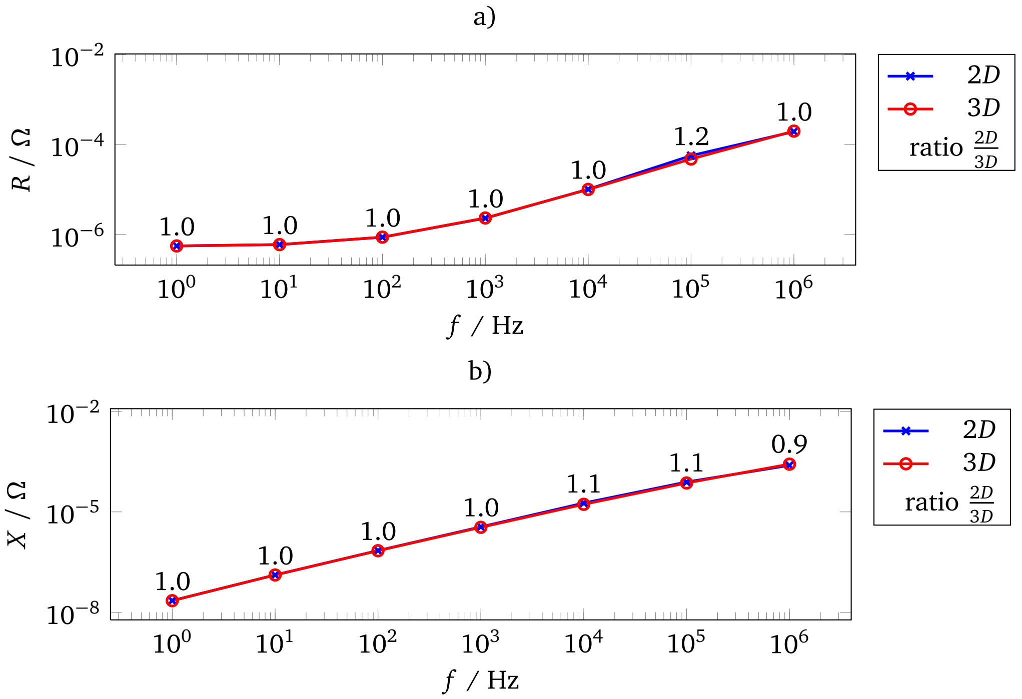

Figure 5.13.: *Self impedance Z11 of conductor one in non-laminated core, 2D compared to 3D results for validation of the 3D code.*

5.5.3 Nonlinear Magnetic Analysis

In this section, the possible influence of the nonlinear magnetisation curve of iron on eddy-current loss and stored magnetic energy is investigated. With, first, the use of the superposition principle in our transmission line (TL) approach and, second, the analysis in the frequency domain (FD), we have two important obstacles, which hamper the inclusion of nonlinear effects in a straightforward manner. However, when back coupling of the high-frequency (HF) components is assumed to be negligible (see Sec. 4.5.5), the actual B-H curve of the material, including saturation and hysteresis, can be taken into account. Owing to the limited material data on the electrical steel employed in the 240 kW motor, only a single valued B-H curve is considered in the following analysis.

The analysis is carried out in a two-step procedure. In step one, the permeability distribution inside the motor lamination is determined by means of FD simulations at 50 Hz, where $\mu(H)$ is updated considering the nonlinear B-H curve of the iron sheet (see Fig. 2.3). The low-frequency (LF) simulation is carried out with FEMM. Two different permeability distributions are generated. The first distribution is obtained from the application of a small three-phase current of only 10 A. Consequently, the iron is maintained unsaturated (Fig. 5.14a). The second, inhomogeneous, permeability distribution results from a current amplitude of 190 A (Fig. 5.14b). In the latter case, saturation effects are noticeable, especially in the teeth of the iron core.

Next, the spatial permeability distribution is extracted from the 2D field solution and used in linear 3D FD simulations at higher frequencies, in order to determine the influence of saturation on the impedance matrix of the multiconductor TL model. The impedance matrix is of size 120 × 120 and contains all self and mutual impedances of the stator conductors. Results of

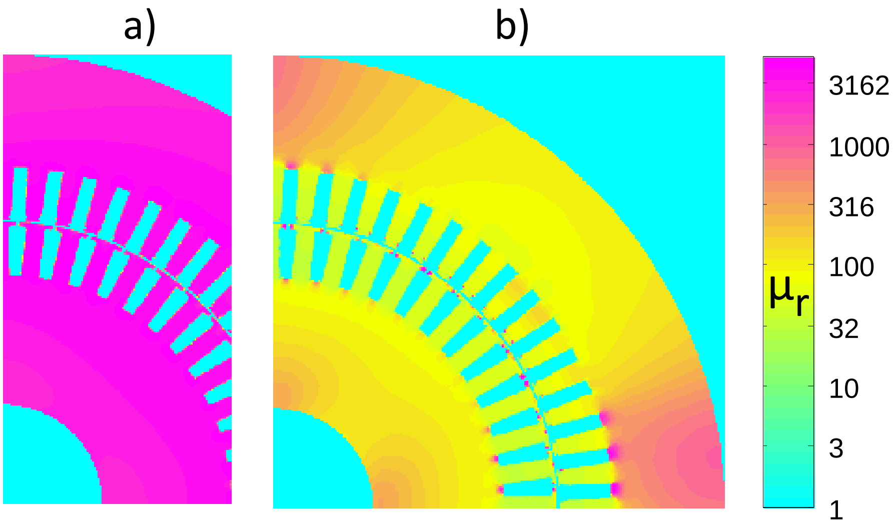

Figure 5.14.: *Relative permeability in the cross-section of the 240 kW motor in the a) non-saturated and b) saturated case. Image obtained with MATLAB® .*

both, the saturated and the unsaturated case, are compared in Fig. 5.15. The self-impedance of one conductor Z_{11} is taken exemplarily under consideration. Resistance and reactance of the Z_{ij} with $i, j = 1..120$ are associated with the losses and the magnetic flux, respectively. Saturation has noticeable impact on both.

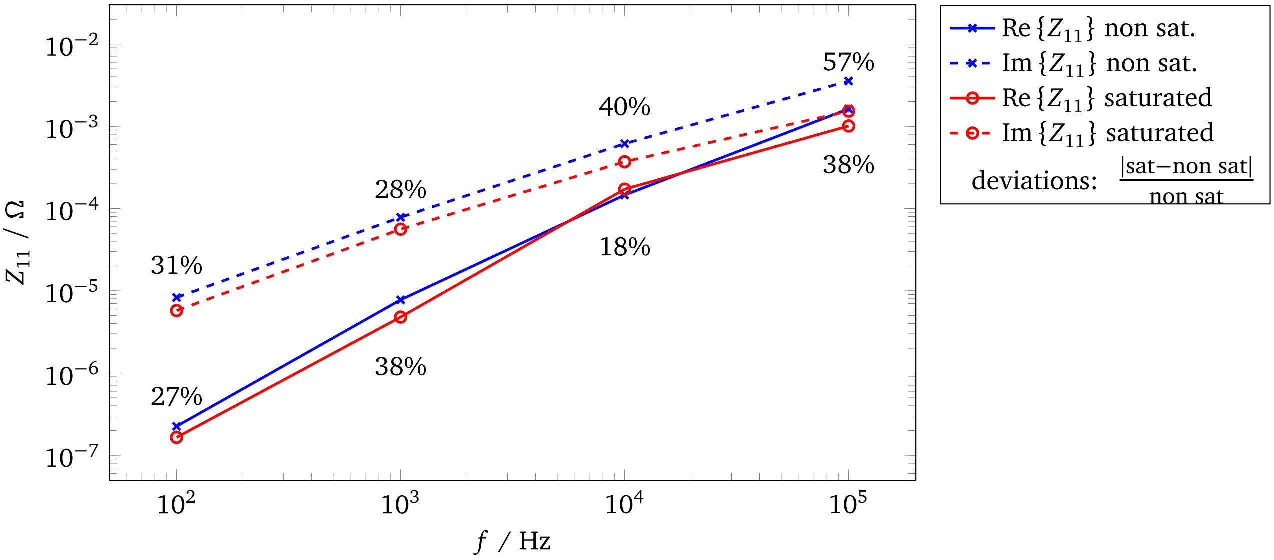

Figure 5.15.: *Real and imaginary part of HF TL impedance Z_{11} in the non-saturated and the saturated case, the relative deviation is shown.*

5.5.4 Evaluation of Common Mode Impedance

The common mode (CM) impedance of the motor is an essential quantity for determination of bearing currents from a lumped circuit model as presented in [75]. Due to the involved capacitive and inductive effects, the CM impedance is highly frequency dependent. It can be measured using an impedance analyser, while the rotor of the machine is removed.

After the determination of the capacitance and impedance matrices of the motor from field simulations, the frequency-dependent CM input impedance is calculated according to the scheme presented in Sec. 3.3.6. For comparison of the simulation results, measurements on the 240 kW induction machine (IM) (see red line in Fig. 5.16) have been kindly provided by the *Institute of Electrical Energy Conversion* of our university.

Owing to the fact, that the three-phase excitation is turned off during the measurements, the actual saturation effects, which are certainly occurring during normal machine operation, are not included in the measured data. Consequently, in order to compare with the measured results, our calculated impedance matrix is taken from the linear magnetic field analysis as described in Sec. 5.5.2, which neglects saturation effects.

In the low-frequency (LF) range, the CM impedance decreases with increasing frequency. It is determined mainly by the capacitive effects of the insulation between conductors and grounded metal parts such as the stator core. The CM impedance curve shows multiple resonances in the higher frequency range, which are attributed to the interplay of the distributed capacitances with distributed inductances.

Agreement between our calculated results to the measured curve is found only for low frequencies, however, the first two resonances are well represented by the simulations in terms of frequency, but less well in magnitude.

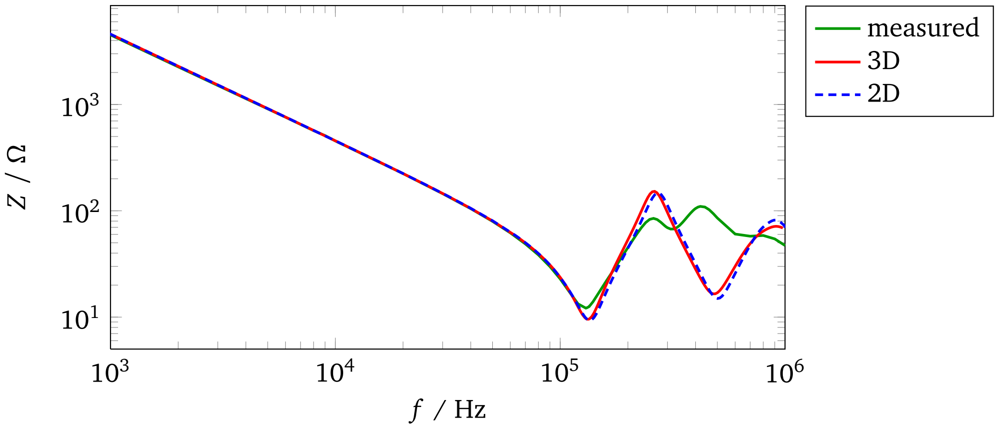

Figure 5.16.: *Comparison of $|Z_{CM}|$ of the 240 kW motor obtained from measurements and simulations in 3D and 2D.*

The 2D and 3D plots in Fig. 5.16 show very good agreement, despite the deviations in the impedance matrices (see Sec. 5.5.2). This is understandable since the stray capacitances are dominant in the CM circuit of the machine. However, the impedances are important to predict machine resonances. Compared to the 3D results, the frequency of the first resonance in the 2D curve is shifted by 6 kHz while its magnitude differs by 4 %.

5.5.5 End-Winding Analysis

In measurements, the end-winding inductance of a motor cannot be isolated from the rest of the motor and, therefore, a number of workarounds have evolved. A common method, to measure the total leakage inductance, is to remove the rotor and supply the stator with a three-phase voltage source [20]. Another approach, first proposed by Barnes in 1951 [8], determines the total motor inductances from a set of fictitious stator core lengths while the end-winding geometry is kept the same. Extrapolating the data to zero core length yields the pure end-winding inductance.

When using 3D finite element (FE) simulations, the end-winding inductance can be easily computed from the stored magnetic energy in the end-winding region. However, the end-region of the core is affected by the end-windings and vice versa [22]. In order to account for these effects in our investigations, the core end is modelled, while end-winding inductances are computed from the stored energy only in the end-winding region (see Fig. 2.6b).

In the first analysis, the model shown in Fig. 2.6 is used. It represents a simplified motor geometry including all rotor bars, the rotor end ring, stator frame and only one stator coil. The iron cores of the motor are modelled as a homogeneous material with zero conductivity in the axial direction. With this simplification, it is possible to use the software *CST* to analyse the problem.

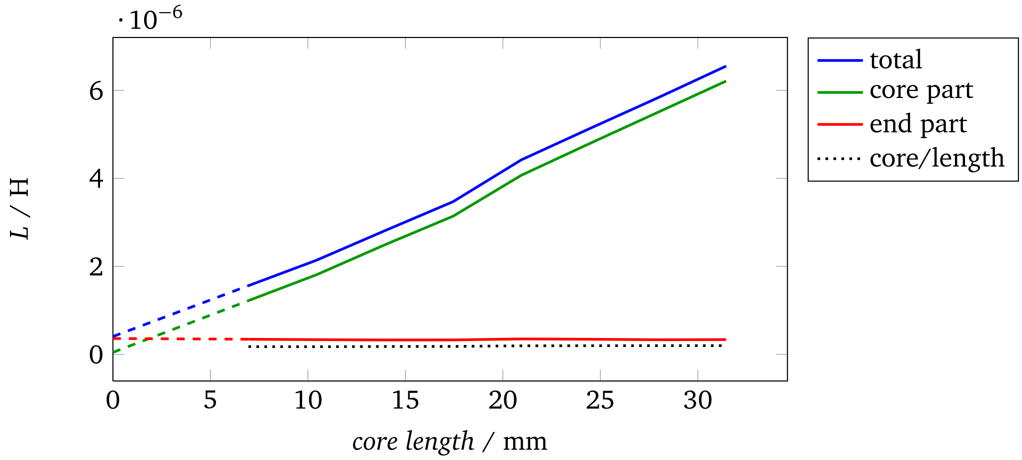

Figure 5.17.: *End-winding inductance from 3D model with homogenized core, variation of core length, extrapolation to zero core length.*

The stator coil is excited by AC current at 50 Hz. In a parameter study, the core length is modified and total inductance, core inductance, as well as end-winding inductance, are computed from the stored magnetic energy in the corresponding regions (Fig. 5.17). When the total inductance is extrapolated to zero core length, it meets exactly the end-winding inductance, as claimed in [8]. Furthermore, the figure nicely illustrates the proportion of core inductance to end-winding inductance, at least for this particular test motor geometry.

In the following investigation, the influence of the rotor bars on the stator end-winding inductance is analysed. Figure 5.18 shows the total inductance, as well as the end-winding inductance, for a varying core lengths. When the rotor conductors are removed from the model, the end-winding inductance increases by 40%. Therefore, the modelling of the rotor

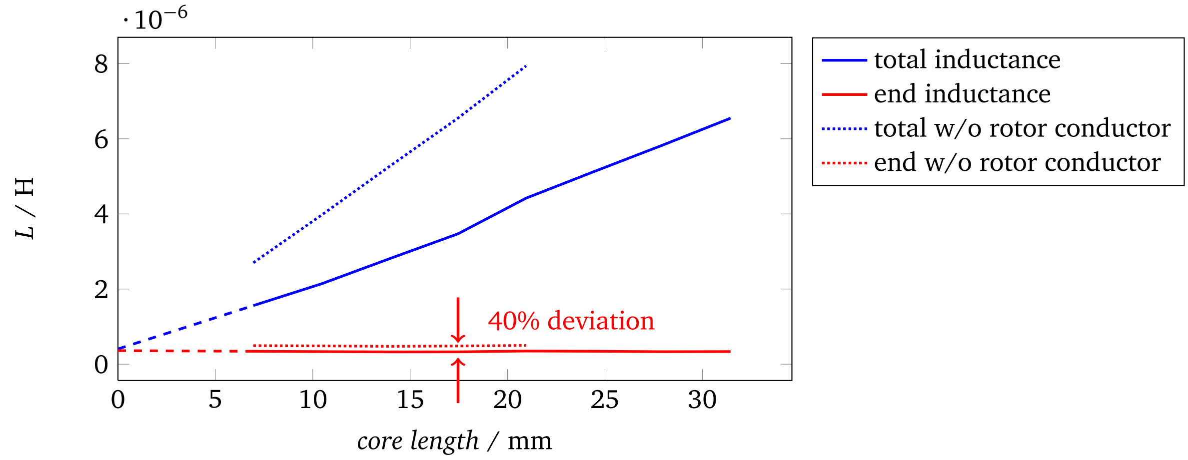

Figure 5.18.: *Comparison of total coil inductance and end-winding inductance with and without modelling the rotor bars.*

bars and end-ring is found to be crucial to accurate determination of the stator end-winding inductance.

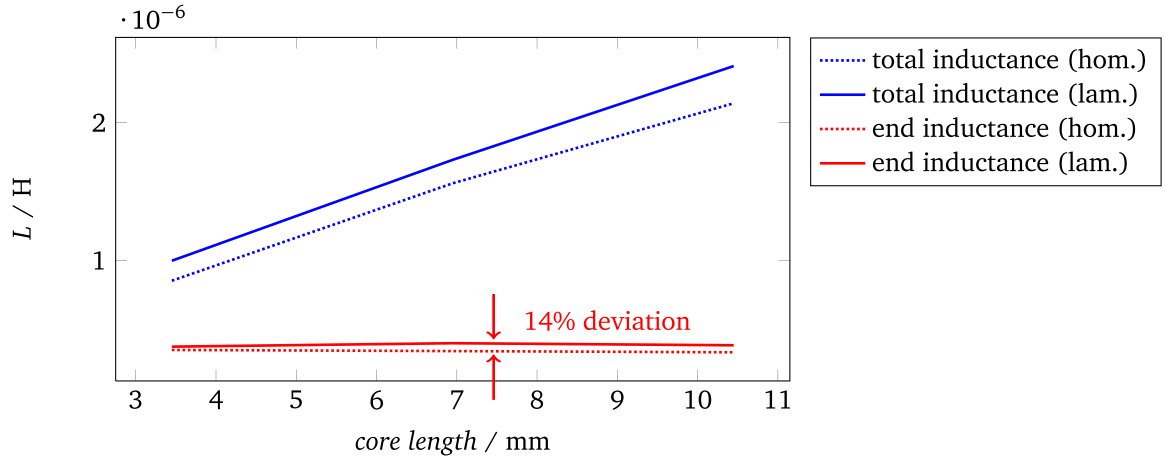

Figure 5.19.: *Comparison of total coil inductance and end-winding inductance with homogenized and laminated iron cores.*

In the third study of this section (see Fig. 5.19), the effect of the homogenized core is investigated at 50 Hz. Total and end-winding inductances are computed for homogenized as well as laminated iron core. The difference is found to be around 14%. From this result, we may conclude that the influence of the laminated core on end-winding inductance is quite noticeable. However, the effect is not as dominant as in the previous study with and without rotor bars and it has to be decided from case to case, if one is willing to spend the effort of modelling individual laminations.

In order to investigate eddy currents in the laminations of the core end-region, a finer discretization of the thin iron sheets is necessary, which, in turn, leads to an increase in problem size. After solving the FE problem, the losses and the stored magnetic energy have to be calculated for several subregions, which turns out to be quite time consuming with *CST* software. In the *sfem* code, a special subroutine was implemented to collect data on the fly which is used later for

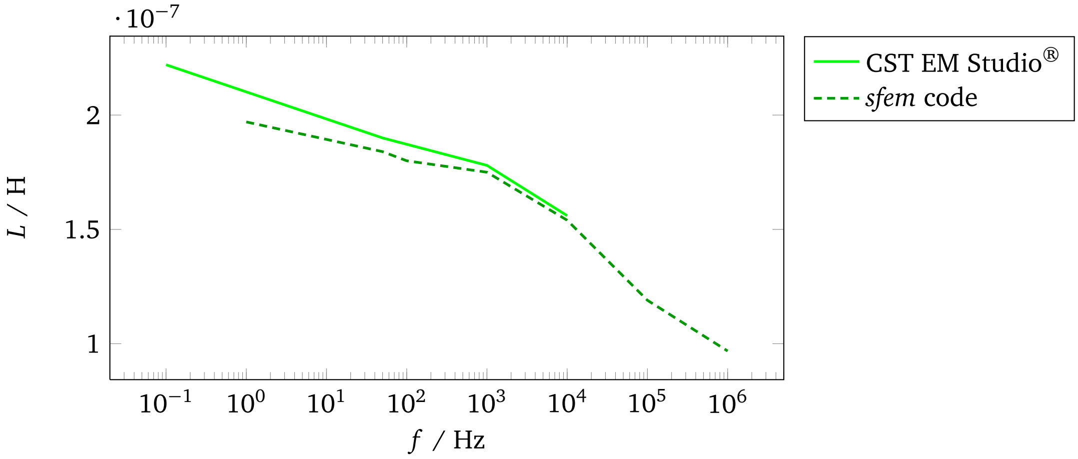

Figure 5.20.: *End-winding inductance of 3D models.*

the magnetic energy calculation. Thus, a considerable speed-up compared to the conventional post-processing was achieved.

Nevertheless, both simulation programs yield matching results, at least for higher frequencies (Fig. 5.20). The increasing deviation in the lower frequency range, e.g. at 1 Hz is due to the different modelling philosophies of both programs. While the *sfem* code uses the cross-section area of conductors to apply the electric potentials, in *CST* EM studio up to version 2013 only voltage or current paths are available for excitation of MQS problems. These paths are added to the geometry and, as a consequence, the geometry of the *CST* model and the *sfem* model are not completely identical anymore. The small additional volume, modelled as vacuum, around the exciting current path in the *CST* model leads to a different field distribution than in the *sfem* model which are noticeable in the low frequency range.

The parallelized *sfem* code is run on 28 computing nodes. First order computations on a grid with 1.5 million mesh cells, as well as second order computations on grids with up to $600,000$ mesh cells, yield the desired results within a few minutes. Figure 5.21a shows a plot of the amplitude of magnetic flux density $|\vec{B}|$ at 10 kHz.

For efficient modelling, the mesh used by *sfem* is composed of tetrahedrons in the end-region parts and triangular prisms in the adjacent part of the core region. Figure 5.21b shows a relatively coarse discretization with $100,000$ mesh cells of the end-winding region. However, using high-order methods ensures accurate modelling of the eddy-current distributions in the metals. For comparison, a convergence study with a set of first order computations is carried out, see Fig. 5.22.

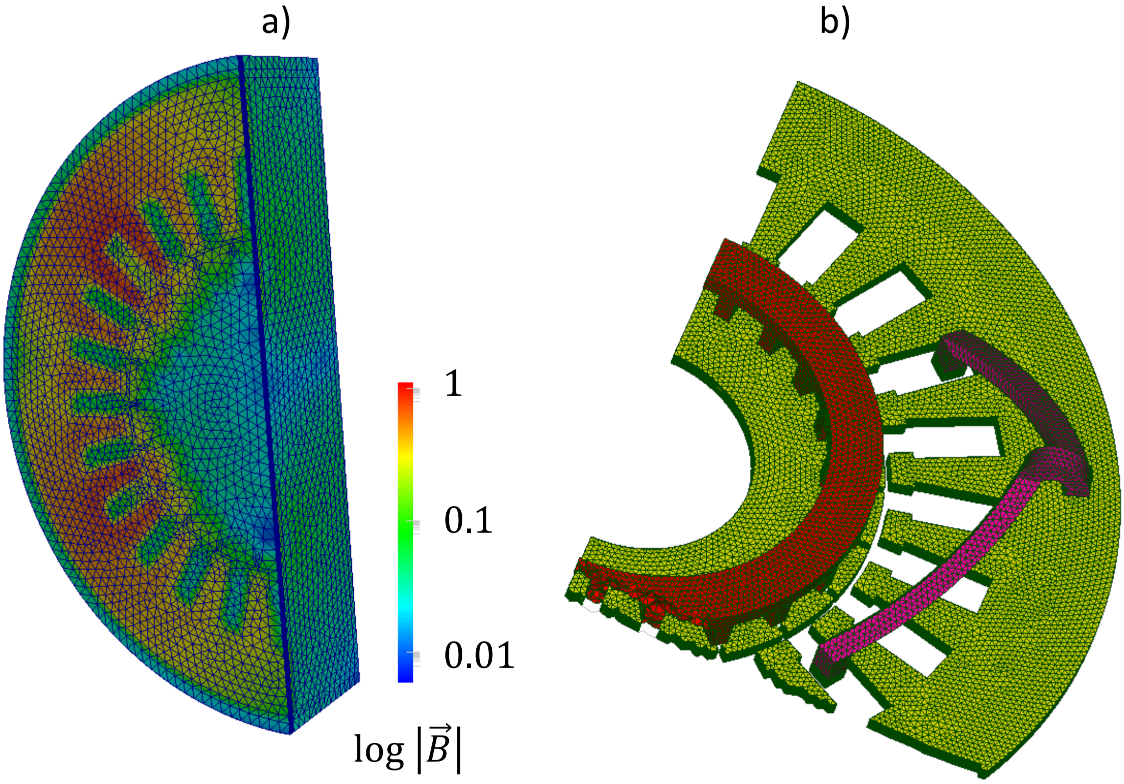

Figure 5.21.: *End-winding model, a) B-field plot at 10 kHz (plot with ParaView), b) part of mesh (image with SALOME).*

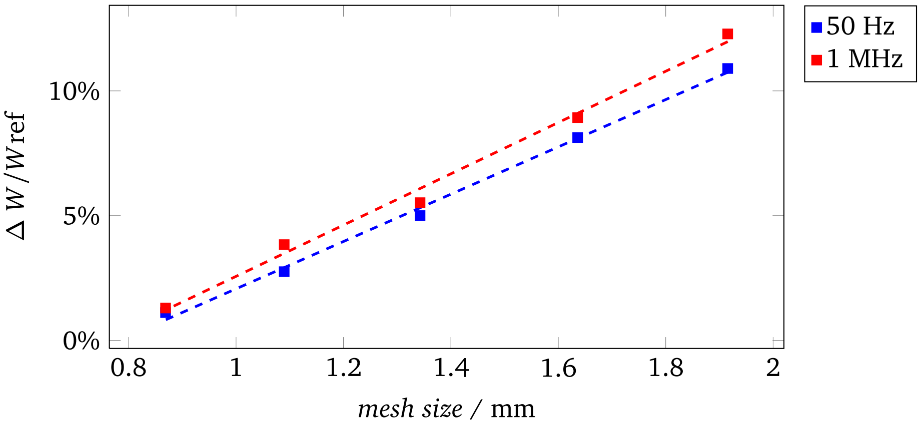

Figure 5.22.: *Convergence plot of 3D end-winding analysis with the sfem code. The deviation* $\Delta W/W_{ref} = \frac{|W - W ref|}{W ref}$, relative to a reference solution with *mesh size* $= 0.66$ mm, is shown.

6 Summary and Outlook

In this thesis, high-frequency models for induction machines have been thoroughly discussed. Existing approaches have been analysed and new extensions to the transmission line model were proposed. Concerning the restriction of field simulations to a single stator slot, it has been shown, that high-frequency fields lead to coupling between the slots and, therefore, the analysis of the entire motor cross-section is necessary. Subsequently, the field analysis has been extended to three dimensions, in order to allow for explicit modelling of eddy currents in the lamination.

As a major task of this work, a method has been developed which is well adapted to the purpose of investigating high-frequency fields in electrical machines with laminated iron cores. A specialized three-dimensional finite element simulation tool has been established which can be used for efficient extraction of the impedance matrix of a large induction motor model. Since the laminated iron is modelled with its actual geometry and material properties, 3D results are more accurate than those obtained from 2D simulations based on a homogenization approach. Capacitance matrix, impedance matrix and winding scheme are combined to compute the frequency-dependent common mode input impedance of the machine. It can be observed that this impedance is dominated by the capacitances and, therefore, less sensitive to inaccuracies in the magnetic field simulations.

Our motor modelling approach has been complemented by the analysis of nonlinear phenomena. The proposed method is able to account for the actual magnetisation curve of the core material by means of an approximate solution in frequency domain. It was found that the inclusion of low frequency saturation effects might be important for the calculation of high-frequency parameters of the machine.

End-winding analysis provides a valuable addition to the analysis of the motor core. Therefore, the subject has also been tackled in this thesis. Our 3D finite element code has been used to compute end-winding fields of a motor model. The discussion shows which motor parts have the greatest influence on the fields in the end region.

Although this thesis already comprises a variety of modelling procedures, some research aspects remain to be addressed in the future. The analysis has been restricted to an upper frequency limit of 1 MHz, since the small skin depth of the fields inside the iron requires an extremely fine mesh on the sheet surface. High frequencies require a very high number of degrees of freedom (DOFs) for the discrete problem, which finally limits the model size. Instead of further refining the discretization, the applicability of 3D homogenization methods could be discussed to extend the frequency range to 10 MHz.

The nonlinear approach, presented in this thesis, could potentially be extended. Accuracy will be increased by using a time domain simulation in order to derive the permeability distribution, which is then employed in the high-frequency frequency domain method.

Simplifications in the calculation of the end-winding inductances is also worth serious consideration. As they account only for a small part of the total motor inductance, expensive 3D methods may not be justified.

A concluding idea is to analyse the interdependence of common mode fields and bearing currents in terms of 3D field analysis. As computational power is continuously increasing, a comprehensive high-frequency machine model will become possible in the future.

A Appendix

A.1 Motional Induction

Electromagnetic induction is described by FARADAY's law, which in a general formulation reads

$$\oint_{\partial A1} \vec{E}(\vec{r},t)\cdot \mathrm{d}\vec{l} = -\frac{\mathrm{d}}{\mathrm{d}t}\int_{A1} \vec{B}(\vec{r},t)\cdot \mathrm{d}\vec{A}. \tag{A.1}$$

Please note, that Eq. A.1 encompasses the total change of magnetic flux $-\mathrm{d}\Phi/\mathrm{d}t$, which can be attributed to two types of induction. The first one is due to a time-varying $\vec{B}$-field and the second arises from moving conductors. The induced electromotive force (emf) then yields

$$U_{\mathrm{emf}} = -\int_{A1} \frac{\partial \vec{B}}{\partial t}\cdot \mathrm{d}\vec{A} + \oint_{C1} \left(\vec{v}\times\vec{B}\right)\cdot \mathrm{d}\vec{l}, \tag{A.2}$$

where vector $\vec{v}$ denotes the relative velocity between the field producing conductor (i.e. in the stator) and the conductor experiencing the emf (i.e. in the rotor). The first term on the right hand side of Eq. A.2 is also referred to as 'transformer' induction, while the second term is called 'motional induction term'.

We may argue that the 'transformer induction term' in Eq. A.2 will increase with increasing frequency of the exciting field $\vec{B}$, while the 'motional induction term' is independent of frequency. For this reason, we may neglect the motional induction in the investigation of high frequency fields.

Nevertheless, it is possible to add a motional term to the problem definition. As an extension to Eq. (4.24), the harmonic magnetoquasistatic (MQS) problem in terms of the magnetic vector potential (MVP) can be formulated as

$$\nabla\times\frac{1}{\mu}\nabla\times\vec{A} + \kappa\left(j\omega\vec{A} - \vec{v}\times\nabla\times\vec{A}\right) = \vec{J}_s. \tag{A.3}$$

However, in our investigations we omitted the approach of Eq. A.3.

A.2 Definition of line voltage and current

The TEM mode allows to define a unique voltage between the conductors and a unique current in the given conductor at any point of the transmission line. We will derive the relations from the integral form of MAXWELL's equations:

$$\oint_{C1} \vec{E} \cdot \mathrm{d}\vec{l} = -\mu \frac{\partial}{\partial t} \int_{A1} \vec{H} \cdot \mathrm{d}\vec{A}, \tag{A.4a}$$

$$\oint_{C1} \vec{H} \cdot \mathrm{d}\vec{l} = \kappa \int_{A1} \vec{E} \cdot \mathrm{d}\vec{A} + \epsilon \frac{\partial}{\partial t} \int_{A1} \vec{E} \cdot \mathrm{d}\vec{A}, \tag{A.4b}$$

where $C1$ is a closed contour around the given conductor in a transverse plane of the line. $A1$ is the area enclosed by $C1$ and, therefore, also perpendicular to the direction of wave propagation. The term on the right hand side of Eq. (A.4a) is equal to zero, since $H_z = 0$. Accordingly, the second term on the right hand side of Eq. (A.4b) equals zero because it is $E_z = 0$. We obtain:

$$\oint_{C1} \vec{E} \cdot \mathrm{d}\vec{l} = 0, \tag{A.5a}$$

$$\oint_{C1} \vec{H} \cdot \mathrm{d}\vec{l} = \kappa \int_{A1} \vec{E} \cdot \mathrm{d}\vec{A}. \tag{A.5b}$$

Equation (A.5a) takes the same form as in the electrostatic case and leads to the conclusion, that a unique voltage can be defined between the two conductors. On the other hand, Eq. (A.5b) reduces to the same form as in the magnetostatic case and results in a current definition. We finally yield

$$\oint_{C2} \vec{E} \cdot \mathrm{d}\vec{l} = U, \tag{A.6a}$$

$$\oint_{C1} \vec{H} \cdot \mathrm{d}\vec{l} = I, \tag{A.6b}$$

where $C2$ is an arbitrary contour between the conductors in a transverse plane of the line. U is the voltage between the conductors and I is the line current, which both are dependent on the z-coordinate.

A.3 Lossy Transmission Lines

Assuming an ideal two-conductor line, which has a homogeneous dielectric with its permeability μ and permittivity ε, both, being independent of frequency, all the natural propagation modes have the same propagation velocity [71], namely

$$v = \sqrt{\frac{1}{\mu\varepsilon}}. \tag{A.7}$$

In the case of vacuum, the delimiting wavelength λ of the modes can be computed approximately as

$$\lambda = \frac{v}{f} = \frac{300,000 \text{ km/s}}{1 \text{ MHz}} = 300 \text{ m}, \tag{A.8}$$

where v is the speed of light in vacuum and f is the highest frequency considered in this thesis.

The circumstances are different, when a *lossy* line is considered. Not only that the propagation of a wave along a lossy line is damped, but also the phase velocity depends upon the frequency, and the signal is propagated with distortion. In other words, a lossy multiconductor TL is generally dispersive. An exception is the distortionless line as formulated by Heaviside in 1887 [45]. Moreover, dispersion also occurs in *inhomogeneous* dielectrics, as known from Microstrip Transmission Lines [105].

The conclusion of this section is, that the actual modal wavelengths of our multiconductor TL model are different from the value obtained in Eq. (A.8). They must be calculated with the matrix of eigenvalues in Eq. (3.8). However, Eq. (A.8) can be used to estimate the influence of wave propagation effects for a specific line length.

A.4 Computation of Z_{CM}, Φ, P for one-conductor model

The common mode impedance of the one-conductor model placed in a lamination stack (see Sec. 5.1) is computed from the distributed parameter line equations (A.9).

$$\begin{pmatrix} \underline{U}(z) \\ \underline{I}(z) \end{pmatrix} = \begin{pmatrix} \cosh\left(\underline{\gamma}(l-z)\right) & \underline{Z}_c \sinh\left(\underline{\gamma}(l-z)\right) \\ \underline{Z}_c^{-1} \sinh\left(\underline{\gamma}(l-z)\right) & \cosh\left(\underline{\gamma}(l-z)\right) \end{pmatrix} \cdot \begin{pmatrix} \underline{U}(l) \\ \underline{I}(l) \end{pmatrix} \tag{A.9}$$

with

$$\underline{Z}_{\mathrm{c}} = \sqrt{(R' + j\omega L')/(G' + j\omega C')}$$

being the characteristic impedance of the line and

$$\underline{\gamma} = \sqrt{(R' + j\omega L')(G' + j\omega C')}$$

being the complex propagation constant. From the state of the line at $z = 0$ we obtain the common mode impedance as

$$\underline{Z}_{\mathrm{CM}} = \frac{\underline{U}(0)}{\underline{I}(0)} = \underline{Z}_{\mathrm{c}} \coth(\underline{\gamma} l). \tag{A.10}$$

Because the line appears to be electrically short in the low frequency range, Z_{CM} can also be computed from the lumped parameter π- or T-equivalent circuit. For the same reason, circumferential flux and loss are simply computed, assuming the current decreasing linearly along the line. We obtain:

$$\Phi = \frac{1}{2}\, L\, |\underline{I}(0)| \tag{A.11}$$

$$P = \frac{2}{3}\, R\, |\underline{I}(0)|^2 \tag{A.12}$$

A.5 Skin depth

The metal sheet has to be discretized carefully in order to represent the exponentially decaying fields appropriately, especially when the same mesh is used for various frequencies. A rule of thumb is suggesting that the mesh element size should be three times smaller than the skin depth. However, this would increase the number of mesh cells in our model dramatically. Therefore, we used convergence studies of a test model to define an optimal mesh topology, which is as coarse as possible, but still remains inside an error limit of 10% for the highest frequency considered, i.e. 1 MHz. The distribution of the mesh layers is shown in Fig. A.1. Note that the oxide layer is nonconductive and, therefore, discretised by only one mesh layer, because fields are assumed to be constant.

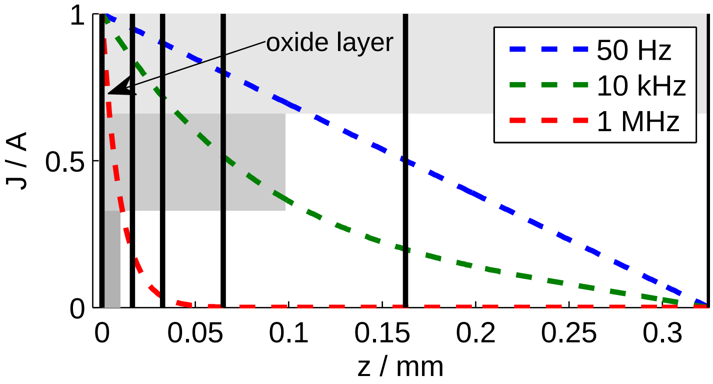

Figure A.1.: *Analytical 1D eddy-current density in the iron sheet. Black lines indicate mesh layers in the 3D model. Grey rectangles denote skin depth at the three frequencies considered.*

A.6 Specification of 240 kW motor

A.6.1 Motor Data

SIEMENS traction motor $1TB2022-0TA02$		
no. of phases	3	
rated voltage	1375	V
maximum voltage	1404	V
rated current	120	A
maximum current	190	A
rated speed	2000	rpm
maximum speed	4041	rpm
rated torque	1147	Nm
rated power	240	kW

Table A.1.: *Electromechanical data of 240 kW induction motor.*

	stator	rotor
poles	4	
slots	60	48
slots per pole per phase	5	
sub-conductors per slot	24	
parallel sub-conductors	2	
parallel branches	2	
no. of turns	60	
sub-conductors blank	3.08 × 1.73 mm	6.65/9.95 × 26.85 mm
sub-conductors insulated	3.25 × 1.90 mm	
electrical sheet	M530-65A	M530-65A

Table A.2.: *Geometrical data of 240 kW induction motor.*

A.6.2 Motor Winding

One quarter of the winding layout of a double layer 4-pole 60-slot winding is depicted in Fig. A.2. The letters U,V,W denote the three phases of the winding, the $+/-$ indicate the conductor orientation. The second and the fourth quarter of the winding have changed indications $-/+$. The third winding quarter is identical to the first one. Each coil side is distributed over 5 slots. The coils have a span of 12 slot pitches. There are two coils per phase, which are interconnected in parallel.

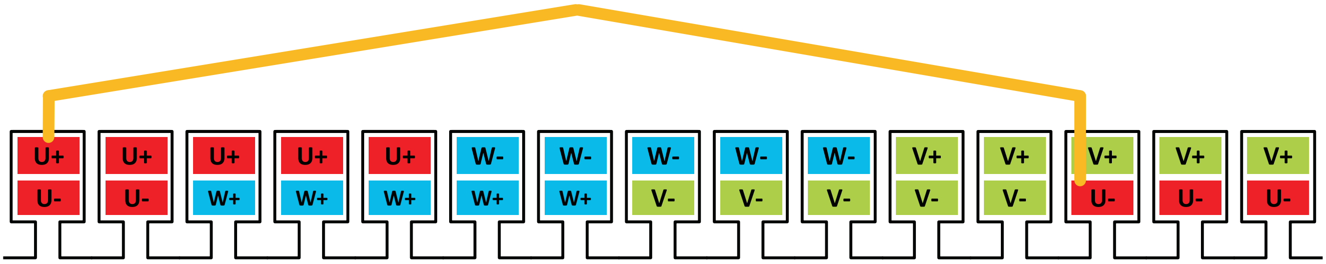

Figure A.2.: 1/4 *of a winding layout of a double layer 4-pole 60-slot winding with distributed coils and two parallel coils per phase.*

Glossary

electrically short

In electrically short transmission lines, propagating wave effects can be neglected.

electrostatic discharge (ESD)

ESDs occur when objects of different potential come to close proximity, where electrostatic charges start to transfer between the objects. ESDs are very short but can produce large current or voltage surges that may cause damage to a device.

full-wave

The term full-wave refers to the solution of the full set of MAXWELL's equations.

high-frequency (HF)

$1\ \mathrm{kHz} < f \leq 1\ \mathrm{MHz}$, includes the fundamental frequency of the pulse-width modulation (PWM) inverter and HF pulses triggered by short rise times or high $\mathrm{d}v/\mathrm{d}t$ of the semiconductor devices, especially in Insulated Gate Bipolar Transistors (IGBT).

low-frequency (LF)

$0\ \mathrm{Hz} < f \leq 1\ \mathrm{kHz}$, covers the base operating frequency of power supply as well as classical subharmonics and harmonics.

LU decomposition

Factorization of a matrix into an upper and a lower triangular matrix.

magnetoquasistatic (MQS)

Within the magnetoquasistatic limit, the impact of displacement current is small compared to that of conduction current, and can be neglected.

proximity effect

Frequency dependent concentration of currents in regions with high magnetic field strength.

quasi-TEM

If losses are significant but frequencies sufficiently low, a quasi-TEM mode is formed. This means, the longitudinal components of electric and magnetic field are still very small compared to the transversal ones. Thus, the TL approach can be used.

skin effect

Penetration of high-frequency fields into the surface of metals.

TEMF

Institut für Theorie elektromagnetischer Felder, TU Darmstadt, Germany.

Acronyms

1D	one-dimensional
2D	two-dimensional
3D	three-dimensional
AC	alternating current
ASD	adjustable-speed drive
BVR	bearing voltage ratio
CM	common mode
DC	direct current
DOFs	degrees of freedom
EM	electromagnetic
ES	electrostatic
FD	frequency domain
FE	finite element
GUI	graphical user interface
HB	harmonic balance
HF	high-frequency
IGBT	Insulated Gate Bipolar Transistor
IM	induction machine
LF	low-frequency
MOSFET	Metal Oxide Semiconductor Field-Effect Transistor
MQS	magnetoquasistatic
MVP	magnetic vector potential
PBCs	periodic boundary conditions
PEC	perfect electric conductor
PWM	pulse-width modulation
rpm	revolutions per minute

SC	stationary current
TD	time domain
TEM	transverse electromagnetic
TL	transmission line
VFD	variable-frequency drive

Symbols

α	°	period angle
A	m^2	area
$\boldsymbol{a}$		vector of unknowns in FE equation
$\vec{B}$	$\mathrm{Vs/m}^2$	vector of magnetic flux density
C'	F/m	capacitance per unit length of the line
$\mathrm{d}\vec{A}$		infinitesimal area element (oriented)
δ	m	skin depth
$\boldsymbol{D}$		projection matrix to couple wire voltages to FE equation
$\vec{D}$	$\mathrm{C/m}^2$	vector of electric flux density
$\vec{E}$	V/m	vector of electric field strength
F		stacking factor
f	Hz	frequency
$\underline{\gamma}$		complex propagation constant
G'	S/m	conductance per unit length of the line
$\boldsymbol{H}$		complex FE system matrix
H_S	A/m	magnetic field on the surface of a lamination
$\vec{H}$	A/m	vector of magnetic field strength
I	A	current
i	A	current
$\underline{\mathrm{I}}$	A	complex current
I_{CM}	A	common mode current
U_DC	A	DC (direct current) link voltage
$\boldsymbol{i}$		source term in FE equation
$\boldsymbol{i}_\mathrm{w}$	A	vector of wire currents
j		imaginary number
$\underline{\mathrm{J}}$	$\mathrm{A/m}^2$	complex current density
$\vec{J}$	$\mathrm{A/m}^2$	vector of current density
κ	S/m	electric conductivity

l	m	length
λ	m	wavelength
$\boldsymbol{\Lambda}$		diagonal matrix of eigenvalues
L'	H/m	inductance per unit length of the line
m		number of degrees of freedom
$\boldsymbol{M}$		material dependend matrix in FE equation
μ	H/m	magnetic permeability $\mu = \mu_0 \mu_r$
μ_0	H/m	permeability of vacuum $\mu_0 = 4\pi 10^{-7}$ H/m
μ_{eq}	H/m	equivalent permeability accounting for eddy currents
μ_{r}		relative permeability
N		number of conductors
$\vec{n}$		normal vector
ω	1/s	angular frequency
p_{DC}	$\mathrm{W/m^3}$	static loss density
P_{ed}	W	classical eddy-current loss
p_{ed}	$\mathrm{W/m^3}$	eddy-current loss density
P_{el}	W	electric loss
P_{ex}	W	excess loss
p_{ex}	$\mathrm{W/m^3}$	excess loss density
φ	rad	azimuthal angle in cylindrical and spherical coordinates
$\underline{\Phi}$	Vs	complex magnetic flux
P_{hy}	W	hysteresis loss
p_{hy}	$\mathrm{W/m^3}$	hysteresis loss density
P_{iron}	W	iron loss
Q	C	electric charge
R	Ω	resistance
ϱ	$\mathrm{C/m^3}$	charge density with $Q = \int_V \varrho \, \mathrm{d}V$
R'	Ω/m	resistance per unit length of the line
S_{n}	$\mathrm{W/m^2}$	normal component of Poynting vector
$\vec{S}$	$\mathrm{W/m^2}$	Poynting vector
t	s	time
$\mathbf{T}$		matrix of eigenvectors
u	V	voltage
$\underline{U}$	V	complex voltage
U_{CM}	V	common mode voltage
$\boldsymbol{u}_{\mathrm{w}}$	V	vector of wire voltages

v	m/s	velocity
$\vec{v}$	m/s	velocity vector
W_{mag}	J	magnetic energy
x	m	Cartesian coordinate
y	m	Cartesian coordinate
$\mathbf{Y}$	S	admittance matrix
z	m	Cartesian coordinate
$\underline{Z}$	Ω	complex impedance
Z_{CM}	Ω	common mode impedance
$\mathbf{Z}$	Ω	matrix of impedances

Bibliography

[1] *SALOME: The Open Source Integration Platform for Numerical Simulation*, 2009-2013, available at: http://www.salome-platform.org/. (Cited on page 5.)

[2] *PETSc: Portable, Extensible Toolkit for Scientific Computation*, 2010, available at: http://www.mcs.anl.gov/petsc/. (Cited on page 36.)

[3] *ParaView, open-source data analysis and visualization application*, Version 4.0.0 for Windows 64 bit, 2010, available at: http://www.paraview.org/. (Cited on page 5.)

[4] *CST - Computer Simulation Technology*, Versions 2010-2013, hompage: https://www.cst.com/. (Cited on page 6.)

[5] ABB, "Technical guide no. 5, bearing currents in modern ac drive systems," Tech. Rep., 2011. (Cited on page 1.)

[6] M. Ainsworth, J. Coyle, P. Ledger, and K. Morgan, "Computing Maxwell eigenvalues using higher order edge elements in three dimension," *IEEE Transactions on Magnetics*, vol. 39 no. 5, pp. 2149–2153, 2003. (Cited on page 29.)

[7] S. Ausserhofer, O. Bíró, and K. Preis, "An Efficient Harmonic Balance Method for Nonlinear Eddy Current Problems," *Proceedings of The 12th IEEE Conference on Electromagnetic Field Computation*, p. 22, 2006. (Cited on page 43.)

[8] E. C. Barnes, "An Experimental Study of Induction Machine End-Turn Leakage Reactance," *American Institute of Electrical Engineers, Transactions of the*, vol. 70, no. 1, pp. 671–679, 1951. (Cited on page 60.)

[9] M. L. Barton and Z. Cendes, "New vector finite elements for three-dimensional magnetic field computation," *Journal of Applied Physics*, vol. 61, no. 8, pp. 3919–3921, 1987. (Cited on page 35.)

[10] J. P. A. Bastos and N. Sadowski, *Electromagnetic Modeling by Finite Element Methods*. CRC Press, 2003. (Cited on pages 9 and 29.)

[11] A. Belahcen, "Magnetoelasticity, magnetic forces and magnetostriction in electrical machines," Ph.D. dissertation, Helsinki University of Technology, 2004. (Cited on page 11.)

[12] G. Bertotti, "General properties of power losses in soft ferromagnetic materials," *IEEE Transactions on Magnetics*, vol. 24 no. 1, pp. 621–630, 2005. (Cited on pages 11, 12, and 13.)

[13] G. Bertotti and I. D. Mayergoyz, *The Science of Hysteresis, 3-volume set*. Oxford, UK: Academic Press, 2006. (Cited on page 11.)

[14] O. Biro, "Edge element formulations of eddy current problems," *Computer Methods in Applied Mechanics and Engineering*, vol. 169 no. 3-4, pp. 391–405, 1999. (Cited on page 35.)

[15] O. Biro, K. Preis, and I. Ticar, “A FEM method for eddy current analysis in laminated media,” *COMPEL: The International Journal for Computation and Mathematics in Electrical and Electronic Engineering*, vol. 24 no. 1, pp. 241–248, 2005. (Cited on page 26.)

[16] I. Boldea and S. A. Nasar, *The Induction Machines Design Handbook*. New York, NY: CRC Press, 2010. (Cited on pages 2, 4, 16, and 25.)

[17] A. Bossavit, “Two dual formulations of the 3-D eddy-currents problem,” *COMPEL: The International Journal for Computation and Mathematics in Electrical and Electronic Engineering*, vol. 4 no. 2, pp. 103–116, 1985. (Cited on page 35.)

[18] ——, “The exploitation of geometrical symmetry in 3-D Eddy-currents computation,” *Magnetics, IEEE Transactions on*, vol. 21, no. 6, pp. 2307–2309, 1985. (Cited on page 41.)

[19] R. M. Bozorth, *Ferromagnetism*. New Jersey: D. Van Nostrand Co. Inc. Princeton, 1951. (Cited on page 13.)

[20] T. A. Brahimi, A. Foggia, and G. Meunier, “End winding reactance computation using a 3D finite element program,” *Magnetics, IEEE Transactions on*, vol. 29, no. 2, pp. 1411–1414, 1993. (Cited on page 60.)

[21] D. S. Burnett, *Finite element analysis: from concepts to applications*. Addison-Wesley Pub. Co., 1987. (Cited on page 34.)

[22] C. J. Carpenter, “The application of the method of images to machine end-winding fields,” *Proceedings of the IEE - Part A: Power Engineering*, vol. 107, no. 35, pp. 487–500, 1960. (Cited on pages 16 and 60.)

[23] Z. J. Cendes, “Vector finite elements for electromagnetic field computation,” *IEEE Transactions on Magnetics*, vol. 27, pp. 3958–3966, 1990. (Cited on page 35.)

[24] C. C. Chan and K. T. Chau, *Modern Electric Vehicle Technology*. Oxford University Press, 2001. (Cited on page 15.)

[25] S. Chen, T. Lipo, and D. Fitzgerald, “Source of induction motor bearing currents caused by PWM inverters,” *IEEE Transaction on Energy Conversion*, vol. 11 no. 1, pp. 25–32, 1996. (Cited on pages 1 and 3.)

[26] O. Chiver, E. Micu, and C. Barz, “Stator winding leakage inductances determination using finite elements method,” in *Optimization of Electrical and Electronic Equipment, 2008. OPTIM 2008. 11th International Conference on*, 2008, pp. 69–74. (Cited on page 16.)

[27] M. Cirrincione, M. Pucci, and G. Vitale, *Power Converters and AC Electrical Drives with Linear Neural Networks*. CRC Press, 2012. (Cited on page 15.)

[28] H. De Gersem, O. Henze, T. Weiland, and A. Binder, “Simulation of wave propagation effects in machine windings,” *COMPEL: The International Journal for Computation and Mathematics in Electrical and Electronic Engineering*, vol. 29 no. 1, pp. 23–38, 2010. (Cited on pages 3, 21, 25, and 37.)

[29] H. De Gersem and A. Muetze, “Finite-Element Supported Transmission-Line Models for Calculating High-Frequency Effects in Machine Windings,” *IEEE Transactions on Magnetics*, vol. 48 no. 2, pp. 787–790, 2012. (Cited on page 3.)

[30] H. De Gersem, H. V. Sande, and K. Hameyer, “Strong coupled multi-harmonic finite element simulation package,” *COMPEL: The International Journal for Computation and Math-*

ematics in Electrical and Electronic Engineering, vol. 20 no. 2, pp. 535–546, 2001. (Cited on page 43.)

[31] R. M. Del Vecchio, “The calculation of eddy current losses associated with rotating magnetic fields in thin laminations,” *IEEE Transactions on Magnetics*, vol. 18 no. 6, pp. 1707–1709, 1982. (Cited on page 13.)

[32] L. Demkowicz, “Edge Finite elements of variable order for Maxwell’s equations - a discussion,” *Technical report, TICAM*, pp. 00–32, 2000. (Cited on page 29.)

[33] E. Dlala, “Magnetodynamic vector hysteresis models for steel laminations of rotating electrical machines,” Ph.D. dissertation, Helsinki University of Technology, 2008. (Cited on pages 11 and 13.)

[34] J. J. Dongarra, I. S. Duff, D. C. Sorensen, and H. A. v. d. Vorst, *Numerical Linear Algebra for High-performance Computers*. SIAM, 1998. (Cited on page 37.)

[35] P. Dular, J. Gyselinck, C. Geuzaine, N. Sadowski, and J. P. A. Bastos, “A 3-D Magnetic Vector Potential Formulation Taking Eddy Currents in Lamination Stacks Into Account,” *IEEE Transactions on Magnetics*, vol. 39 no. 3, pp. 1424–1427, 2003. (Cited on pages 3, 26, and 48.)

[36] Y. DuTerrail, J. Sabonnadiere, P. Masse, and J. Coulomb, “Nonlinear complex Finite Element Analysis of Electromagnetic Fields in Steady-State AC Devices,” *IEEE Transactions on Magnetics*, vol. 20 no. 4, pp. 549–552, 1984. (Cited on page 43.)

[37] A. Emadi, *Handbook of Automotive Power Electronics and Motor Drives*. Boca Raton, FL: CRC Press, 2005. (Cited on page 2.)

[38] J. Erdman, R. Kerkman, D. Schlegel, and G. Skibinski, “Effect of PWM inverters on AC motor bearing currents and shaft voltage,” *IEEE Transactions on Industry Applications*, vol. 32, p. 250Ű259, 1996. (Cited on page 1.)

[39] K. Fujiwara, T. Nakata, . N. Takahashi, and H. Ohashi, “On the continuity of the magnetizing current density in 3-D magnetic field analysis with edge element,” *IEEE Transactions on Magnetics*, vol. 31 no. 3, pp. 1364–1367, 1995. (Cited on page 33.)

[40] Y. Gao, K. Muramatsu, K. Shida, K. Fujiwara, S. Fukuchi, and T. Takahata, “Loss Calculation of Reactor Connected to Inverter Power Supply Taking Account of Eddy Currents in Laminated Steel Core,” *Magnetics, IEEE Transactions on*, vol. 45, no. 3, pp. 1044–1047, 2009. (Cited on page 48.)

[41] G. Grandi, M. Kazimierczuk, A. Massarini, U. Reggiani, and G. Sancineto, “Model of laminated iron-core inductors for high frequencies,” *IEEE Transactions on Magnetics*, vol. 40 no. 4, pp. 1839–1845, 2004. (Cited on page 26.)

[42] J. Gyselinck, P. Dular, C. Geuzaine, and W. Legros, “Harmonic-balance finite-element modeling of electromagnetic devices: a novel approach,” *IEEE Transactions on Magnetics*, vol. 38 no. 2 pt. 1, pp. 521–524, 2002. (Cited on page 43.)

[43] K. P. K. H. Jordan, V. Klima, *Asynchronmaschinen - Funktion, Theorie, Technisches*. 1. Aufl., Akademiai Kiado, Budapest, 1975. (Cited on page 2.)

[44] K. A.-H. Haitham Abu-Rub, Mariusz Malinowski, *Power Electronics for Renewable Energy Systems, Transportation and Industrial Applications*. John Wiley & Sons, 2014. (Cited on page 9.)

[45] O. Heaviside, *Electrical Papers, Third Edition*. Chelsea Publishing Company, New York, 1970. (Cited on page 67.)

[46] B. Heller and A. Veverka, *Surge Phenomena in Electrical Machines*. London: Iliffe Books, 1968. (Cited on page 2.)

[47] H. Henke, *Elektromagnetische Felder: Theorie und Anwendung*. Springer, 2011. (Cited on page 27.)

[48] K. Hollaus and O. Bíró, “Estimation of 3-D eddy currents in conducting laminations by an anisotropic conductivity and a 1-D analytical model,” *COMPEL: The International Journal for Computation and Mathematics in Electrical and Electronic Engineering*, vol. 18 no. 3, pp. 494–503, 1999. (Cited on page 3.)

[49] V. B. Honsinger, “Theory of End-Winding Leakage Reactance,” *Power Apparatus and Systems, Part III. Transactions of the American Institute of Electrical Engineers*, vol. 78, no. 3, pp. 417–424, 1959. (Cited on page 16.)

[50] P. G. Huray, *Maxwell’s Equations*. John Wiley & Sons, 2011. (Cited on page 29.)

[51] I. Husain, *Electric and Hybrid Vehicles: Design Fundamentals, Second Edition*. CRC Press, 2011. (Cited on page 15.)

[52] M. Ibrahim and P. Pillay, “Core loss prediction in electrical machine laminations considering skin effect and minor hysteresis loops,” *IEEE Energy Conversion Congress and Exposition (ECCE)*, pp. 2681–2687, 2012. (Cited on page 13.)

[53] A. G. Jack and B. C. Mecrow, “Methods for magnetically nonlinear problems involving significant hysteresis and eddy currents,” *IEEE Transactions on Magnetics*, vol. 26 no. 2, pp. 424–429, 1990. (Cited on page 43.)

[54] D. Jiles and D. Atherton, “Theory of ferromagnetic hysteresis,” *Journal of Applied Physics*, vol. 55 no. 6, pp. 2115–2120, 1984. (Cited on page 11.)

[55] A. Kameari, “Calculation of transient 3D eddy current using edge elements,” *IEEE Transactions on Magnetics*, vol. 26, pp. 466–469, 1990. (Cited on page 35.)

[56] A. Küchler, *Hochspannungstechnik: Grundlagen - Technologie - Anwendungen*. Springer, 2009. (Cited on page 22.)

[57] P. Knupp and K. Salari, *Verification of Computer Codes in Computational Science and Engineering*. CRC Press, 2010. (Cited on page 44.)

[58] A. Kost, *Numerische Methoden in der Berechnung elektromagnetischer Felder*. Berlin: Springer Verlag, 1991. (Cited on pages 2, 33, 35, and 43.)

[59] M. Kuczmann, “Neural network based vector hysteresis model and the nondestructive testing method,” Ph.D. dissertation, Budapest University of Technology and Economics, 2004. (Cited on page 13.)

[60] J. Lammeraner and M. Stafl, *Eddy currents*. ILIFFE Books, London, 1966. (Cited on page 3.)

[61] L. D. Landau and E. M. Lifshitz, “Theory of the dispersion of magnetic permeability in ferromagnetic bodies,” *Phys. Z. Sowietunion*, vol. 8, pp. 6153–169, 1935. (Cited on page 10.)

[62] N. Lawrence, *Modern transmission line theory and applications*. John Wiley & Sons, 1979. (Cited on page 19.)

[63] R. Lin, "Electromagnetic and mechanical finite element analysis of end region of large-sized three-phase squirrel-cage induction machines," Ph.D. dissertation, Aalto University, 2010. (Cited on pages 16 and 20.)

[64] S. A. Maas, *Nonlinear Microwave and RF Circuits*. Norwood, MA: Artech House, Inc., 2003. (Cited on page 43.)

[65] P. Maeki-Ontto and J. Luomi, "Induction motor model for the analysis of capacitive and induced shaft voltages," *Conference Record of the International Electric Machines and Drives Conference IEMDC 2005, San Antonio, TX*, 2005. (Cited on page 3.)

[66] O. Magdun, "Calculation of high-frequency current distributions in inverter-fed electrical machines," Ph.D. dissertation, Technische Universität Darmstadt, 2012. (Cited on pages 3 and 28.)

[67] D. Makaveev, L. Dupré, M. De Wulf, and J. Melkebeek, "Dynamic hysteresis modeling using feed-forward neural networks," *Journal of Magnetism and Magnetic Materials*, vol. 254-255, pp. 256–258, 2003. (Cited on page 13.)

[68] I. D. Mayergoyz, *Mathematical models of hysteresis*. New York: Springer Verlag, 1991. (Cited on page 13.)

[69] D. Meeker, *FEMM (Finite Element Methods Magnetics), 2D Finite Element Solver*, version 4.2 for windows 32 and 64 bit ed., 2010-2012, available at: www.femm.info. (Cited on pages 3 and 5.)

[70] G. Meunier, *The Finite Element Method for Electromagnetic Modeling*. John Wiley & Sons, 2010. (Cited on page 29.)

[71] G. Miano and A. Maffucci, *Transmission Lines and Lumped Circuits: Fundamentals and Applications*. Academic Press, 2001. (Cited on page 67.)

[72] J. M. Miller, *Propulsion Systems for Hybrid Vehicles*. IET, 2004. (Cited on page 15.)

[73] P. Mäki-Ontto and J. Luomi, "Induction motor model for the analysis of capacitive and induced shaft voltages," *Proceedings of the 2005 IEEE-IEMDC International Conference on Electric Machines and Drives in San Antonio*, pp. 1653–1660, 2005. (Cited on page 25.)

[74] P. Monk, *Finite Element Methods for Maxwell's Equations*. Oxford University Press: Academic Press, 2003. (Cited on pages 29 and 35.)

[75] A. Muetze, "Bearing currents in inverter-fed ac-motors," Ph.D. dissertation, Technische Universität Darmstadt, 2004. (Cited on pages 1, 3, 16, 20, 55, and 58.)

[76] T. Nakata, N. Takahashi, K. Fujiwara, and A. Ahagon, "Periodic boundary condition for 3-D magnetic field analysis and its applications to electrical machines," *Magnetics, IEEE Transactions on*, vol. 24, no. 6, pp. 2694–2696, 1988. (Cited on page 41.)

[77] O. D. Neacsu, *Switching Power Converters: Medium and High Power, Second Edition*. CRC Press, 2013. (Cited on page 16.)

[78] W. L. Oberkampf and C. J. Roy, *Verification and Validation in Scientific Computing*. Cambridge University Press, 2010. (Cited on page 44.)

[79] D. O'Kelly, "Hysteresis and eddy-current losses in steel plates with nonlinear magnetisation characteristics," *Proceedings of the Institution of Electrical Engineers*, vol. 119 no. 11, pp. 1675–1676, 1972. (Cited on page 43.)

[80] P. Olszewski, "Expansion of periodic boundary condition for 3-D FEM analysis using edge elements," *IEEE Transactions on Magnetics*, vol. 28 no. 2, pp. 1084–1087, 1992. (Cited on pages 33, 35, and 41.)

[81] B. Oyegoke, "Transient voltage distribution in stator winding of electrical machine fed from a frequency converter," Ph.D. dissertation, Helsinki University of Technology, 2000. (Cited on pages 2 and 25.)

[82] Z. Peroutka, "Motor insulation breakdowns due to operation of frequency converters," in *Power Tech Conference Proceedings, 2003 IEEE Bologna*, vol. 2, 2003, p. 8 pp. (Cited on page 9.)

[83] J. Pippuri, "Finite element analysis of eddy current losses in steel laminations of inverter-fed electrical machines," Ph.D. dissertation, Aalto University, 2010. (Cited on page 3.)

[84] J. Pippuri and A. Arkkio, "Time-Harmonic Induction-Machine Model Including Hysteresis and Eddy Currents in Steel Laminations," *IEEE Transactions on Magnetics*, vol. 45 no. 7, pp. 2981–2989, 2009. (Cited on page 43.)

[85] F. Preisach, "Über die magnetische Nachwirkung," *Zeitschrift für Physik, Springer-Verlag*, vol. 94 no. 5-6, pp. 277–302, 1935. (Cited on page 11.)

[86] Z. Ren, "Influence of the R.H.S. on the convergence behaviour of the curl-curl equation," *IEEE Transactions on Magnetics*, vol. 32 no. 3, pp. 655–658, 1996. (Cited on page 33.)

[87] D. Roger, E. Napieralska-Juszczak, and A. Henneton, "High frequency extension of non-linear models of laminated cores," *COMPEL: The International Journal for Computation and Mathematics in Electrical and Electronic Engineering*, vol. 25 no. 1, pp. 140–156, 2006. (Cited on page 13.)

[88] R. Ruedenberg, *McGraw-Hill Electrical and Electronic Engineering Series*. McGraw-Hill Book Co., New York, 1950. (Cited on page 2.)

[89] S. J. Salon, D. J. Scott, and G. L. Kusic, "Electromagnetic forces on the end windings of large turbine generators. II. Transient conditions," *IEEE Trans. Power App. Syst.*, vol. PAS-102, no. 1, pp. 14–19, 1983. (Cited on page 16.)

[90] D. J. Scott, S. J. Salon, and G. L. Kusik, "Electromagnetic forces on the armature end windings of large turbine generators IŮSteady state conditions," *IEEE Trans. Power App. Syst.*, vol. PAS-100 no. 11, pp. 4597–4603, 1981. (Cited on page 16.)

[91] H. O. Seinsch, *Oberfelderscheinungen in Drehfeldmaschinen : Grundlagen zur analytischen und numerischen Berechnung*. Teubner, Stuttgart, 1992. (Cited on page 2.)

[92] V. C. Silva, G. Meunier, and A. Foggia, "A 3-D finite-element computation of eddy currents and losses in laminated iron cores allowing for electric and magnetic anisotropy," *IEEE Transactions on Magnetics*, vol. 31, no. 3, p. 2139Ű2141, 1995. (Cited on pages 26 and 48.)

[93] C. P. Steinmetz, "On the law of hysteresis," *Proceedings of the IEEE*, vol. 72 no. 2, pp. 197–221, 1984. (Cited on page 12.)

[94] R. Stoll, *The Analysis of Eddy Currents*. Oxford: Clarendon Press, 1974. (Cited on pages 3 and 14.)

[95] G. Stone, E. A. Boulter, I. Culbert, and H. Dhirani, *Electrical Insulation for Rotating Machines: Design, Evaluation, Aging, Testing, and Repair*. John Wiley & Sons, 2004. (Cited on pages 16, 53, and 54.)

[96] V. Subrahmanyam, *Thyristor Control of Electric Drives*. Tata McGraw-Hill Education, 1987. (Cited on pages 8 and 16.)

[97] M. Touma, "Three-dimensional finite element computation of eddy currents in synchronous machines," Ph.D. dissertation, Chalmers University of Technology, Göteborg, 1998. (Cited on page 33.)

[98] I. Vago, "On the interface and boundary conditions of electromagnetic fields," *Periodica Polytechnica Ser. El. Eng.*, vol. 38, no. 2, pp. 79–94, 1994. (Cited on page 33.)

[99] J. Wang, H. Lin, Y. Huang, and X. Sun, "A New Formulation of Anisotropic Equivalent Conductivity in Laminations," *IEEE Transactions on Magnetics*, vol. 47 no. 5, pp. 1378–1381, 2011. (Cited on pages 3 and 26.)

[100] J. P. Webb, "Hierarchical vector basis functions of arbitrary order for triangular and tetrahedral finite elements," *IEEE Transactions on Antennas and Propagation*, vol. 47 no. 8, p. 1495Ű1498, 1999. (Cited on page 29.)

[101] P. Weiss, "L'Hypothese du champ Moleculaire et de la Propriete Ferromagnetique," *Journal de Physique*, vol. 6 no. 1, pp. 661–690, 1907. (Cited on page 10.)

[102] S. Yamada, P. P. Biringer, and K. Bessho, "Calculation of Nonlinear Eddy-Current Problems by the Harmonic Balance Finite Element Method," *IEEE Transactions on Magnetics*, vol. 27 no. 5, pp. 4122–4125, 1991. (Cited on page 43.)

[103] C. Yeh and F. Shimabukuro, *The Essence of Dielectric Waveguides*. Springer, 2008. (Cited on page 29.)

[104] S. Zaglmayr, "High order finite element methods for electromagnetic field computation," Ph.D. dissertation, Johannes Kepler Universität Linz, 2006. (Cited on pages 29 and 36.)

[105] G. Zysman and D. Varon, "Wave propagation in microstrip transmission lines," in *Microwave Symposium, 1969 G-MTT International*, 1969, pp. 3–9. (Cited on page 67.)

List of Publications

[106] H. Jorks, E. Gjonaj, and T. Weiland, “Simulation of an induction motor including eddy-current effects in core laminations,” in *Computation in Electromagnetics (CEM 2011), IET 8th International Conference on*, 2011, pp. 1–2. (Cited on pages 5 and 6.)

[107] ——, “Eddy current analysis of a pwm controlled induction machine,” in *Proceedings of the 15th International IGTE Symposium on Numerical Field Calculation in Electrical Engineering (IGTE 2012)*, 2012, pp. 1–4. (Cited on pages 5 and 6.)

[108] ——, “Eddy current analysis of a pwm controlled induction machine,” in *Proceedings of the 9th Conference on Scientific Computing in Electrical Engineering (SCEE 2012)*, 2012, pp. 1–2. (Cited on pages 5 and 6.)

[109] ——, “Eddy Current Analysis of a PWM Controlled Induction Machine,” *The International Journal for Computation and Mathematics in Electrical and Electronic Engineering (COMPEL)*, vol. 32, no. 5, pp. 1609–1619, 2013. (Cited on pages 5 and 6.)

[110] ——, “High frequency transmission line model of induction motor employing 3d electromagnetic field simulation,” in *Proceedings of the 17th CIRP Conference on Electro Physical and Chemical Machining (ISEM 2013)*, 2013, pp. 1–2. (Cited on pages 5 and 6.)

[111] ——, “High frequency transmission line modelling of induction motors employing 3d electromagnetic field simulation,” in *Proceedings of the 9th International Symposium on Electric and Magnetic Fields (EMF 2013)*, 2013. (Cited on pages 5 and 6.)

[112] H. Jorks, T. Gjonaj, E.and Weiland, and O. Magdun, “Three-dimensional simulations of an induction motor including eddy current effects in core laminations,” *IET Science, Measurement & Technology*, vol. 6, no. 5, pp. 344–349, 2012. (Cited on pages 5 and 6.)

Acknowledgements

This work was partly carried out in the collaborative research group (FOR 575) ‘High-frequency parasitic effects in inverter-fed electrical drives’ funded by the German Research Foundation (Deutsche Forschungsgemeinschaft, DFG).

My special thanks go to Prof. Dr.-Ing. Thomas Weiland for supervising this work and providing a perfect scientific work environment,

to Prof. Dr.-Ing. Kay Hameyer for being co-advisor of this thesis,

to Prof. Dr.-Ing. habil. Dr. h.c. Andreas Binder for his valuable advice as the DFG FOR 575 research group leader,

to Prof. Dr.-Ing. Gerd Griepentrog and Prof. Dr. rer. nat. Sebastian Schöps for being members of the dissertation committee,

to PD Dr. rer. nat. habil. Erion Gjonaj for the scientific supervision and constructive remarks,

to Prof. Dr. Ir. Herbert De Gersem for helpful remarks.

I would also like to express my gratitude to the Institute of Electrical Energy Conversion for providing measurement and motor data,

to Annette Fröhlcke for technical aid and to Frank Denz for proofreading.

Thanks to all my colleagues from TEMF for their help, the valuable discussions and the unforgettable time we spent together.

Most of all, I am deeply thankful to Alex, Gustaf and Lucian, for always being supportive and making me laugh.

Darmstadt, April 2014
Hai Van Jorks

Curriculum vitae

Hai Van Le Jorks

2002-2009	Studium der Elektrotechnik an der TU Dresden.
2009-2014	Promotion am Institut für Theorie Elektromagnetischer Felder, Fachbereich Elektrotechnik und Informationstechnik, TU Darmstadt.